A new series of semiconducting azine polymers and their applications in organic electronics

by

Guanlin Wang

A thesis

presented to the University of Waterloo

in fulfillment of the

thesis requirement for the degree of

Master of Applied Science

in

Chemical Engineering (Nanotechnology)

Waterloo, Ontario, Canada, 2020

Author's Declaration

This thesis consists of material all of which I authored or co-authored: see Statement of Contributions included in the thesis. This is a true copy of the thesis, including any required final revisions, as accepted by my examiners.

I understand that my thesis may be made electronically available to the public.

Statement of Contribution

This thesis includes some data and discussions for a published paper, some of which were derived from cooperation with my group members. Part of the content in Chapter 1 and Chapter 2 was published in Guanlin Wang, Pankaj Kumar, Zhifang Zhang, Arthur D. Hendsbee, Haitao Liu, Xu Li, Jinliang Wang and Yuning Li, *RSC Adv.*, 2020, 10, 12876.

Abstract

The rise of renewable energy and the urgency of sustainable development make organic solar cells (OSCs) or organic photovoltaics (OPVs) valued. Among so many donor materials for bulk heterojunction structure, P3HT is one of the most common donor polymers which is cost-effective and has been studied deeply. The room and potential for the improvement of OSCs based on polythiophene material still need further research. Therefore, Poly(4,4'-didodecyl-2,2'-bithiophene-azine) (PDDBTA), a new semiconducting azine polymer was synthesized in only three steps. As a p-channel material, PDDBTA showed hole mobilities of up to 4.1×10^{-2} cm^2 V^{-1} s^{-1} in organic thin film transistors (OTFTs). As a donor in organic solar cells (OSCs), a 2.18% of power conversion efficiencies (PCEs) was achieved, which was the first example to use an azine-based polymer to fabricate organic photovoltaics (OPVs). These performances indicate the potential of bithiophene-azine polymers as a new type of low-cost semiconductor materials for OPVs and other organic electronics. The performances of OTFT and OPV devices have reached the same level as those fabricated with P3HT. However, the morphology of active layer mixed by PDDBTA and PCBM was relatively unsatisfying due to the poor solubility and high crystallinity nature based-on a straight longer side chain, which had an adverse effect to charge transport and charge collection of the active layer, thereby limited the J_{SC} and FF. In order to increase the solubility to form a better blend film morphology and lower the aggregation caused by high crystallinity, as well as obtain a better phase separation and maintain the original performance of PDDBTA, a branch sidechain polymer PDEHBTA and a shorter straight sidechain polymer with pyrrole units as backbone PHPA were synthesized. However, the low molecular weight of these two types of optimized structures became an obstacle that hindered the OPVs to gain a satisfactory J_{SC} and FF, and only 1.58% of PCE based on PDEHBTA OSCs and 1.1% of that fabricated with PHPA were obtained, respectively.

Acknowledgements

I would like to profoundly thank to my supervisor Prof. Yuning Li, who gave me a chance to be a master student in University of Waterloo. Two years of his patience and scientific guidance led me to sustain interest in semiconducting organic polymer science and photovoltaic devices. I am very much thankful for Chinese Scholarship Council who support my tuition fees and living cost.

I also would like to show thanks to Dr. Arthur Hendsbee, Dr. Xu Li, Dr. Keqiang He and Jenner Ngai, who helped me get familiar with all the facilities in labs and basic experiment skills. I am especially thankful for Arthur and Jenner who taught me how to test OTFT performance.

In addition, I am would like to thank Pankaj Kumar and Zhifang Zhang for helping test performance of the solar cells, AFM and XRD and thank Xiguang Gao for testing TGA and DSC. I also thank Yi Yuan, Chenyang Guo and Wuqi Li who enroll as master students at the same time with me, and I avoided many detours in my research career by discussing with them.

Finally, I would like to acknowledge the unequivocal support from my family and friends, I cannot complete my work without there constant encouragement.

Table of Contents

List of Figures

List of Tables and schemes

List of Abbreviation and Symbols

AFM: atomic force microscopy

CV: cyclic voltammetry

D-A: donor-acceptor

DDTS: dodecyl trichlorosilane

DSC: differential scanning calorimetry

FF: fill factor

HOMO: highest occupied molecular orbital

HT-GPC: high temperature gel-permeation chromatography

I_{ON}/I_{OFF}: current ON/OFF ratio

J_{SC}: short-circuit current density

λ_m: wavelength of incident light with maximum adsorption

L: channel length

LUMO: lowest unoccupied molecular orbital

NMR: nuclear magnetic resonance

OTFT: organic thin film transistor

OPV: organic photovoltaic

OSC: organic solar cell

P3HT: poly(3-hexylthiophene)

PCE: power conversion efficiency

PDDBTA: poly(4,4'-didodecyl-2,2'-bithiophene-azine)

TGA: thermogravimetric analysis

UV-Vis: ultraviolet-visible

V_{OC}: open-circuit voltage

V_{th}: threshold voltage

V_G: gate voltage

μ: charge carrier mobility

W: channel width in OTFT

XRD: X-ray diffraction

Other abbreviations and symbols are defined in the text

Chapter 1 Introduction

Part of this chapter in was published in Guanlin Wang, Pankaj Kumar, Zhifang Zhang, Arthur D. Hendsbee, Haitao Liu, Xu Li, Jinliang Wang and Yuning Li, *RSC Adv.*, 2020, 10, 12876.

1.1 Research background

Due to population growth and industrial development, the world's energy demand has greatly increased. Therefore, preventing energy crises is one of the most fortuitous problems in the 21st century. With population growth and development plans, the global available resources are drying up. Nowadays, people have realized that the burning of fossil fuels causes a serious greenhouse effect and has a serious impact on sustainable development.[1] Solar energy received 6-7 times of current annual global energy consumption from earth's surface, which is around 120,000 TW. [2] Therefore, the development and application of solar energy has gradually entered people's field of vision and received enough attention.

A solar cell is an electrical device which is based on Schottky barrier or a p-n junction and can take advantage of the photovoltaic characteristics of suitable semiconductors that can convert solar energy into electrical energy. [3]–[5]It can be used for multiple purposes, such as residential supply, automobile transportation and electric energy storage, without causing any air pollution or negative impact on the environment. In terms of the technological development of solar cells (also called photovoltaic cells), they can usually be divided into three generations.[6], [7] The first generation of solar cells is based on Si-single crystals and polycrystalline Si wafers.[7] Monocrystalline silicon solar panels have higher efficiency and longer service life, which has been

widely used in homes and factories as shown in **Figure 1.1**. However, their initial production cost and heavyweight make it impossible to use in other fields, such as portable wearable electronic devices.[8] The second generation of solar cells are based-on inorganic semiconducting thin film, such as copper indium gallium diselenium and cadmium telluride . Compared with silicon wafer technology, solar cells based-on thin film save materials, and low-temperature processes integrate cell insulation and a high level of automation in mass production, providing the potential to reduce costs in the manufacturing process. Another advantage is the use of flexible substrates, which provides more opportunities for the batteries as second-generation solar cells to participate in the field of energy conversion and opens new application areas. The third generations of solar cells including OSCs which are based-on organic semiconductor has showed great potential for solar energy, and they are still under research and development.[9]

Figure 1.1 Solar system based on Si-single crystals. **[7]**

OSCs which is also called OPVs show a series of advantages in many aspects. Firstly, it can be processed in solution, basically using printing technology to manufacture solar

panels in high yield. Printing technology will greatly reduce manufacturing costs and improve manufacturing efficiency compared with the production of inorganic solar cells.[10], [11], [12] Secondly, organic materials have the nature of light weight because of their low density and good flexibility, which are suitable for portable electronic devices (**Figure 1.2**) in special applications, because lightness and flexibility are the typical natural advantages of most organic materials.[13], [14] Last but not least, the diversity of semiconductors provides a means to adjust and optimize the properties of materials to meet the standards set by the application. Because of these characteristics, organic solar cells are considered one of the promising photovoltaic technologies, and they have shown the potential of solar energy storage and conversion in the future.
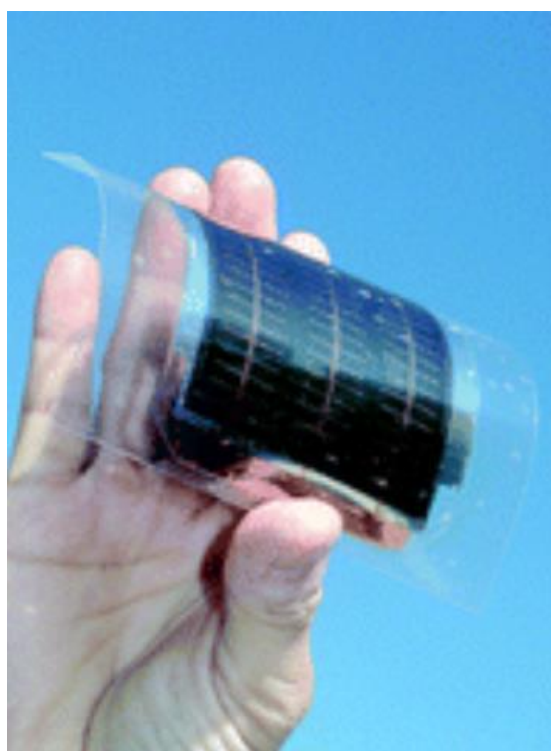
Figure 1.2 Thin-film flexible organic solar cells[15]

1.2 Organic solar cells (OSCs)

We all know that the manufacturing cost of fossil fuel power generation is higher than

the electricity from solar cells due to the cost of inorganic materials, high temperature processes and expensive vacuum systems. [16]–[18] **Table 1.1** summarizes the materials and structures used in organic solar cells in 20th century. In 1959, Kallmann and his group firstly made some photovoltaic measurements on single crystals based-on photoconductivity of anthracene, which laid the foundation for subsequent development of organic solar cells, although they could not explain the principles at that time.[19] A breakthrough was made by Tang's group in 1986, and the power conversion efficiency reached 0.95% based-on CuPc (donor)/PV (acceptor) structure as shown in **Figure 1.3**. However, the deposition of organic films in vacuum systems limited the devices performance.[20]

Table 1.1 Summary of key materials/structures used in organic solar cells reported from 1906 to 1995. [21]

Year	First author	Materials/Device structures	PCE (%)	Light intensity
1906	A. Pochettino	Anthracene crystals	-	-
1910	J. Koenigsberger	Benzene derivatives	-	-
1953	H. Mette	Antracene	-	-
1957	H. Hoegel	Poly(N-vinyl carbazole) (PVK)	-	-
1959	H. Kallmann	Anthracene	~0.1%	-
1960	O. H. Le Blanc	Anthracene	-	-
1960	R. G. Kepler	Anthracene crystals	-	-
1962	P. Mark	p-Terphenyl, p-quaterphenyl, anthracene	-	-
1966	N. Geacintov	Tetracene-water	-	-
1986	C. W. Tang	CuPc/PV	0.95%	75 mW/cm^2
1990	B. A. Gregg	Liquid crystalline porphyrins	V_{OC} : 0.3 V	100 mW/cm^2
			J_{SC} : 0.4 mA/cm^2	
1992	N. S. Sariciftci	MEH-PPV : C$_{60}$		
1995	G. Yu	MEH-PPV : PC$_{61}$BM	2.9%	20 mW/cm^2 at 430 nm
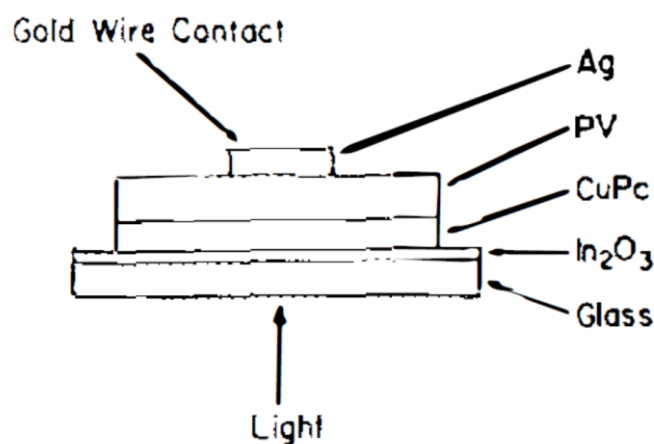
Figure 1.3 The OSC structure in Tang's group.[20]

By mixing soluble conjugated polymers with fullerenes, the second pioneering work can be attributed to the invention of bulk heterojunction structure (**Figure 1.4**) in 1992. [22]The latest pioneering work may be the first published by the Friend's group and Heeger's group in 1995 to realize the bulk heterojunction structure with p-type and n-type polymers.[23], [24] Organic photovoltaics (OPVs) have shown a rapid increase in PCE in the last few years with the highest efficiencies reaching 17–18%.[25]–[29]
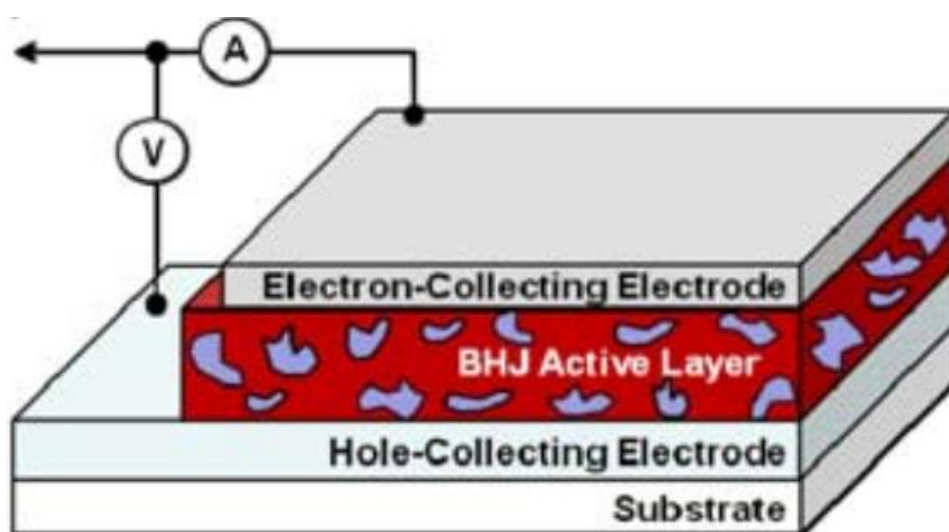
Figure 1.4 The structure of a BHJ active layer OSC.[21]

The photovoltaic conversion of a typical organic solar cell can be explained by five steps: (1) Light absorption: when photons produced in the BHJ active layer absorb sunlight, electrons will excite from HOMO to LUMO and pairs of electron and hole (so called exciton) will be created. (2) Exciton diffusion and (3) Exciton dissociation: the excitons diffuse to the interface of donor and acceptor, followed by being separated into free electrons and holes. (4) Charge transport and (5) Charge collection: the free holes travel through the LUMO of donor to acceptor and then will be collected at anode; the free electrons transport trough the HOMO of acceptor to donor and then will be extracted by cathode.[30], [31]

The performance of OSCs is most intuitively reflected in power conversion efficiency (PCE), which is affected by V_{OC} (open-circuit voltage), J_{SC} (short-circuit current density)

and FF (fill factor), and all of them can be obtained from a J-V curve an OSC. PCE can be described by an equation:

$$PCE = \frac{J_{SC}V_{OC}FF}{P_{in}}$$

Where P_{in} indicates the incident light power which is often considered as 100 mW/cm^2, the standard AM1.5G spectrum multiplied by the area of the cell. **T**he J-V curve of the most efficient solar cell so far from Ding's group by using D18 as donor material and Y6 as an acceptor, which set a new record in the field of OPV(**Figure 1.5**).[27]
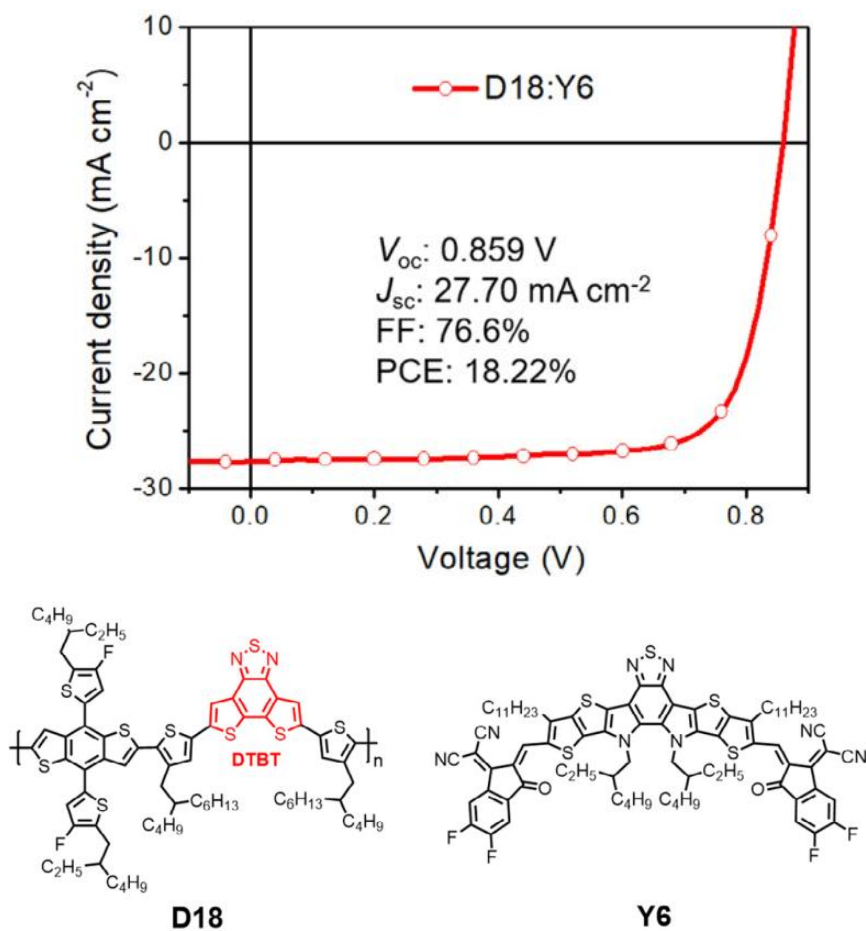
Figure 1.5 J-V curve of the OSC with the highest PCE in Ding's group and structures of D18 and Y6. **[27]**

As can be seen in **Figure 1.6**, each cell performance parameter J_{SC}, V_{OC} or FF is affected

by the photovoltaic process and material characteristics, which ultimately depend on the molecular structure of the polymer donor.[99] V_{OC} is mostly affected by the difference between HOMO energy of donor and LUMO energy of the corresponding acceptor as well as the dielectric constants of donor and acceptor, which can be described as an equation[32]:

$$V_{OC} = \frac{1}{e}\left(E_{HOMO}^{Donor} - E_{LUMO}^{Acceptor} - D\right) - \frac{KT}{e}ln\frac{N_e N_h}{N_C}$$

Where N_e is called the electron density in the acceptor domain, N_h is called the hole density in the donor domain under open circuit condition, and N_C is the density of states (DOS) of the donor edge and the main energy band, K is Boltzmann constant. The energy shift D is caused by disorder in the separate donor and acceptor domains. This equation can be approximately simplified due to BHJ solar cell design rule as follow[33], [34]:

$$V_{OC} = \frac{1}{e}\left(E_{HOMO}^{Donor} - E_{LUMO}^{Acceptor}\right) - 0.3V$$

J_{SC} is the current density under the condition of short circuited or the voltage across the device is zero, which is indicated by an equation:

$$J_{SC} = ne\mu E$$

n is charging density, e is elementary charge, μ is carrier mobility and E is electric-field strength. J_{SC} can be influenced by all the photovoltaic processes, among which (1) the number of excitons created rely on the absorption coefficient and bandgap energy according to the building block of donor; (2) the structure of donor polymer, film morphology and dielectric constant influence exciton diffusion; (3) exciton dissociation is affected by the building block, dielectric constant as well as the HOMO and LUMO energy offsets; (4) charge transport and collection are influenced by the balance degree between donor hole mobility and acceptor electron mobility. Fill factor FF determines the level of free carriers extraction from a device to the electrode,[35] which can be calculated based-on a J-V curve:

$$\frac{P_m}{P_{in}} = \frac{J_m V_m}{P_{in}} = \frac{J_{sc} V_{OC} FF}{P_{in}}$$

Thus, FF can be described as follow:

$$FF = \frac{J_m V_m}{J_{sc} V_{OC}}$$

Where P_{in} is light power incident, J_m is the current of maximum power while V_m is the voltage of maximum power. FF also mostly depends on the value and balance of hole mobility and electron mobility. The morphology and crystallinity of active layer thin-film influence mobility a lot,[36]–[38] which are affected by the donor polymer nature including structure of building block, side chain, molecular weight and defects (terminal groups, homo coupled units in a copolymer, random arrangements of comonomers in a copolymer, regio-irregular units, branching, lightly cross-linked units, oligomers, etc.)[39] Besides, the R_S (series resistance) and R_{SH} (shunt resistance) also take an effect on the J-V curve:

$$J = J_L - J_0 exp\left[\frac{q(V + JR_S)}{nKT}\right] - \frac{V + JR_S}{R_{SH}}$$

Where J_L is the photocurrent, J_0 is the dark saturation current, q is the elementary charge, n is the ideality of diode and V is the applied voltage. According to the equation above, FF will increase as R_{SH} rises and R_S falls.
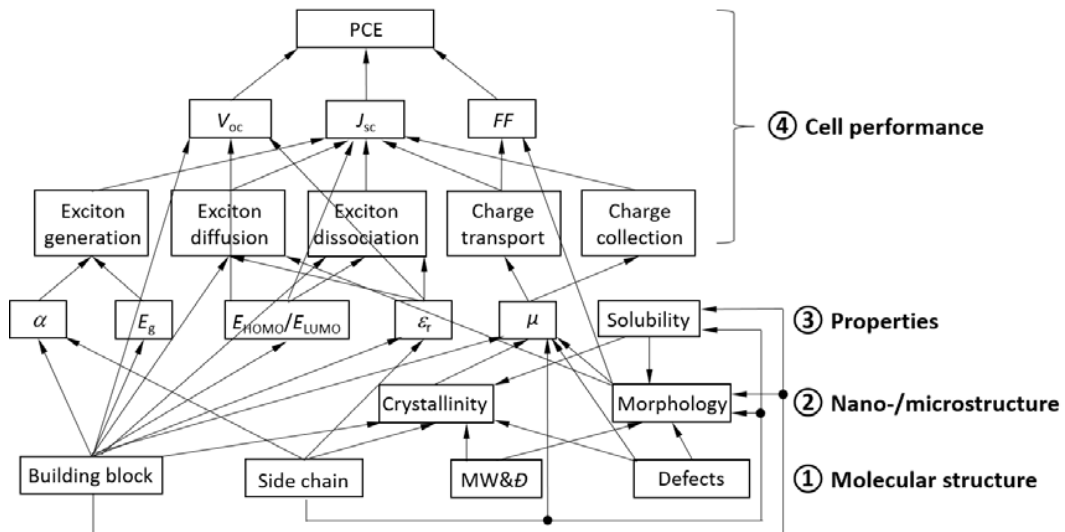
Figure 1.6 Scheme of structure-property-cell performance relationships of a polymer donor for OSCs, where α is the absorption coefficient, ε_r is the dielectric constant (or relative permittivity), μ is the mobility, and MW & Đ are the molecular weight and its distribution, respectively, of the polymer donor. Some or all these relationships may apply to small molecule donors as well as polymer and small molecule acceptors. **[39]**

1.3 P3HT: PC₆₁BM-based OSCs research status

The high-efficiency OPVs reported so far have unexceptionally used organic semiconductors synthesized tediously with numerous steps or high synthetic complexity, which results in very high costs.[25] To balance the PCE and manufacturing cost of the unit area, some low-cost donor materials with simple structures are also worth to be studied.[40] Furthermore, for organic solar cells to achieve large scale commercialization, low-cost organic semiconductors must be developed. [41]–[45]Among polymer donors, regioregular head-to-tail poly(3-hexylthiophene) (P3HT) has the lowest synthetic complexity since it can be synthesized in two steps starting from 3-hexylthiophene via the McCullough[46], [47] or Rieke method[48].[25] Zakhidov's group did a comparison experiment between two kinds of organic solar cell based-on P3HT: $PC_{61}BM$ and P3HT: ITIC, respectively (**Figure 1.7 shows** the structures of P3HT and $PC_{61}BM$). [49] The highest PCE of P3HT: ITIC device only shows 0.57% with a J_{SC} of 2.5 mA/cm^2, a V_{OC} of 0.53V and an FF of 0.43, however, the best performance for a P3HT: $PC_{61}BM$ OSC reached a PCE of 2.25% with a J_{SC} of 5.92 mA/cm^2, a V_{OC} of 0.65V and an FF of 0.59. The difference in photovoltaic characteristics of the two types of OSC should be attributed to the qualitative difference in the structure of the active layer, the structure of the P3HT polymer is close to amorphous and results in the P3HT: ITIC film having a significant resistance.[50] What's more, the key problem to increase PCE of these kinds of OSC was to form an ordered laminar structure in active layer blend films.[51]

In 2003, Padinger succeeded making an organic solar cell based-on P3HT: $PC_{61}BM$

which achieved 3.5% PCE.[52] Then in 2005, the same type of OSC made by Kim reached a same level of PCE as the one in Padinger's group which was 3.0%,[53] Li and Ma made a breakthrough that the efficiencies of P3HT: $PC_{61}BM$ OSCs achieved 4.4% and 5%, respectively.[54], [55]
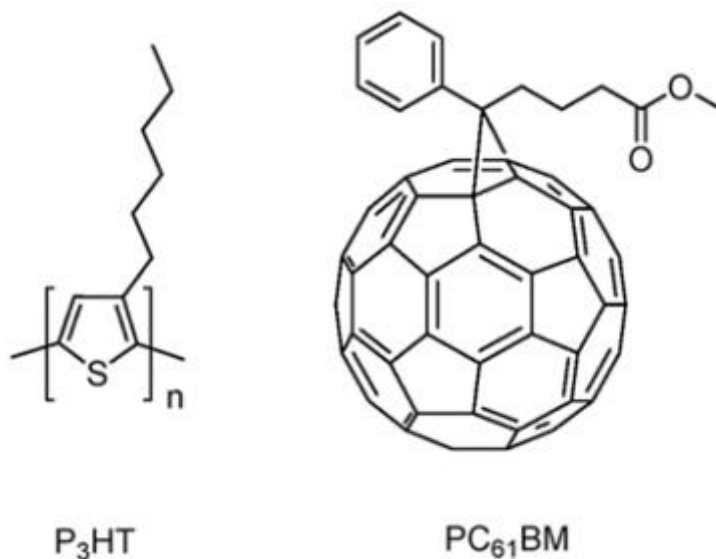
Figure 1.7 Structures of P3HT, $PC_{61}BM$**[56]**.

1.4 Characterizations of polymer

1.4.1 High Temperature Gel-permeation Chromatography (HT-GPC)

HT-GPC was used to measure the molecular weight of polymer in this project. When the polymer solution flows through the GPC column, molecules larger than the gel pores are excluded from the pores of the gel particles and only pass through the gap between the particles with a higher speed; and smaller molecules can enter the pores in the particles with a much lower speed; medium-sized molecules can penetrate into the larger pores, but are excluded by the smaller pores. After a chromatographic column of a certain length, the molecules are separated according to the relative molecular mass. The larger molecular mass molecule come out from the column firstly (shorter the elution time), and molecules with relatively smaller molecular mass come out

subsequently (longer the elution time).[57], [58]

HT-GPC measurements in this thesis were tested by Agilent PL-GPC220 by using 1,2,4-trichlorobenzne solution with a concentration of 10 mg mL^{-1} at 110 °C.

1.4.2 Cyclic Voltammetry (CV)

Cyclic Voltammetry is mainly carried out by applying a cyclic potential, from a starting potential to a terminal potential at a fixed rate, and then changing back to the starting potential at the same rate, which is a cycle.[59] A CV diagram can be drawn obtained from the analysis of a reversible oxidation reagent. When scanning from a low potential to a high potential, the analyte will show an oxidation peak of the oxidation current. Cyclic voltammetry is a three-electrode system, and three electrodes are passed into the test solution, which are working electrode, reference electrode and counter electrode, respectively.[59]–[61]

Cyclic voltammetry (CV) data in this thesis were obtained on a CHI600E electrochemical analyzer using an Ag/AgCl reference electrode and two Pt disk electrodes as the working and counter electrodes, respectively, in a 0.1 M tetrabutylammonium hexafluorophosphate solution in acetonitrile at a scan rate of 100 mV s^{-1}. Ferrocene was used as the reference, which has a HOMO level value of -4.8 eV. [62] Thus, the HOMO and LUMO levels can be approximately calculated by using the equations below:[63]

$$E_{\text{HOMO}} \text{ (eV)} = \text{-e } (E_{ox}^{onset}) \text{ - 4.8 eV}$$

$$E_{\text{LUMO}} \text{ (eV)} = \text{-e } (E_{red}^{onset}) \text{ - 4.8 eV}$$

where e is the energy of an electron and E_{ox}^{onset} and E_{red}^{onset} are oxidation and reduction redox onset potentials, respectively.[25]

1.4.3 Ultraviolet-visible Spectrometry (UV-vis)

Ultraviolet-visible Spectrometry is a method of irradiating a sample with a continuous spectrum of electromagnetic waves in the ultraviolet-visible light region as a light source to study the relative intensity of light absorption by a substance molecule.[64] We can qualitatively analyze by molecular UV-visible molecular absorption spectroscopy and quantitatively analyze based on Beer-Lambert law:

$$A = -log_{10}\frac{I_t}{I_0} = log_{10}\frac{1}{T} = K \cdot l \cdot c$$

Where A is absorbance; I_t is intensity of the incident light; I_0 is intensity of the transmitted light; T is transmittance; K is a coefficient; l is the thickness of the absorbance medium generally in cm; c is concentration of light absorbance substance, whose unit can be g/L or mol/L.

Due to Planck–Einstein relation: The relationship between the energy of a photon (photon energy), E, known as photon energy and its frequency, υ:

$$\boldsymbol{E} = \boldsymbol{h\upsilon}, \text{One photon: eV as unit}$$

$$E = h\upsilon = hc\ \bar{\upsilon} = h\frac{c}{\lambda} \cong \frac{1.986\text{x}10^{-16}\ (J\ nm)}{\lambda\ (nm)} = \frac{1240\ (eV\ nm)}{\lambda\ (nm)}$$

Where h: the Planck constant, 6.62607015×10-34 J.s; υ frequency, cycles/s or Hz; c speed of light in vacuum, 299,792,458 m/s; $\bar{\upsilon}$ wavenumber, cm^{-1}; λ wavelength, nm.

The bandgap of the polymer was calculated from the absorption onset wavelength, which determines the minimum excitation energy required for a photon excites an electron from ground states to the lowest excited states. The UV-Vis absorption spectra of polymers were recorded on Cary 7000 Universal Measurement Spectrophotometer (UMS).[25]

1.4.4 Thermogravimetric Analysis (TGA)

Thermogravimetric analysis measures the weight change which requires three highly accurate measurements: mass change, temperature, and temperature change.[65] The sample was placed in a small, electrically heated furnace equipped with a set of thermocouples to compare voltage output and voltage versus temperature to monitor accurate temperature measurements. The reference sample should be placed in a separate and confined space, which is filled with inert gas to prevent oxidation or other undesired reactions.

Within the required temperature range, no quality change is observed if samples are thermally stable, so there is little or no amplitude in the TGA curve corresponding to mass loss. [66]TGA also shows an upper temperature limit for samples.[67] When the temperature is higher than this limit, the substance will begin to decompose.

Thermogravimetric analysis (TGA) in this thesis was carried out on TA Instruments SDT 2960 at a scan rate of 10 °C min^{-1} under nitrogen.[25]

1.4.5 Differential Scanning Calorimetry (DSC)

DSC is a thermal analysis technique that uses a compensator to measure the relationship between the heating rate and temperature required to achieve the same temperature for the sample compared with reference. [68] The basic principle of DSC is that the sample absorbs or releases when it undergoes a phase change, glass transition, and chemical reaction. The compensator can measure increasing or decreasing heat flow in order to remain the sample and reference at a same temperature.

1.4.6 Atomic force microscope (AFM)

AFM is a nano-level high-resolution scanning probe microscope.[69] A micro-cantilever was used to sense and amplify the force between a sharp probe on the cantilever and the atoms of the sample with atomic resolution, so as to achieve the purpose of detection.[70] AFM can observe both conductor and non-conductor, which precludes the drawbacks of scanning tunneling microscope. This cantilever carries a probe, and the radius of curvature of the tip of the probe is on the order of nanometers. When the probe gets close to the surface of the sample, the probe head on the cantilever will bend and deflection due to the force on the surface of the sample (Hooke's law). In different cases, the force measured by AFM may be mechanical contact force, van der Waals force, gross suction force, chemical bond, orientation force, electrostatic force, magnetic force, etc.[71]

Atomic force microscope (AFM) images in this thesis were taken with a Dimension 3100 scanning probe microscope.

1.4.7 X-ray diffraction (XRD)

XRD is used to characterize the crystalline structure.[72] Crystals are regular arrangements of atoms, and X-rays can be viewed as electromagnetic radiation waves. Atoms mainly scatter X-ray waves through electrons, and X-rays also generate secondary spherical waves from electrons. This phenomenon is called elastic scattering. Although these waves cancel each other out in most directions through destructive interference, they overlap in some specific directions, which is determined by Bragg's law:[73]

$$2d \sin \theta = n\lambda$$

Where d is the spacing between diffracting planes, θ is the incident angle, n is any

integer, and λ is the wavelength of the beam.

X-ray diffraction (XRD) measurements in this thesis were carried out with a Bruker D8 Discover powder diffractometer equipped with a 2D detector using Cu Ka radiation (l ¼ 0.15418 nm) using standard Bragg–Brentano geometry.

1.5 Objective and Structure of This Thesis

Some groups have demonstrated that the glass transition of P3HT reaches up to 110°C while it absorbs a wide range of visible light with a wavelength of up to 650nm. [52], [53], [55], [74], [75]What more, a pretty high external quantum efficiency (EQE) at the maximum wavelength of P3HT: PCBM devices is usually close to 70% mostly due to the high level of recrystallization or chain stacking in rr-P3HT films thereby leads to a high charge carrier mobility. [75] It is unfortunate that the highest occupied molecular orbital (HOMO) level of P3HT is ca. ~5.0 eV, which is too high as a donor for OPVs since the open-circuit voltage (Voc) of the devices would be inevitably low. One approach to solve this issue is to develop acceptors with a higher lowest unoccupied molecular orbital (LUMO) level.[76], [77] However, the room for improvement is restricted by the stability of the acceptor since a sufficiently low LUMO level (ca. ~4 eV)[78]–[80] is required to achieve stable electron transport. The high HOMO level of P3HT is due to the electron-rich nature of the 3-hexylthiophene unit. To lower the HOMO level of a thiophene-containing polymer, one can simply incorporate an electron-withdrawing building block in the polymer backbone, which has led to numerous successes in achieving high Voc and high PCE using those so-called donor-acceptor (D–A)-type polymer donors in OPVs[50], [81], [82] although laborious synthetic processes for the acceptor building block and polymers are required.[25] Therefore, I had a consideration that modifying polythiophene backbone through a simple method would efficiently help lower the HOMO level and increase the V_{OC} of OSCs combining with $PC_{61}BM$ thereby reach a consistent or a higher level of PCE compared with P3HT based devices.

In Chapter 2, the facile synthesis of a new azine polymer PDDBTA based on bithiophene and azine units was recorded, which aimed at lowering the HOMO level, enhancing the open circuit voltage and achieving a same or a higher degree of OTFTs and OPVs performance compared with P3HT. Several characterizations (UV, CV, DSC etc.), which lays the foundation of considerable devices' performances based-on this azine polymer. PDDBTA exhibited good performances as a p-type semiconductor channel material in OTFTs and as a donor in OPVs. Particularly, this is the first example of an azine-based polymer for OPVs. The nature of higher HOMO level of PDDBTA gives larger V_{OC} and FF, which leads a same level of PCE compared with OSCs based on P3HT.

Two kinds of improvement work were summarized in Chapter3. What limits power conversion efficiency based-on PDDBTA is the relatively low J_{SC}. Therefore, the objective of this chapter is to try to increase J_{SC} through sidechain optimization which may help improve solubility and compatibility to improve film morphology. What's more, polypyrrole materials showed good properties on device applications with a high HOMO level, so pyrrole-azine polymer also hopes to be a series of high-quality material for OSCs. Characterizations of both two optimized polymers will be summarized in this chapter, and the shortcomings and improvements methods of these two materials will also be discussed

Finally, all the content of this thesis will be concluded and some future directions will be proposed in Chapter 4.

Chapter 2 Synthesis and characterization of poly(4,4'-didodecyl-2,2'-bithiophene-azine)(PDDBTA)

2.1 Introduction

In this study, we are interested in combining the azine (C=N–N=C) building block with an alkylated bithiophene to lower the HOMO level of the resulting bithiophene-azine polymer. The rationale is that azine is a p-conjugated building block, isoelectronic with the diene counterpart (C=C–C=C), but more electron-withdrawing due to the higher electronegativity of nitrogen than carbon. Furthermore, the azine linkage can be easily synthesized by a simple condensation reaction between an aldehyde (or ketone) and hydrazine, which is very attractive in terms of largescale production. Despite their facile synthesis, very few azine-based polymers have been studied as semiconductors for organic electronics.[83]–[87] This is partially due to the reputation of azine as a "conjugation blocker" or "conjugation stopper" given in some literature.[88], [89] Nonetheless, a few recent accounts have demonstrated that azine-based p-conjugated polymers may be promising semiconductors for organic electronics.[25], [83]–[87] According to our initial guess, the azine group will lower the HOMO level of the bithiophene structure, so Density Functional Theory (DFT) was needed before the synthesis of PDDBTA. The simulation results are shown in **Figure 2.1**, after adding an azine group between two thiophene rings, the HOMO level of the bithiophene-azine group decreases from -5.48 eV to -5.63 eV, which demonstrates our hypothesis.
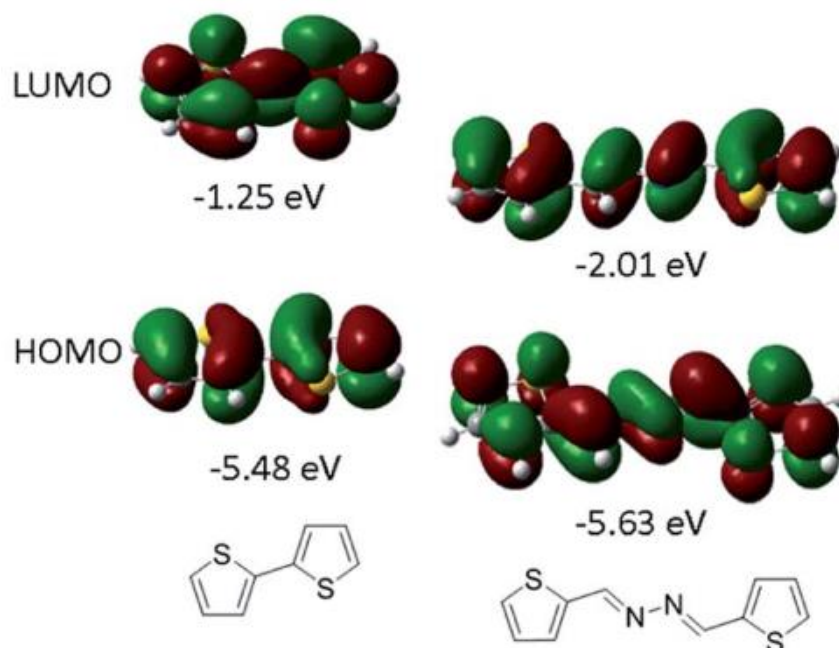
Figure 2.1 HOMO/LUMO orbitals and energy levels (with respect to vacuum, 0 eV) of bithiophene and bithiophene-azine calculated using the density functional theory (DFT) by using Gaussian 09 with by using Gaussian 09 with the 6-31G(d) basis set and B3LYP hybrid functional[25]

PDDBTA started from a coupling reaction with 3-dodecylthiophene to obtain 4,4'-didodecyl-2.2'-bithiophene, then was added to aldehyde groups on 5,5' positions to get the monomer 4,4'-didodecyl-2,2'-bithiophene-5,5'-dicarboxaldehyde.

2.2 Synthesis of poly(4,4'-didodecyl-2,2'-bithiophene-azine) (PDDBTA)
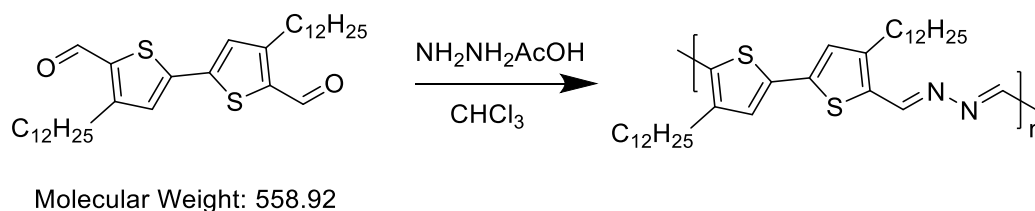
Scheme 2.1 Synthesis of PDDBTA

4,4'-Didodecyl-2,2'-bithiophene-5,5'-dicarboxaldehyde (400 mg, 0.72 mmol) and dry hydrazine acetate (65.9 mg, 0.72 mmol) were added into a double-neck round-bottom

flask. After being evacuated and backfilled with argon at room temperature three times, chloroform (4 mL) was added. The mixture was heated to reflux for 20 h. Three drops of 2-thiophenecarboxaldehyde were added to terminate any residual hydrazine end groups. The mixture was cooled down to room temperature and poured into stirring methanol (100 mL). The precipitate was collected by filtration, followed by Soxhlet extraction with acetone, hexane, heptane and chloroform. The chloroform fraction was poured into methanol and the precipitates were filtered and dried to afford the target polymer as a dark solid. Yield: 164 mg (41%)[25] The M_w was 24.1 kD with a corresponding M_n of 15.6 kD, which was measured by low temperature GPC. A dispersity of polymer at 40 degrees centigrade was 1.59.

It's worthy to mention that I tried to make the condensation polymerization with 4,4'-didodecyl-2,2'-bithiophene-5,5'-dicarboxaldehyde and hydrazine anhydrate several times previously with the same reaction conditions. However, the best yield of target material precipitated in methanol after Soxlet extracted with acetone, hexane and chloroform. The chloroform part only reached 17%, which means the molecular weight of this batch of polymer is not high enough, and the direct cause of this situation is that the molar quantities of two reactants are not equal. The strong water absorption of hydrazine anhydrate led the concentration of hydrazine anhydrate to decrease due to prolonged exposure to the air. Meanwhile, liquid is also difficult to measure the weight and volume in such a small scale for polymerization. Therefore, hydrazine acetate, an easy-to-weight salt which is relatively more stable in the air can be measured accurately and promotes this reaction to be successful and increases the molecular weight of PDDBTA.

2.3 Characterization of PDDBTA compared with P3HT

The P3HT (HT=98%) we used as reference in this thesis was commercially purchased from 1-Material.

2.3.1 HT-GPC for PDDBTA and P3HT

The HT-GPC results of PDDBTA and P3HT were showed in **Figure 2.2** (a) PDDBTA and (b) P3HT. For PDDBTA, the number average molecular weight M_n is 21.8 kD and weight average molecular weight M_w is 34.3 kD, and dispersity of polymer (**PD**) is 1.58, where **PD**= M_w/ M_n. For rr-P3HT from 1-Material, the number average molecular weight M_n is 30.9 kD and weight average molecular weight M_w is 44.7 kD, and dispersity of polymer (**PD**) is 1.45. The molecular weight results M_n and M_w were both larger than those tested by low temperature GPC, which indicated that the higher molecular weight fraction of PDDBTA did not dissolve completely due to the relatively poor solubility or the aggregation of molecules.

(a)
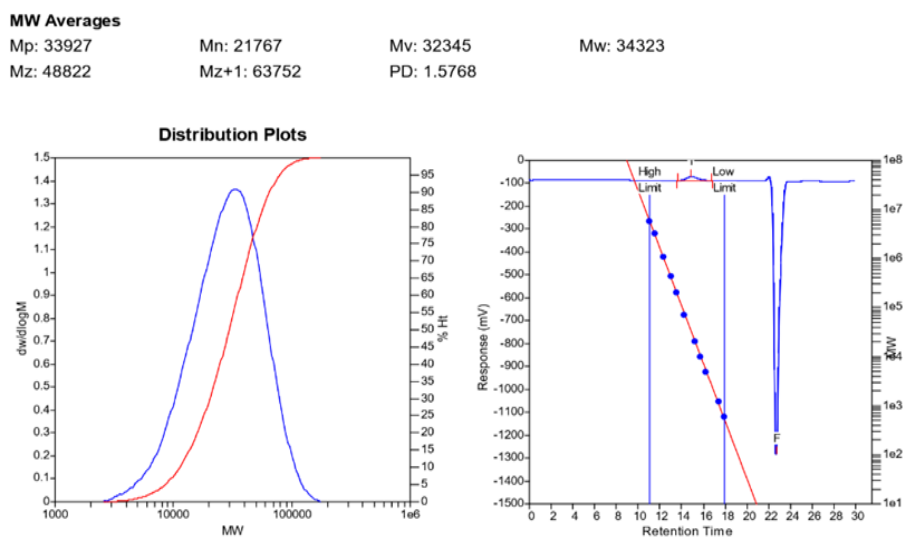
MW Averages

Mp: 45010	Mn: 30867	Mv: 42600	Mw: 44706
Mz: 60400	Mz+1: 79026	PD: 1.4483	
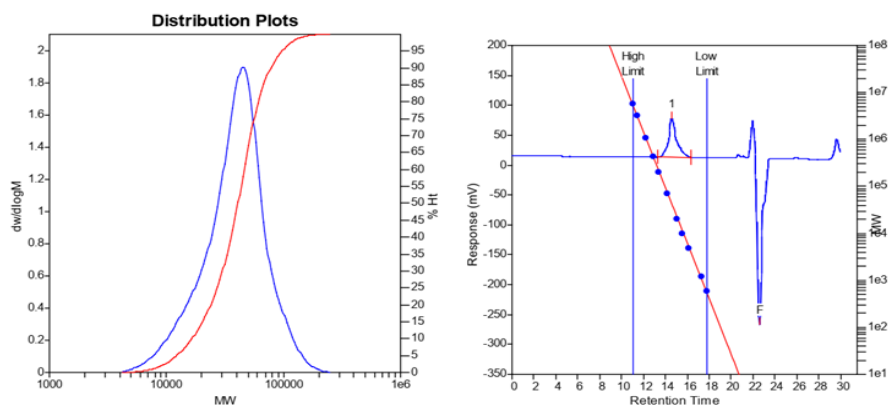
(b)

Figure 2.2 High temperature GPC diagrams for (a) PDDBTA and (b) P3HT (HT% = 98%, from 1-Material), measured using 1,2,4-trichlorobenzne as eluent at 110 °C with a flow rate of 1.00 mL min⁻¹.

2.3.2 NMR for PDDBTA

Compared with two spectra below, **Figure 2.3&2.4** shows a small peak at *J*=9.90 which corresponds to protons on the aldehyde groups (*J*=10.0 showed in **Figure 2.3**). After adding 2-thiophenecarboxaldehyde as termination, there is no such peak anymore, which prevented acetone reacting with aldehyde groups during Soxlet extraction.
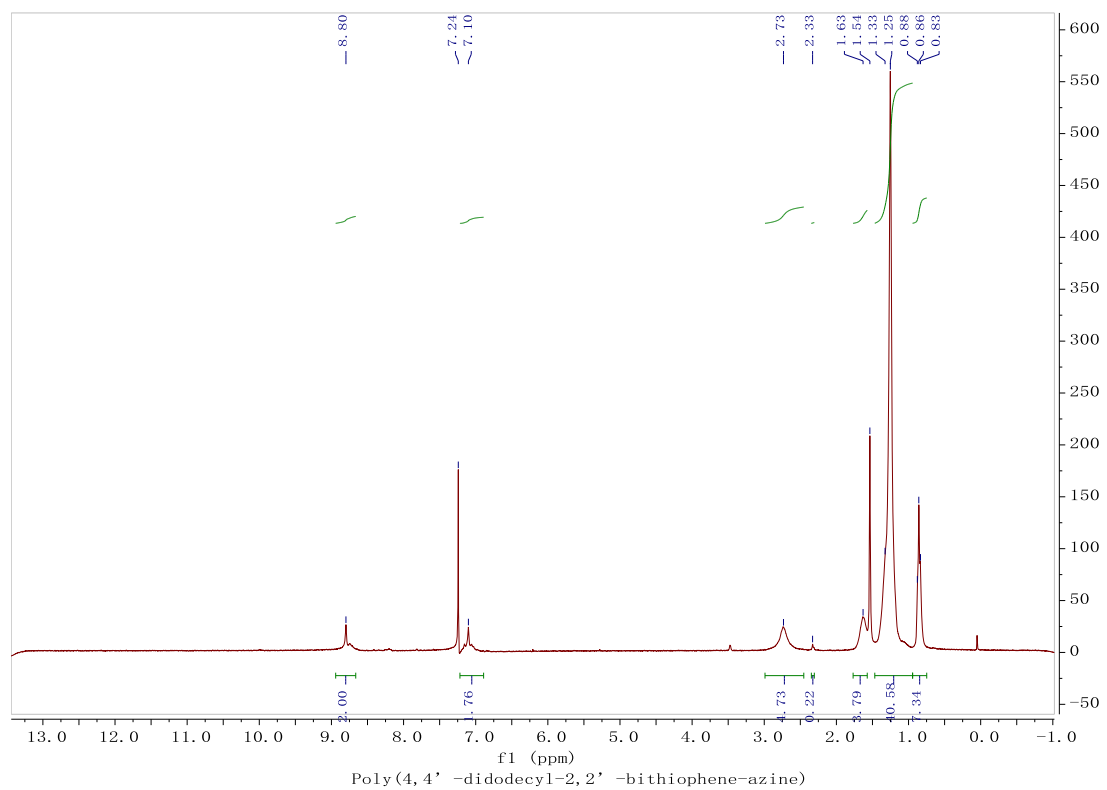
Figure 2.3 300 MHz ^{1}H NMR spectrum of PDDBTA in CDCl$_3$. NMR data was measured by a Bruker DPX 300 MHz spectrometer with chemical shifts relative to tetramethylsilane (TMS, 0 ppm).
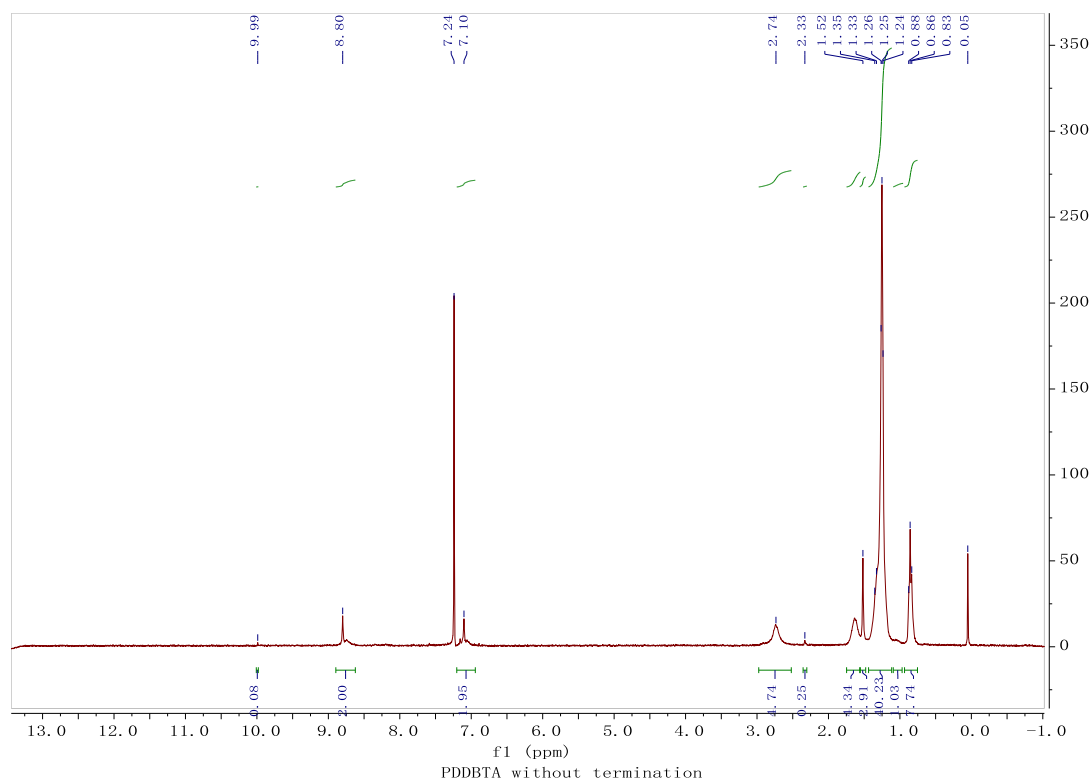
Figure 2.4 300 MHz ^{1}H NMR spectrum of PDDBTA without termination in CDCl$_3$.

2.3.3 CV for PDDBTA and P3HT

Cyclic voltammetry (CV) was used to determine the HOMO energy level of PDDBTA in the solid state (**Figure 2.5**). Oxidation started to occur at a potential of 0.75 V vs. Ag/AgCl, which corresponds to a HOMO level of -5.55 eV. The polymer showed no reduction peak and thus the LUMO level was estimated by using the HOMO level and the optical band gap to be -3.54 eV (mentioned in section **2.2.4**). The HOMO level of this polymer is much lower than that of regioregular P3HT (-5.14 eV) (mentioned in section **2.2.4**). The results are consistent with the DFT simulation results (**Figure 2.1**), which indicate that by the incorporation of an azine, the resulting bithiophene-azine unit has lower HOMO and LUMO levels in comparison to bithiophene, indicating the strong electron withdrawing effect of the azine unit. The lowered HOMO and LUMO levels are desirable for achieving a higher V_{OC} in OPV devices.[25]
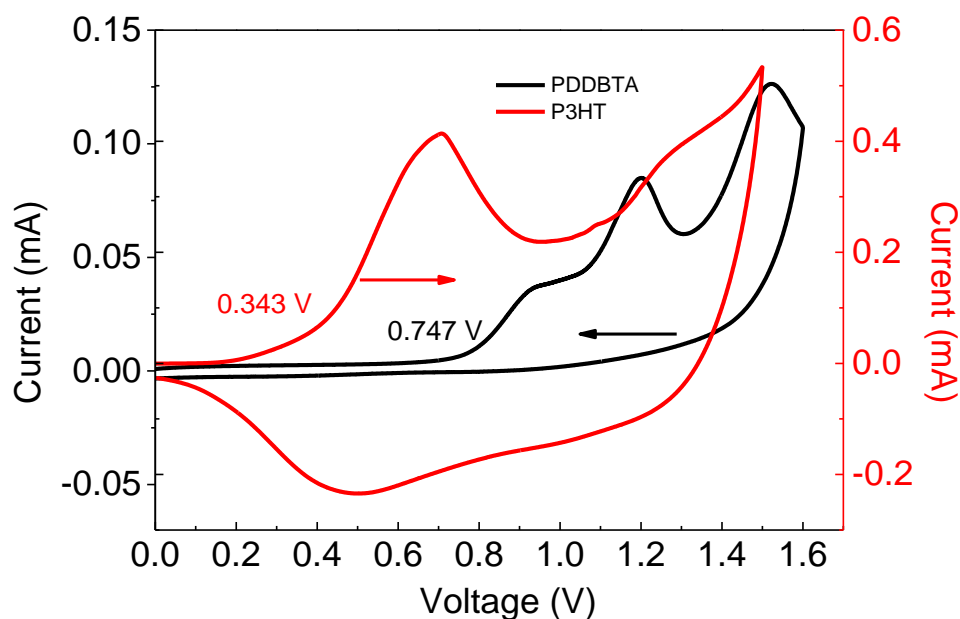
Figure 2.5 Cyclic voltammograms of PDDBTA and P3HT films measured in tetrabutylammonium fluoride (0.1 M) solution in acetonitrile using Ag/AgCl as the reference electrode.

2.3.4 UV for PDDBTA and P3HT

UV-vis absorption spectrum of PDDBTA in a chloroform solution showed a wavelength of maximum absorbance (λ_{max}) at 529 nm, while the as-cast polymer film showed a significant red-shift with a λ_{max} at 551 nm along with the appearance of a shoulder peak at 595 nm (**Figure 2.6**), which is indicative of the chain ordering and backbone planarization in the solid state. For the film annealed at 150 °C, the peak at 595 nm slightly intensified resulting from an improved chain packing. [25]

According to this equation:

$$E = h\upsilon = hc\ \bar{\upsilon} = h\frac{c}{\lambda} \cong \frac{1.986 \text{x} 10^{-16}\ （J\ nm）}{\lambda\ (nm)} = \frac{1240\ (eV\ nm)}{\lambda\ (nm)}$$

The bandgap of the polymer was calculated from the absorption onset wavelength to be 1.96 eV, which is slightly larger than that of P3HT (1.91 eV) (**Figure 2.7**).
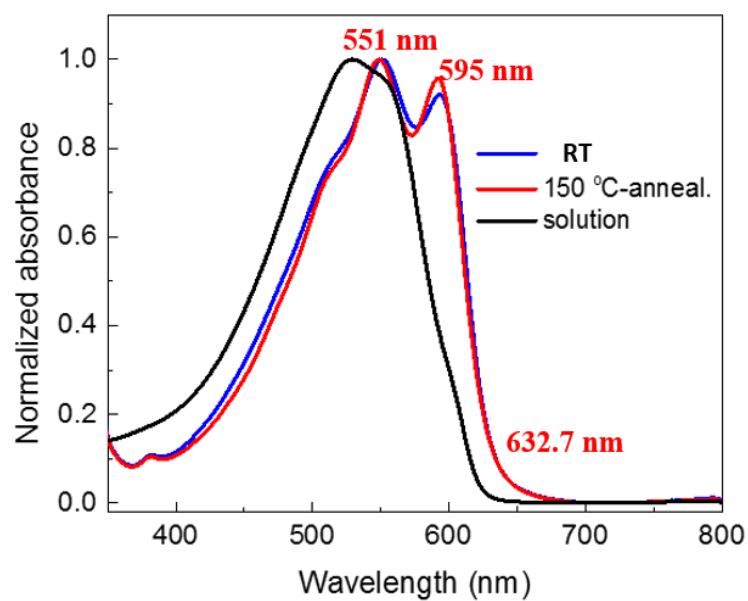
Figure 2.6 UV-vis absorption spectra of PDDBTA in solution in chloroform and films.
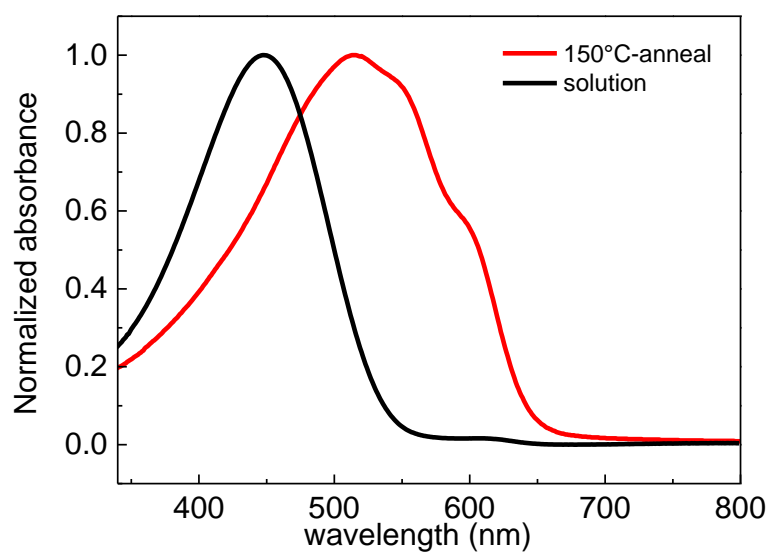
Figure 2.7 UV-vis absorption spectra for P3HT in a chloroform solution and as a thin film annealed at 150 °C.

2.3.5 TGA for PDDBTA

Thermogravimetric analysis result (**Figure 2.8**) shows that PDDBTA lost 2% of its weight when heating up to 280 °C, which indicates a good thermal stability. And two hundred degrees centigrade is high enough for normal OPVs fabrication.
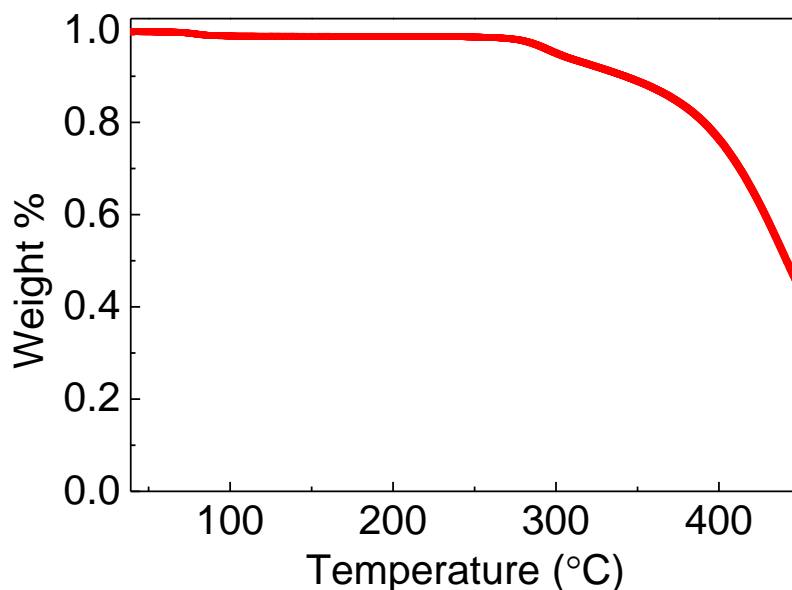
Figure 2.8 The TGA curve of PDDBTA obtained at a heating rate of 10 °C min^{-1} under nitrogen.

2.3.6 DSC for PDDBTA

In the first heating scan (**Figure 2.9 (a)** from -20 °C to 210 °C), the polymer sample, which was precipitated from methanol after Soxhlet extraction (see the polymer synthesis section), showed a glass transition temperature (T_g) at 46.7 °C), followed by a melting temperature at 160.8 C and then another melting temperature at 206.4 °C. The results indicated that there was a significant portion of amorphous phase in the as-precipitated sample. The first and second melting temperatures represent the melting of the side chains and backbones, respectively. After cooling, a melting temperature appeared at 148.8 °C and a broad transition at ca. 6.5 °C might represent the crystallization of the backbone and side chains, respectively. During the second heating

scan (**Figure 2.9 (a)** -20 °C to 220 °C), the melting temperatures for the side chains and backbones appeared at 147.3 °C and 204.0 °C, respectively, while no visible glass transition temperature was observed, indicating that the sample became more crystalline after the first heating/cooling cycle. The liquid crystal behavior due to the different melting temperatures of the side chains and backbones have been observed some other thiophene-based π-conjugated polymers. [90]–[92]It is noticed that the crystallization peaks became weakened in the second cooling scan, which indicates that the polymer partially decomposed. [25]

When a PDDBTA sample was heated to a high temperature of 250 °C (**Figure 2.9 (b)**), no crystallization temperature was observed during the subsequent cooling scan, indicating the complete decomposition of the polymer sample. Based the DSC data, PDDBT might start to decompose around 200-210 °C, which is consistent with the observed decrease in crystallinity in the XRD diagrams and hole mobility for the OTFT devices as well as the appearance of pinholes in the AFM image for the polymer films annealed at 200 °C.[25]
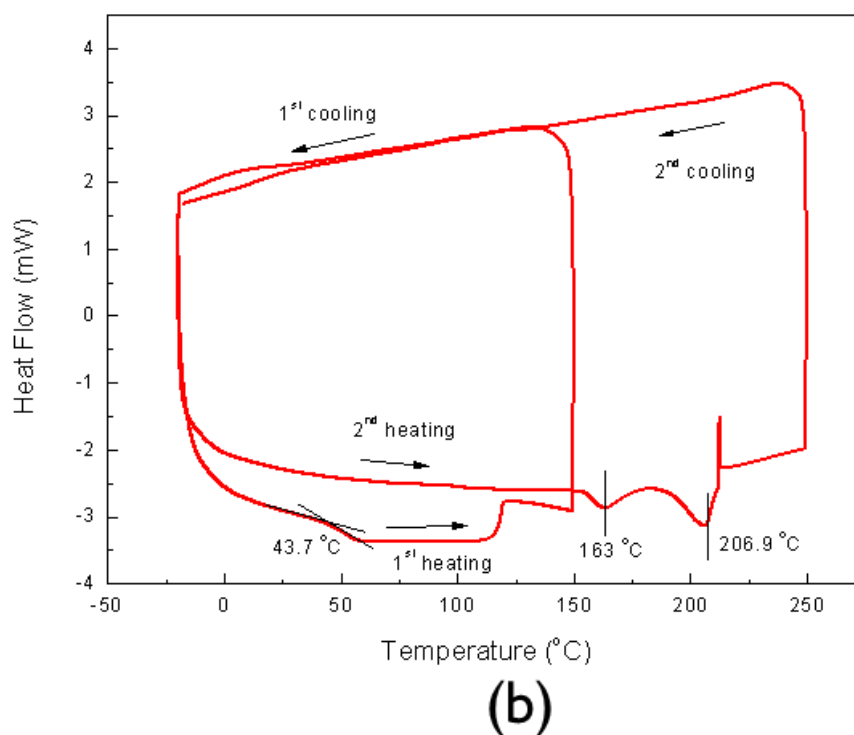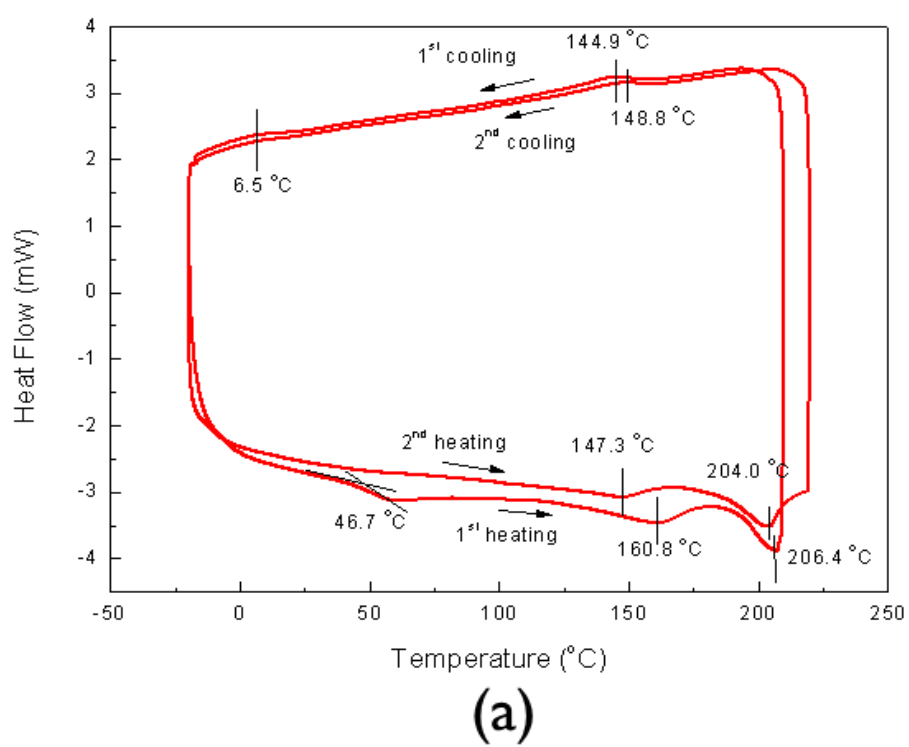
Figure 2.9 DSC diagrams of PDDBTA measured at a heating rate of 5 °C min^{-1} under nitrogen.

2.3.7 AFM for PDDBTA

The neat PDDBTA films AFM height images annealed at different temperatures are shown in **Figure 2.10**. Five annealing temperatures for AFM samples, room temperature,50 °C, 100 °C, 150 °C and 200 °C correspond to the annealing temperature for hole mobility measurement which will be mentioned in **Section 2.3.1**. The substrates of AFM samples are SiO2/Si wafers, which are identical with OTFT devices, in order to ensure the morphology of PDDBTA polymers consistent during different characterizations. We can see that the crystallinity of PDDBTA become higher gradually when the annealing temperature is no more than 150 °C, however, there are some black pinholes shown in the image with a 200 °C annealing temperature. This is due to the partial decomposition of the polymer at this temperature (see the discussion of DSC results in the **Section 2.2.6**), which also explains the appearance of pinholes in the AFM image of the film annealed at this temperature. [25]Some further effects on OTFTs will be discussed in next **Section 2.4**.
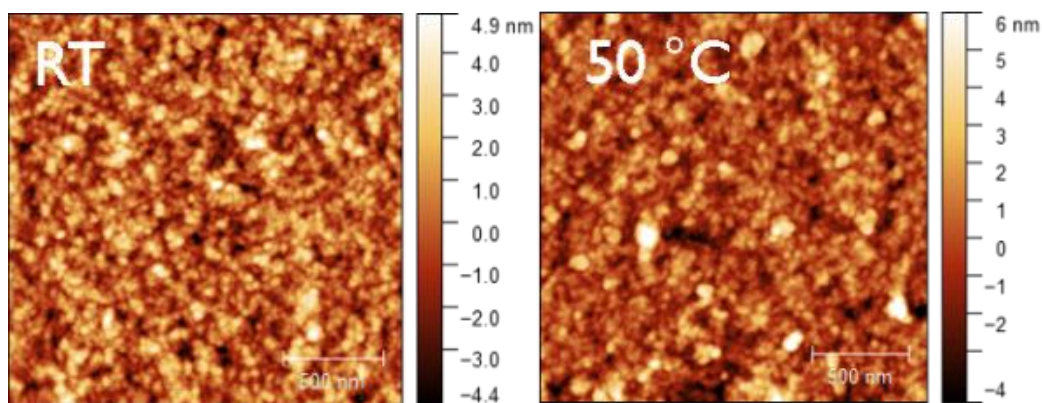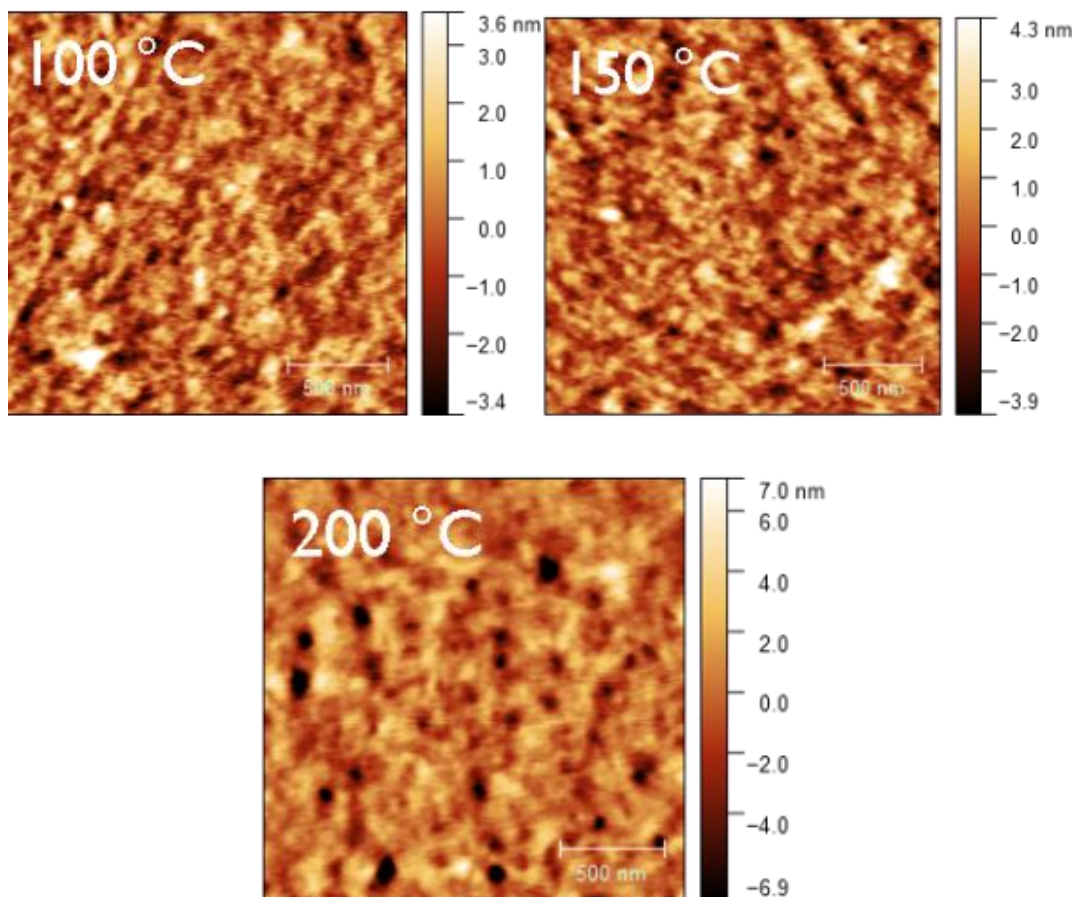
Figure 2.10 AFM height images of neat PDDBTA films on SiO2/Si wafers annealed at different temperatures.

2.3.8 XRD for PDDBTA

The crystalline structure of the polymer films was characterized by XRD (**Figure 2.11 (a)**) and **Table 2.1**. The neat as-spun polymer film showed an intense peak at $2\theta = 4.68°$, corresponding to a d-spacing of 1.89 nm, which can be assigned to the distance between the (100) planes of the lamellar crystal structure formed in the polymer thin film. For the films annealed at 50 °C and 100 °C, the secondary (200) peaks intensified, suggesting improved ordering and lamellar packing in these films. Upon annealing at 150 °C, the (100) peak position shifted to a lower diffraction angle of 4.03° or a larger d-spacing of 2.19 nm. This observation is consistent with the phenomenon of thermal

relaxation of side chains leading to increased order in the lamellar direction.[25], [93]A further increase in annealing temperature to 200 °C slightly decreased the crystallinity, which also demonstrates that the partial decomposition occurs at this temperature corresponding to DSC and AFM images (**Figure 2.9** & **Figure 2.10**).

In order to characterize the π-π stacking distance (not visible in the reflection XRD diagrams in **Figure 2.11**), a polymer flake was sandwiched between mica sheets to obtain a transmission XRD diagram. A weak (101) peak can be observed at $2\theta = 23.3°$ (**Figure 2.12**) corresponding to a π-π stacking distance of 0.38 nm.[25]
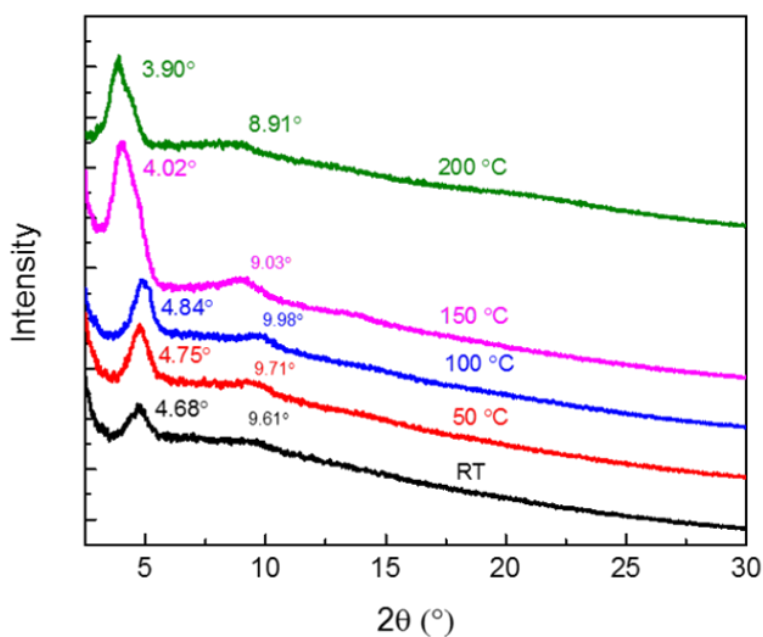
Figure 2.11 XRD patterns of neat PDDBTA films on SiO2/Si wafers annealed at different temperatures;
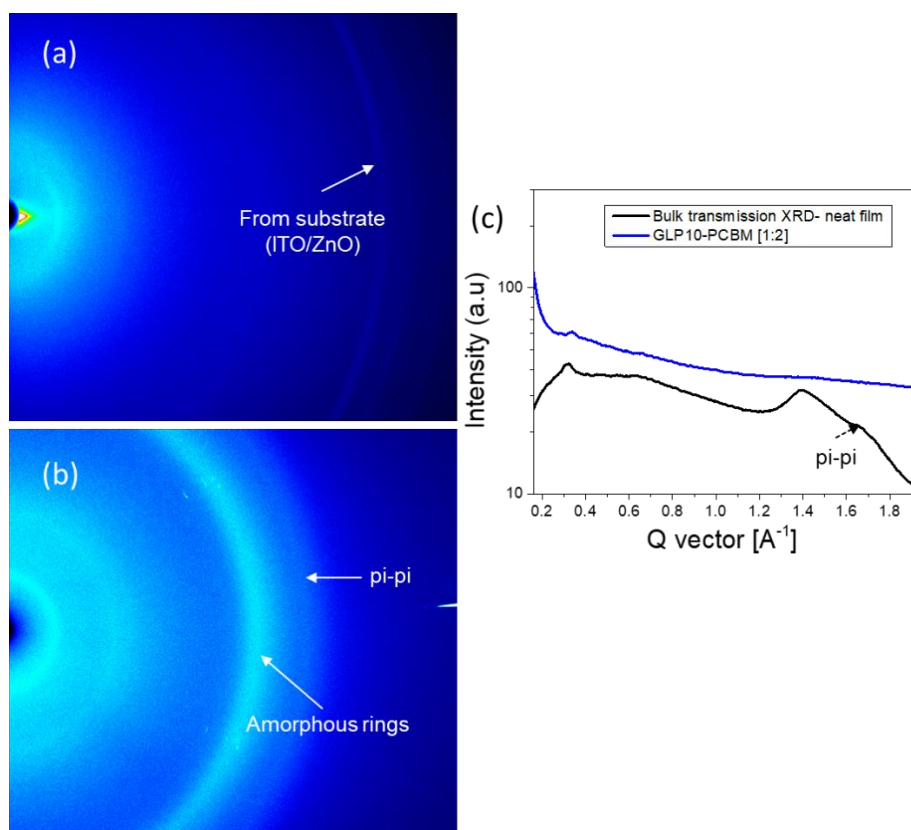
Figure 2.12 2D GIWAXS images (a) a PDDBTA:PCBM (1:2) blend film on a ZnO/ITO substrate (b) a neat PDDBTA sample in the transmission mode using polymer flakes sandwiched between two thin (75-100 μm) mica films. The corresponding out-of-plane line-cuts are shown in (c).

Table 2.1 XRD data for neat PDDBTA thin films.

Annealing temperature	(100) peak position 2θ (°)	d-spacing distance of (100) planes, d (nm)	Momentum transfer, Q (Å^{-1})
RT	4.68°	1.89	0.33
50°C	4.75°	1.86	0.34
100°C	4.84°	1.83	0.34
150°C	4.03°	2.19	0.29
200°C	3.90°	2.26	0.28

2.4 Characterization of OTFTs for both PDDBTA and rr-P3HT

2.4.1 Hole mobilities at increasing annealing temperature

To evaluate the charge transport performance, PDDBTA was used as a channel material in bottom-gate bottom-contact (BGBC) OTFTs using dodecyltrichlorosilane-modified SiO_2/Si substrates and gold contacts. The as-spun polymer films showed apparent p-type semiconductor performance with hole mobilities of up to 2.1×10^{-2} cm^2 V^{-1} s^{-1} (**Figure 2.13 (a)** and **Table 2.2**) when the devices were tested under argon. A relatively high threshold voltage (V_{th}) of -37 V was observed, which might be due to the rather low HOMO level of this polymer, resulting in a large hole injection barrier from the gold contact. After annealing at 150 °C for 20 min, the mobilities increased to 4.1×10^{-2} cm^2 V^{-1} s^{-1} (**Figure 2.13 (d)**). Then annealing to 200 °C for 20 min, the average mobility decreased to 3.3×10^{-2} cm^2 V^{-1} s^{-1} due to the start of decomposition as discussed in **Section 2.3.6.**[25]

(a)

(b)

(c)

(d)

34
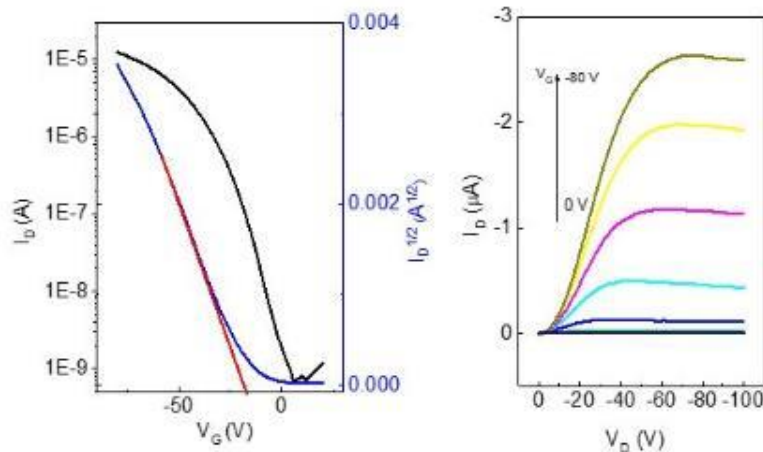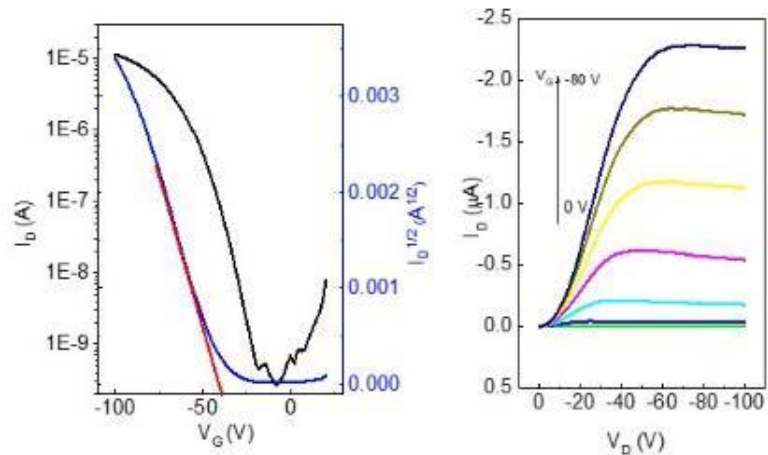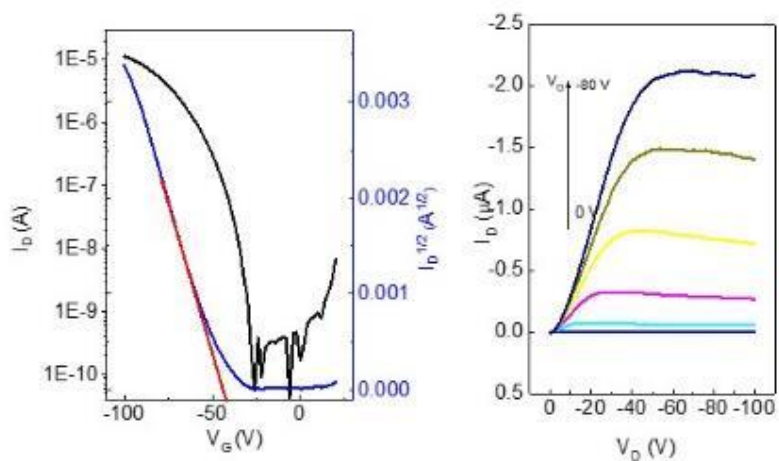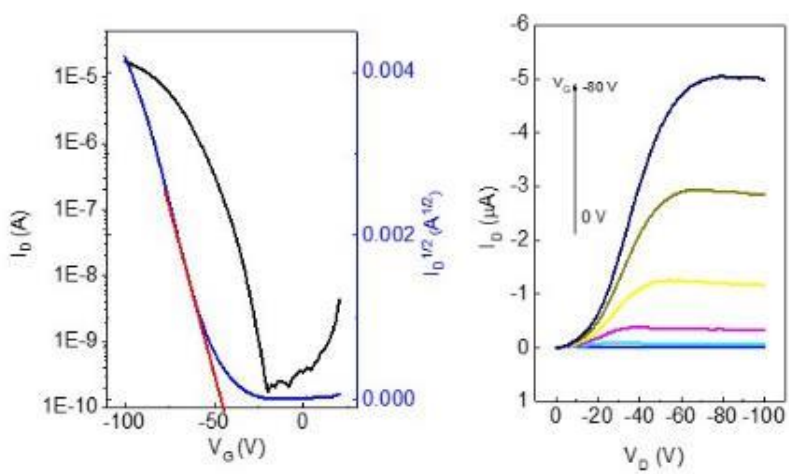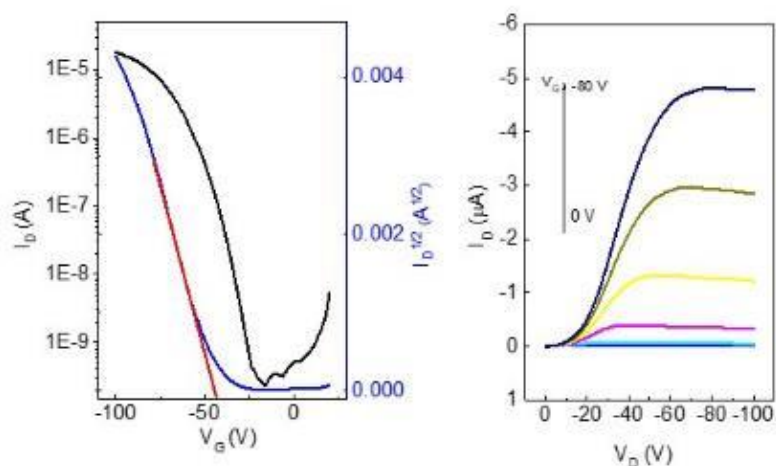
(e)
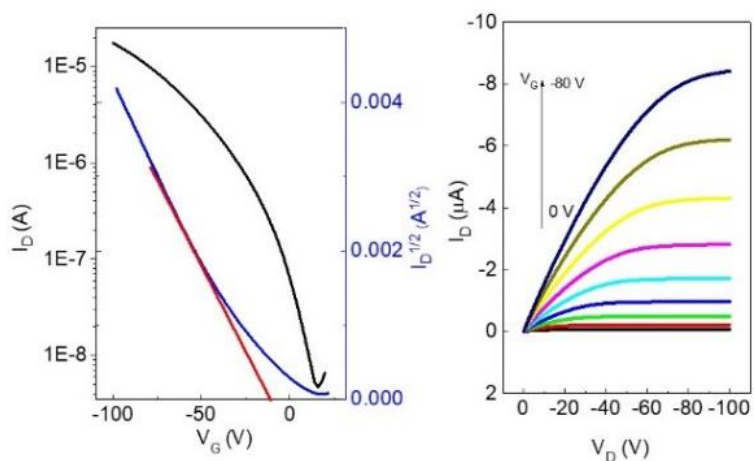
(f)

Figure 2.13 The transfer curves and output curves of OTFTs based on PDDBTA: (a) room temperature, (b) 50 °C, (c) 100°C, (d)150 °C, and (e) 200 °C, as well as P3HT annealed at 160 °C: (f). Device dimensions: channel length (L) = 30 µm; channel width (W) = 1000 µm. V_G varied from 0 V to -80 V in a step of -20 V in the output curves.

Table 2.2 OTFT device parameters of PDDBTA and P3HT at different annealing temperatures.

Polymer	Annealing[a] temperature	Average (maximum) hole mobility[b]	V_{th}[c] (V)	I_{on}/I_{off}

	(°C)	(cm^2 V^{-1} s^{-1})		
PDDBTA	r. t. (22)	0.018±0.003(0.021)	-37	10^4
	50	0.018±0.002(0.020)	-41	10^4
	100	0.021±0.002(0.023)	-45	10^4
	150	0.036±0.005(0.041)	-47	10^5
	200	0.033±0.013(0.040)	-45	10^5

[a] The devices were annealed in a glove box on a hotplate at the selected temperature for 20 min under argon. Hole mobilities were obtained in the saturated regions in hole enhancement modes. Each set of data were obtained from 3-5 OTFT devices.

[b] The average mobility ± standard deviation (maximum mobility) calculated from the saturation regions of the devices.

[c] The threshold voltage, V_{th}, was calculated for the device with the maximum mobility.

The hole mobilities are similar to those of P3HT (ca. 0.01 – 0.1 cm^2 V^{-1} s^{-1}) (**Table 2.3**), indicating that the incorporation of azine unit is not detrimental for the hole transport of the resultant polymer.[25]

Table 2.3 OTFT Performance comparison between PDDBTA and P3HT.

	OTFT performance (neat polymer)		
Polymer	Hole mobility ($cm^2\,V^{-1}\,s^{-1}$)	V_{th} (V)	I_{on}/I_{off}
P3HT[a]	0.02-0.1	/	10^3
P3HT[b]	0.01	-10	10^2
PDDBTA	0.041	-47	10^5

[a] Typical OTFT performance of P3HT reported in the literature.[94], [95].

[b] OTFT performance of P3HT with a HT% of 98% obtained in this work, which was purchased from 1-Material.

2.4.2 Air stability of PDDBTA-based OTFT devices

When the devices were tested in the ambient air with a relative humidity (RH) of 55%, the mobility dropped to 3.3×10^{-3} $cm^2\,V^{-1}\,s^{-1}$ in average for the 150 °C-annealed films (**Figure 2.14** & **Table 2.4**), an order of magnitude lower than that measured under argon. The rather polar azine unit in the polymer might be prone to absorption of moisture in the ambient air, negatively impacting the hole transport.[25]
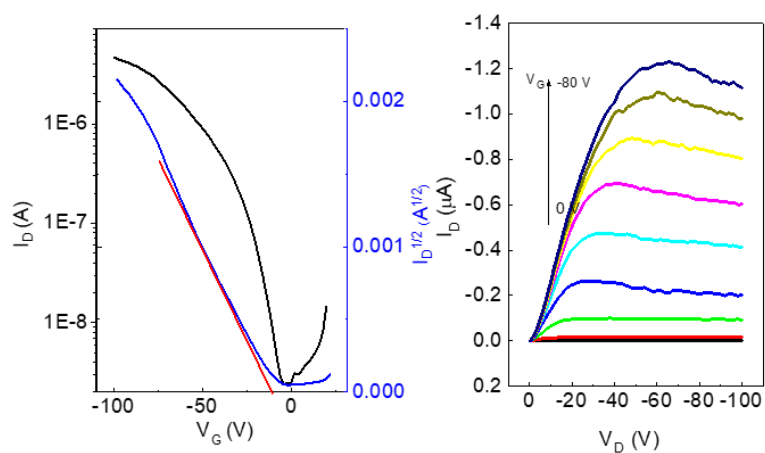
Figure 2.14 The transfer curves and output curves of OTFTs based on PDDBTA annealed at 150 °C tested in the air (relative humidity, RH = 55%). Device dimensions: channel length (*L*) = 30 µm; channel width (*W*) = 1000 µm. V_G varied from 0 V to -80 V in a step of -20 V in the output curves.

Table 2.4 Air stability of OTFT Performance based-on PDDBTA.

Polymer	Annealing[a] temperature (°C)	Average (maximum) hole mobility[b] (cm^2 V^{-1} s^{-1})	V_{th}[c] (V)	I_{on}/I_{off}
PDDBTA	150	0.036±0.005(0.041)	-47	10^5
PDDBTA in the air [a]	150	0.0033±0.0006(0.0039)	-12	10^4

[d] The devices were tested in ambient air with a relative humidity (RH) of 55%.

2.5 Characterization of OPVs for both PDDBTA and rr-P3HT

2.5.1 Photovoltaic performance

The photovoltaic performance of PDDBTA as a donor was studied in OPVs with an inverted structure (ITO / ZnO / active layer / MoO$_x$ / Ag) with phenyl-C$_{61}$-butyric acid methyl ester (PCBM) as the acceptor. **Table 2.5** shows the influence of different D:A ratios and film thickness on power conversion efficiency, and the highest PCE based-on PDDBTA: PCBM corresponded to the D: A of 1:2 and a film thickness of 120nm. The current density–voltage (J-V) curve of the optimized device, which has a PDDBTA:PCBM ratio of 1:2, is shown in **Figure 2.15**. The device showed a short circuit current density (J$_{SC}$) of -4.70 mA cm^{-2}, a V$_{OC}$ of 0.73 V, and a fill factor (FF) of 0.64, corresponding to a PCE of 2.18 %. Compared to the OPV fabricated with a

P3HT:PCBM (1 : 1) blend active layer, which showed a J_{SC} of 7.79 mA cm^{-2}, a V_{OC} of 0.59 V, a FF of 0.65, and a PCE of 2.95%.[25]

Table 2.5 Optimization of OPV performance.

D:A ratio				
Ratio	J_{SC} (mA cm^{-2})	V_{OC} (V)	FF	PCE (%)
1:2	**-4.70**	**0.73**	**0.64**	**2.18**
1:1	-4.61	0.78	0.48	1.72
2:1	-2.51	0.89	0.31	0.69
Thickness optimization (D:A ratio = 1:2)				
120 nm	**-4.70**	**0.73**	**0.64**	**2.18**
150 nm	-4.88	0.68	0.64	2.13
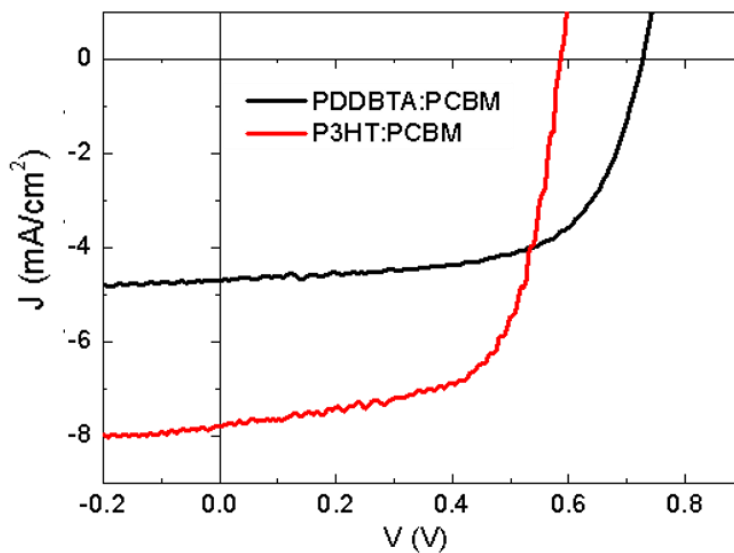
Figure 2.15 J-V curves of OPV devices having PDDBTA:PCBM (1:2) and P3HT:PCBM (1:1) as the active layers, respectively.

Obviously, the PDDBTA:PCBM device has a higher V_{OC}, which is due to the deeper HOMO level of PDDBTA (-5.55 eV) than that of P3HT (-5.14 eV). The attainable V_{OC} of an OPV device for a donor:PCBM system can be estimated by an empirical equation: $eV_{OC} = E_{g\_eff} - 0.3$ eV, where E_{g_eff} is effective donor–acceptor energy gap (E_{LUMO} (PCBM) $- E_{HOMO}$(donor)), e is the elementary charge, and 0.3 eV is an energy loss including the energy required to offset the exciton binding binder energy of an exciton.[33], [34] If a LUMO level for PCBM (E_{LUMO} (PCBM)) of -4.3 eV is taken,[33] the estimated attainable V_{OC} for the PDDBTA:PCBM based device would be 0.95 V. The lower-than-expected V_{OC} obtained for the PDDBTA : PCBM OPVs indicates a large energy loss, which is likely caused by the poor film morphology of the active layer.[34] On the other hand, the J_{SC} of the PDDBTA:PCBM device is much lower than that of the P3HT:PCBM device. The external quantum efficiency (EQE) spectrum of the PDDBTA:PCBM device showed pretty low EQE of ca. 30% in the photovoltaically active 350-600 nm region (**Figure 2.16**).[25]
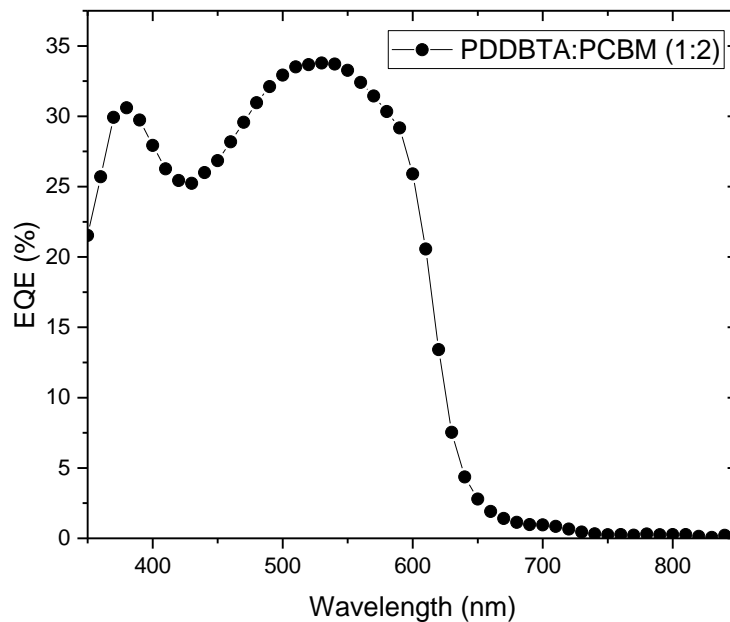
Figure 2.16 External quantum efficiency (EQE) spectrum of an unencapsulated PDDBTA:PCBM (1:2) based OPV device. The integrated J_{SC} was calculated to be 4.45 mA cm^{-2}.

To investigate the cause for the significantly lower J_{SC} of the PDDBTA:PCBM devices, photoluminescence quenching experiments were carried out to characterize the effectiveness of exciton diffusion and charge transfer from donor to PCBM acceptor phase of the active layer. A photoluminescence quenching of 97% was observed for the PDDBTA:PCBM blend with respect to the photoluminescence of donor (**Figure 2.17**), which suggests that the exciton diffusion from the donor phase to the donor-acceptor interface and the subsequent exciton dissociation processes were quite efficient. [25]
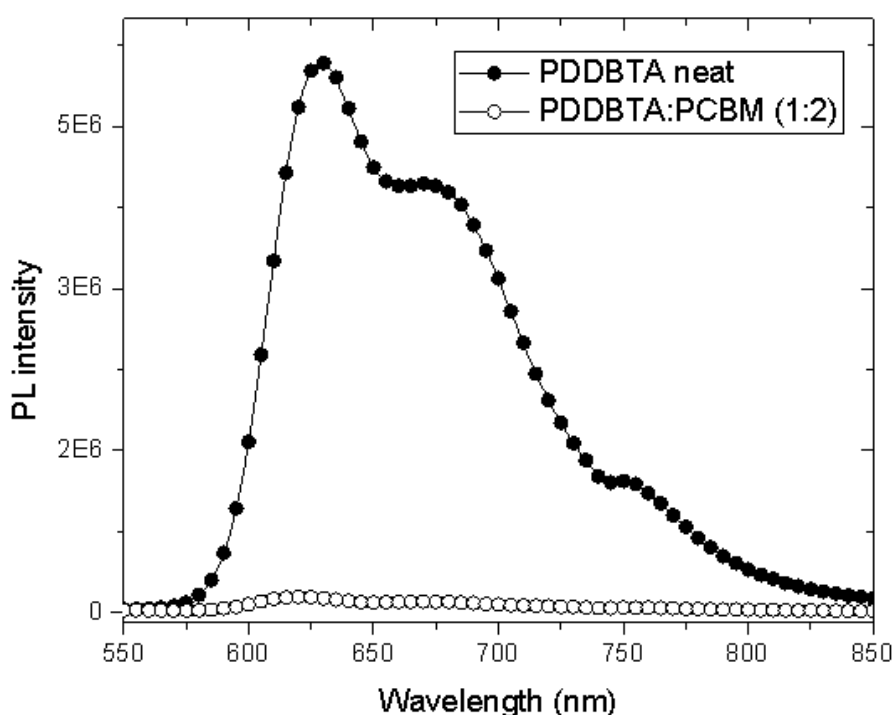
Figure 2.17 Photoluminescence (PL) quenching data for neat PDDBTA and PDDBTA:PCBM (1:2) blend films on glass substrates at an excitation wavelength of 510 nm. Three vibronic transition peaks at 630, 670, and 751 nm from PDDBTA were observed. The integrated PL intensity of PDDBTA: PCBM film is 3% that of the neat PDDBTA film, that is, the

photoluminescence of the PDDBTA: PCBM film is 97% quenched compared to the neat PDDBTA film.

The new polymer PDDBTA showed comparable performances compared to those of P3HT in OTFTs and OPVs (**Table 2.6**). The FF of the PDDBTA-based device was 65, which was almost the same as that of P3HT-based devices not only made by our group but also from some literatures. The value of V_{OC} significantly increased compared with P3HT devices which demonstrated the target of this polymer. On the contrary, what limited PCE was the relatively low J_{SC}, the detailed explanations will be described under further characterization. Overall, the OPV performance of PDDBTA: $PC_{61}BM$-based OSCs reached same level of P3HT ones, and there was a lot of room and potential to improve by enhancing J_{SC}.

Table 2.6 OPV performance comparison between PDDBTA and P3HT.

Polymer	OPV performance (polymer:PCBM blend)			
	J_{SC} (mA cm^{-2})	V_{OC} (V)	FF (%)	PCE (%)
P3HT[a]	7.3-11.5	0.56-0.61	48-67	2.25-5
P3HT[b]	7.79	0.59	65	2.95
PDDBTA[c]	4.7	0.73	64	2.18

[a] Typical OPV performance of P3HT:PCBM blend reported in the literature.[55][69–73]

[b] OTFT performance of P3HT and OPV performance of P3HT:PCBM obtained in this work, where P3HT with a HT% of 98% was purchased from 1-Material.

[c] The best performance obtained in this work for an OPV device with a PDDBTA:PCBM ratio of 1:2.

2.5.2 The space charge limited current (SCLC) mobilities

The SCLC hole mobility was measured using a device architecture of ITO / PEDOT:PSS / polymer film / MoO$_x$ /Ag, while the SCLC electron mobility was measured using a device architecture of ITO / ZnO / polymer film / LiF / Al.

The SCLC mobility was obtained by taking current–voltage curves and fitting the results using the following equation:

$$J_{sclc} = \frac{9}{8}\mu\varepsilon \frac{V_{appl}^2}{d^3}$$

where $\varepsilon = \varepsilon_o\varepsilon_r$, ε_o is the permittivity of free space, ε_r is the relative permittivity of the material (assumed to be 3), μ is the SCLC mobility, $V_{appl} = V - V_{bi}$ is the applied voltage corrected for built in potential V_{bi}, and d is the thickness of the film.[25]

After the exciton diffusion and dissociation, the free charge carriers, holes and electrons, need to transport to and be collected by the anode and cathode, respectively. The critical parameters governing this step are the hole and electron mobilities in the respective donor and acceptor phases. The space charge limited current (SCLC) mobilities, which represent the vertical charge transport in OPVs in comparison to the lateral charge transport in OTFTs, were measured to further study the cause for the lower J$_{SC}$ of the PDDBTA:PCBM based OPV devices (**Table 2.7**). The neat PDDBTA films showed the highest SCLC hole mobility of 7.75×10^{-6} cm^2 V^{-1} s^{-1}, which is much lower than that of the neat P3HT films (3.24×10^{-4} cm^2 V^{-1} s^{-1}). In the PDDBTA:PCBM (1:2) blend, the SCLC hole mobility further decreased to 3.71×10^{-6} cm^2 V^{-1} s^{-1}, while the SCLC electron mobility was also found to be low at 5.78×10^{-6} cm^2 V^{-1} s^{-1}. Both the SCLC hole and electron mobilities of the PDDBTA:PCBM blend were 2-3 orders of magnitude lower than those for the P3HT:PCBM blend ($\sim 10^{-3}$ cm^2 V^{-1} s^{-1} for the hole mobility and $\sim 10^{-4}$ cm^2 V^{-1} s^{-1} for the electron mobility).[96] The low SCLC mobilities of the PDDBTA:PCBM blend are thus considered contributing to the loss of charge carriers, leading to lower J$_{SC}$. The AFM height and phase images of the blend film

showed very large (ca. 100's nm in size) and poorly connected grains (**Figure 2.18**), which would form discontinuous pathways for charge carrier transport. This poor morphology might also contribute to the lower-than-expected V_{OC} of the PDDBTA:PCBM devices as discussed previously.[25]

Table 2.7 SCLC mobility data.

	Electron mobility ($cm^2 V^{-1} s^{-1}$)		Hole mobility ($cm^2 V^{-1} s^{-1}$)	
	Maximum	Average [SD][b]	Maximum	Average [SD][b]
PDDBTA	/	/	7.75×10^{-6}	6.50×10^{-6} [1.15×10^{-6}]
PCBM[a]	/	2×10^{-3} [2.00×10^{-4}]	/	/
PDDBTA:PCBM (1:2)	5.78×10^{-6}	2.86×10^{-6} [2.01×10^{-6}]	3.71×10^{-6}	2.89×10^{-6} [5.02×10^{-7}]
P3HT	/	/	3.23×10^{-4}	2.63×10^{-4} [3.35×10^{-5}]
P3HT:PCBM (1:1)[a]		1×10^{-3}		3×10^{-4}

[a] From Reference[96]

[b] SD: standard deviations.
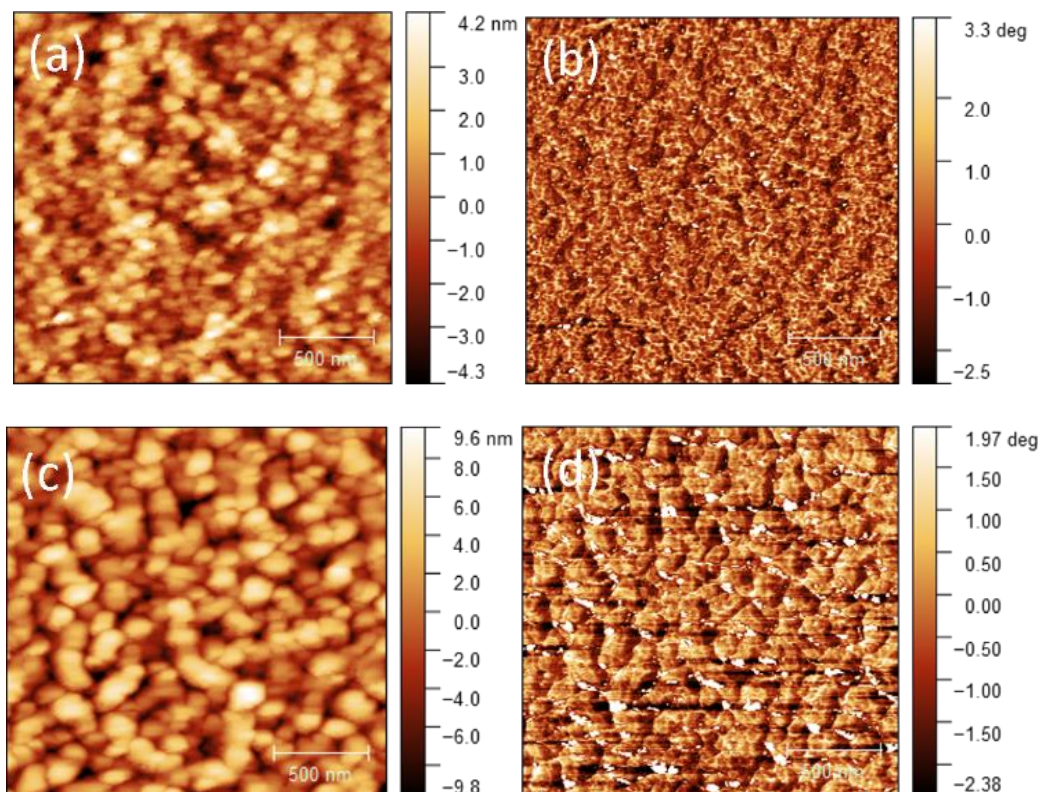
Figure 2.18 AFM height images of (a) neat PDDBTA (c) PDDBTA:PCBM (1:2) blend films on ITO substrates. The corresponding phase images are shown in (b) and (d), respectively. RMS roughness for neat and blend films are 1.3 nm and 3.4 nm respectively.

2.5.3 Air stability of PDDBTA-based OPV devices

The unencapsulated PDDBTA:PCBM based OPV devices showed remarkable stability with ~10% drop in PCE after 200 hr of storage under ambient conditions (at 22 °C and with an RH of 55%)(**Figure 2.19**). In comparison, in a study of air stability of OPV devices using some common polymer donors paired with PCBM acceptor, the unencapsulated devices with similar structures showed PCE drops of 35% for P3HT:PCBM, 50% for PTB7:PCBM and 75% for PBDTTT-EFT (or PCE10):PCBM after 200 hr of shelf storage under ambient conditions.[97] The good stability of the PDDBTA:PCBM based OPV devices indicates that PDDBTA is quite stable both chemically and morphologically in the active layer.[25]
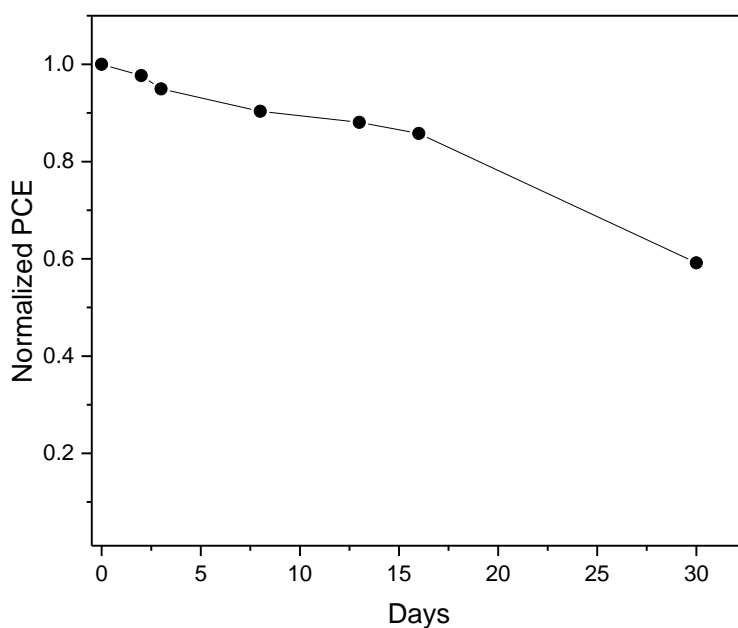
Figure 2.19 Stability of an unencapsulated PDDBTA:PCBM (1:2) solar cell stored in the ambient air at room temperature (22 °C) with a relative humidity (RH) of 55%.

2.6 Conclusion and future directions

In conclusion, we have synthesized a new bithiophene-azine polymer PDDBTA in a very simple process. This polymer showed good hole mobility of up to 4.1×10^{-2} cm^2 V^{-1} s^{-1} in OTFTs. Moreover, this polymer can be used as a donor in OPVs, achieving PCEs of up to 2.18%, which is the first example of using an azine-based semiconductor polymer in OPVs. These preliminary results demonstrate that the bithiophene-azine polymers and other azine-based polymers may be a new class of low-cost polymer semiconductors that are suitable for mass production of organic solar cells and other printed electronics.[25] However, the solubility and partially aggregation due to high level of crystallinity of active layer limits the performance, which might be improved by side chain optimization or backbone replacement to gain a better active layer morphology

46

or a higher value of SCLC mobilities or a more balanced electron and hole charge carrier mobilities, thereby result in larger J_{SC} and FF.

2.7 Experimental section

2.7.1 Synthesis of 4,4'-didodecyl-2.2'-bithiophene
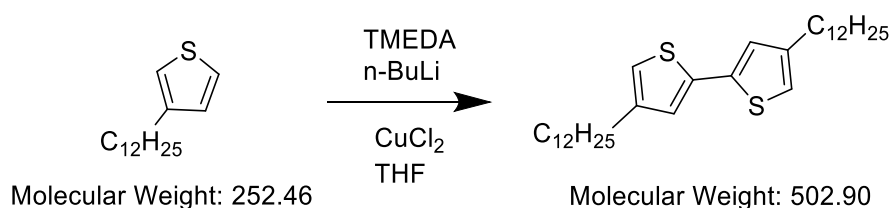
Scheme 2.2 Synthesis of 4,4'-didodecyl-2.2'-bithiophene

3-dodecylthiophene (3.8 g, 15.05 mmol) was dissolved in 30ml THF, TMEDA (2.47 ml, 16.56 mmol) and n-BuLi (15.05 mmol) was slowly added at 0 C. The solution mixture was heated to 50°C for 1 h and then cooled to -78 °C. CuCl$_2$ (2.23g, 16.56 mmol) was added in one portion. After being stirred for about 40 min, the mixture was warmed to room temperature and was kept overnight. Water was added to end this reaction, and the residue mixture was extracted with ether. The combined organic phase was washed with water, brine, dried with Na$_2$SO4, and the solvent was removed under reduced pressure. Then the crude product was purified by column chromatography with pure hexane to give the target material as bright yellow powder. Yield:1.21g (34%)^{1}H NMR (300 MHz, CDCl$_3$, ppm) δ: 6.96 (s, 2H), 6.75 (s, 2H), 2.57-2.52 (t, 4H), 1.62-1.57 (m, 4H), 1.24 (m, 36H), 0.88-0.84 (t, 6H).

300 MHz ^{1}H NMR spectrum, with peaks labeled at 7.24, 6.96, 6.95, 6.75, 6.74, 2.57, 2.54, 2.52, 1.62, 1.59, 1.57, 1.51, 1.30, 1.29, 1.26, 1.24, 0.88, 0.86, 0.84 ppm

4,4'-didodecyl-2,2'-bithiophene
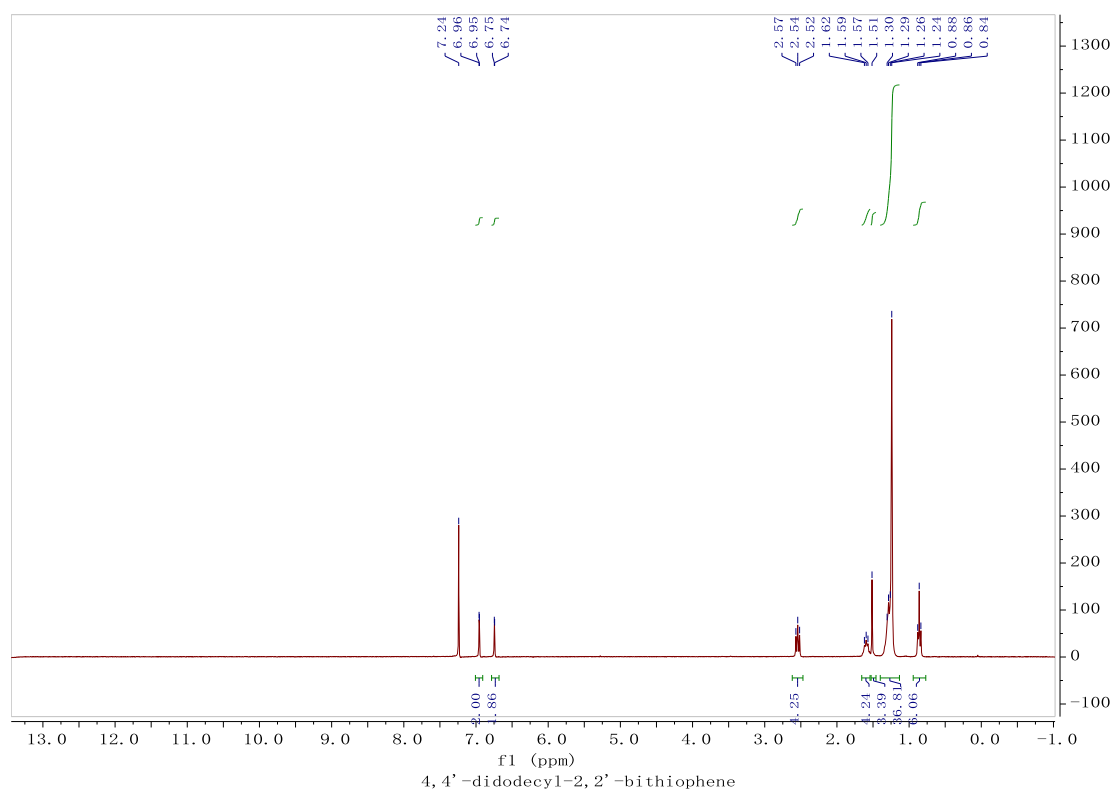
Figure 2.20 300 MHz ^{1}H NMR spectrum for 4,4'-didodecyl-2,2'-bithiophene in Chloroform-*d*.

2.7.2 Synthesis of 4,4'-didodecyl-2,2'-bithiophene-5,5'-dicarboxaldehyde (monomer)

Molecular Weight: 502.90 → (n-BuLi, DMF, ether) → Molecular Weight: 558.92
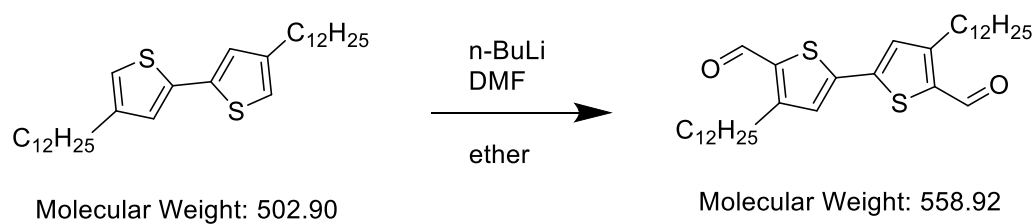
Scheme 2.3 Synthesis of 4,4'-didodecyl-2,2'-bithiophene-5,5'-dicarboxaldehyde

A 4.62 ml of n-BuLi/hexane 2.5 M solution was dropped to a stirred solution of 4,4'-dodecyl-2,2'-bithiophene (1.0 g, 1.78 mmol) in anhydrous ether (25 mL) at 0°C under N$_2$. Then the solution was stirred for 1 h at this temperature and refluxed for 2h. After cooling to room temperature, excess anhydrous DMF was added in one portion. The

mixture was refluxed for 2 h then poured into water, extracted with ethyl acetate. ,washed with brine and dried with Na$_2$SO4, then the solvent was evaporated under reduced pressure. The crude product was purified by column chromatography on silica (eluent: dichloromethane: hexane=2:1(v:v)).Yield: 67%(670 mg).^{1}H NMR (300 MHz, CDCl$_{3,}$ ppm) δ: 10.0 (s, 2H), 7.17 (s, 2H), 2.94-2.89 (t, 4H), 1.67(m, 4H), 1.24 (m, 36H), 0.88-0.83 (t, 6H)

4,4'-dodecyl-2,2'-bithiophene-5,5'-dicarboxaldehyde
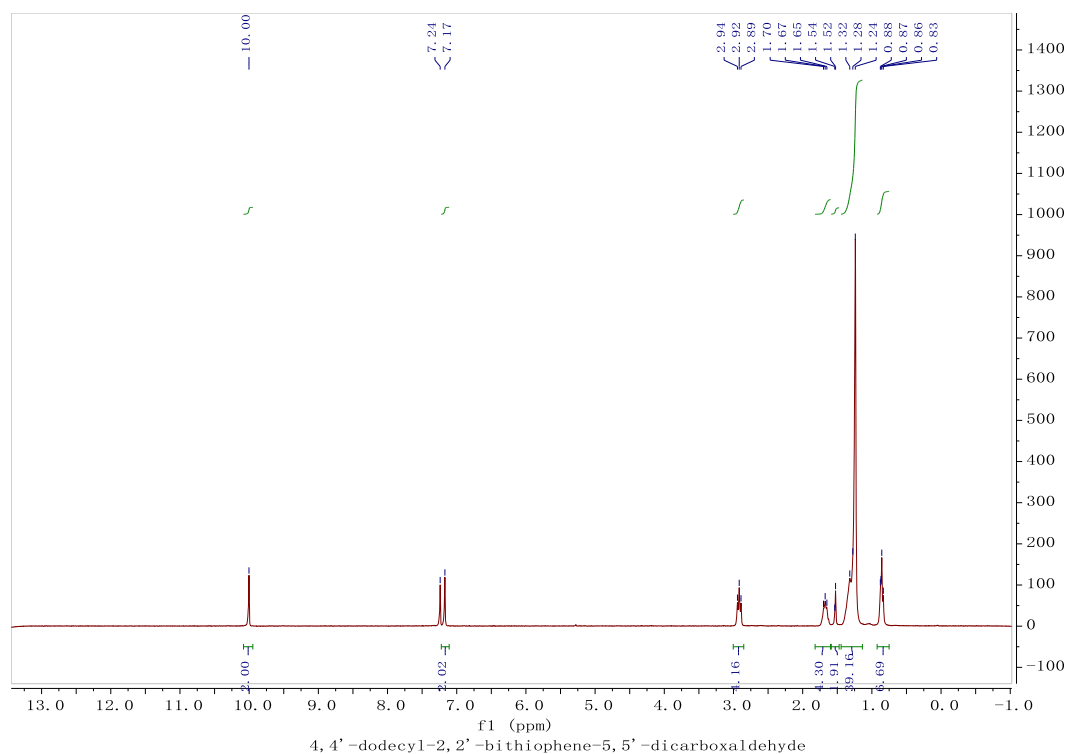
Figure 2.21 300 MHz **^{1}H NMR spectrum for** 4,4'-didodecyl-2,2'-bithiophene-5,5'-dicarboxaldehyde in chloroform-*d*.

2.7.3 Fabrication of OTFT devices and hole mobility calculation method

The field effect hole mobility of polymers was measured in OTFT devices with a bottom-gate bottom-contact (BGBC) configuration. The OTFT devices were fabricated as follows.

First, gold source and drain pairs were patterned on a heavily n-doped SiO₂/Si wafer with 300 nm thickness of SiO_2 by conventional photolithography and thermal deposition techniques. Then, the wafer was cut into small square wafers (ca. 1 cm × 1 cm), which were sonicated in acetone in an ultrasonic bath for 20 min at room temperature. Subsequently, acetone was removed and 2-propanol (IPA) was added followed by ultrasonication for an additional 20 min. After sonication, the wafers were dried by using nitrogen gas and treated with oxygen plasma for 2 min with a low air flow. Wafers were immersed into pure ethanol, chloroform, a 10 mM solution of octadecanethiol in ethanol for 1 h and pure ethanol in a covered petri dish successively. Then, wafers were immersed in 100 mL DI water in covered petri dish, and four drops of a solution of HNO_3 : HCl : H_2O (1 : 10 : 10) were added. The wafers were kept for 1 min, taken out and rinsed with deionized water. The wafers were dried with nitrogen gas and subsequently on hot plate at 120 °C for 10 min. Subsequently, the wafers were put in a solution of dodecyltrichlorosilane (DDTS) in toluene (3% DDTS) at room temperature for 20 min. The wafers were then rinsed with toluene and dried under a nitrogen flow. Then a polymer solution in chloroform (5 mg mL⁻¹) was spin-coated onto the wafer at 1000 rpm for 60 s to obtain a polymer film, which was optionally subjected to thermal annealing at different temperatures for 20 min in an argon-filled glove box. All the OTFT devices have a channel length (*L*) of 30 μm and a channel width (*W*) of 1000 μm and were characterized in the same glove box using an Agilent B2912A Semiconductor Analyzer. The hole mobility was calculated in the saturation regime according to the following equation:

$$I_{DS} = \frac{\mu C_i W}{2L}(V_G - V_T)^2$$

where I_{DS} is the drain-source current, μ is charge carrier mobility, C_i is the gate dielectric layer capacitance per unit area (~ 11.6 nF cm^{-2}), V_G is the gate voltage, V_T is the threshold voltage, L is the channel length (30 μm), and *W* is the channel width (1000 μm).[25]

2.7.4 Fabrication and characterization of OPV devices

Solar cells with a configuration of ITO (150nm) / ZnO (40nm) / Active layer / MoO_x (10nm) / Ag (100nm) were fabricated as follows.

The ITO glass substrates were cleaned in an ultrasonic bath in deionized water and acetone for 20 min each at 40 °C. The substrates were then taken out and cleaned by clean Q-tips soaked with acetone. The substrates were then sonicated again for 20 min at 40 °C in IPA. The substrates were dried with a nitrogen flow and cleaned in an air plasma chamber for 10 min. A ca. 40 nm thin layer of ZnO was deposited by spin-coating a freshly prepared ZnO precursor solution (by mixing zinc acetate (197 mg), ethanolamine (54 µl), 2-methoxyethanol (2 ml) under stirring vigorously at 50 ℃ overnight) at 3500 rpm and annealed subsequently at 200 °C for 1 h in air. Then the substrates were transferred to a nitrogen filled glove box, where the PDDBTA (or P3HT) and the PCBM blend (36 mL^{-1}mg total in 1,2-DCB in the ratio 1:2 (donor: acceptor)) layer with a thickness of 120 nm was spin-coated onto the ZnO layer at 1000 rpm (the donor:acceptor ratio and thickness were optimized as shown in **Table 3.4**). The substrates were taken out and a thin layer of MoO_x (10 nm) and an Ag (100 nm) electrode were deposited onto the substrate using a thermal evaporator at pressure < 5.0 × 10^{-6} Pa. The active area was 0.0574 cm^2. The current density–voltage (*J-V*) characteristics of the polymer solar cells were measured on an Agilent B2912A Semiconductor Analyzer with a ScienceTech SLB300-A Solar Simulator. A 450 W xenon lamp and an air mass (AM) 1.5 filter were used as the light source.[25]

Chapter 3 Improvements of the polymer based-on PDDBTA

3.1 Introduction

Further efforts were designed to improve the solubility and compatibility of the previous azine polymer mixed with PCBM in order to improve the film morphology. We determined to change the long straight dodecyl carbon side chains on thiophene rings to short branch ones with eight carbons, which are 2-ethylhexyl chains (shown in **Scheme 3.1**).
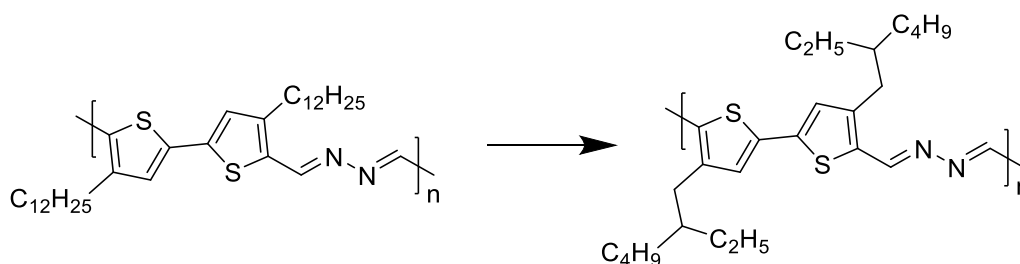
Scheme 3.1 Side chain optimization design.

Another improvement is to change the backbone of the polymer by replacing thiophene rings. Pyrrole-based conjugated polymers also showed good optical and optoelectronic properties.[98]–[100] Polypyrrole also showed a wide absorption wavelength of light up to about 650 nm.[101] The good conductivity and its effects on electron extraction-charge carrier recombination and morphology also help achieve performance on solar cell applications. [102], [103] However, the HOMO level of PPY (polypyrrole) was measured as about 0.4 V compared to the I^-/I_3^-,[104] which is also too high to match with PCBM as a donor material in D-A OSCs. Therefore, adding azine groups might play the same role as in previous project that they can help lower the HOMO level. Then a DFT

simulation for a pyrrole-azine unit was also necessary before synthesis and the results are shown in **Figure 3.1**. After adding an azine group next to a pyrrole ring, the HOMO level of the pyrrole-azine group is -5.67 eV, which is lower than that of bithiophene theoretically.
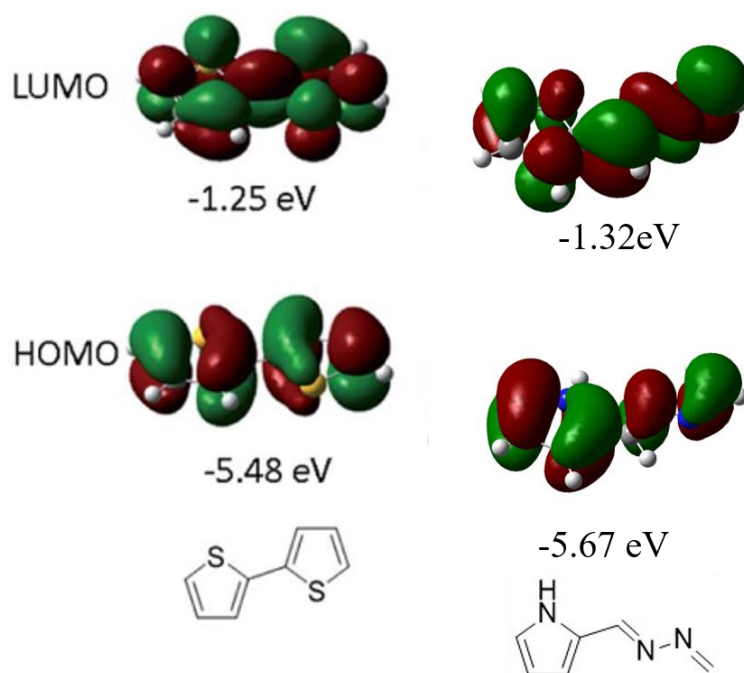
Figure 3.1 HOMO/LUMO orbitals and energy levels (with respect to vacuum, 0 eV) of bithiophene and pyrrole-azine calculated using the density functional theory (DFT) with the same conditions as **Figure 2.1**.

3.2 Synthesis and characterization of poly(4,4'-di(2-ethylhexyl)-2,2'-bithiophene-azine) (PDEHBTA)

3.2.1 Synthesis of PDEHBTA

PDEHBTA1:

Molecular Weight: 446.71
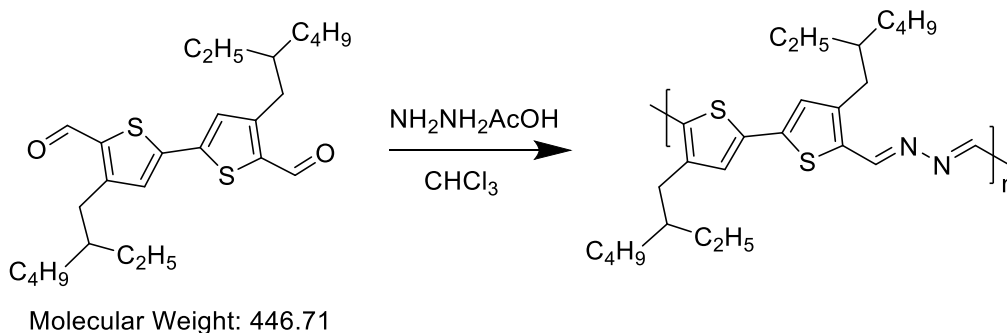
Scheme 3.2 Synthesis of poly(4,4'-di(2-ethylhexyl)-2,2'-bithiophene-azine).

4,4'-Di(2-ethylhexyl)-2,2'-bithiophene-5,5'-dicarboxaldehyde (500 mg, 1.19 mmol) and hydrazine acetate (103.1 mg, 1.19 mmol) were added into a double-neck round-bottom flask. After being refilled with argon three times, chloroform (4.5 mL) was added. The solution was heated to 85 °C for 20 h. Three drops of 2-thiophenecarboxaldehyde were added as termination. After 40 min, the mixture was cooled down to room temperature and poured into stirring methanol (100 mL), followed by Soxhlet extraction with acetone, hexane, heptane and chloroform. The chloroform fraction was precipitated in methanol and was filtered then dried to afford the target polymer as a dark solid. Yield: 215 mg (42.9%).

M_w = 5.6 kD; M_n = 1.3 kD; PD = 4.26 (The molecular weight was measured by low temperature GPC), the molecular weight was relatively low. Considering that chloroform is acidic and hydrazine acetate is alkaline, using a neutral solvent might be a better choice, since the purity of monomer had been over 98% which was clean enough for a polymerization. Furthermore, the shorter branch side chain is pretty close to a functional group (aldehyde group), which may also cause a problem of steric hindrance.

PDEHBTA2:

Molecular Weight: 446.71
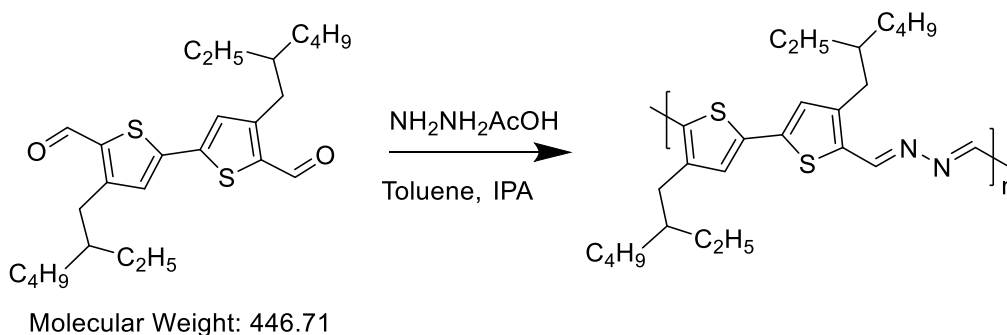
Scheme 3.3 Synthesis of poly(4,4'-di(2-ethylhexyl)-2,2'-bithiophene-azine).

4,4'-Di(2-ethylhexyl)-2,2'-bithiophene-5,5'-dicarboxaldehyde (304.3 mg, 0.681 mmol) and hydrazine acetate (63.1 mg, 0.685 mmol) with 0.5 ml IPA were added into a double-neck round-bottom flask. After being refilled with argon at room temperature three times, toluene (3 mL) was added. The mixture was heated to 90°C for 48 h. Then the mixture was cooled down to room temperature without termination and was poured into stirring methanol (100 mL), followed by Soxhlet extraction with acetone, hexane, heptane and chloroform. The chloroform fraction was precipitated in methanol and was filtered then dried to afford the target polymer as a dark solid. Yield: 89.3 mg (29.3%).

M_w = 7.2 kD; M_n = 2.7 kD; **PD** = 2.68. (low temperature GPC) The molecular weight increased to some extent but may still not high enough to show a satisfactory property.

3.2.2 Characterization of PDEHBTA2

The onset of oxidation curve started at a potential of 0.74 V, and a HOMO level of -5.54 eV can be estimated (**Figure 3.2**). There was no reduction peak for this polymer and the LUMO level was calculated through the HOMO level and the band gap energy from UV-vis spectra (**Figure 3.3**) to be -3.54 eV. The HOMO level of PDEHBTA2 is still lower than that of rr-P3HT but is similar to that of PDDBTA.
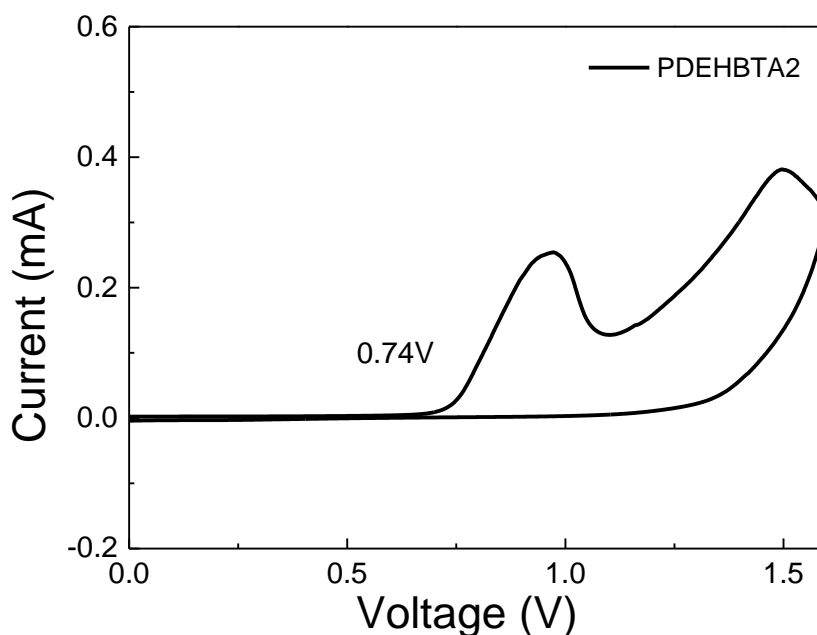
Figure 3.2 Cyclic voltammograms of PDEHBTA film measured in tetrabutylammonium fluoride (0.1 M) solution in acetonitrile using Ag/AgCl as the reference electrode.

The wavelength of maximum absorbance for PDEHBTA2 in a $CHCl_3$ solution was 510.8 nm as shown in **Figure 3.4**, while an obvious red-shift with a maximum absorbance at 532.4 nm was observed along with a shoulder peak at 574.3 nm (**Figure 3.3**). After annealed at 150 °C for 20 min, the intensities of the maximum peak at 532.4 nm and shoulder peak at 574.3 nm intensified with a 3nm red shift. The bandgap of PDEHBTA2 was calculated from the onset wavelength of absorption curve to be 2.00 eV, which is wider than that of P3HT (1.91 eV).
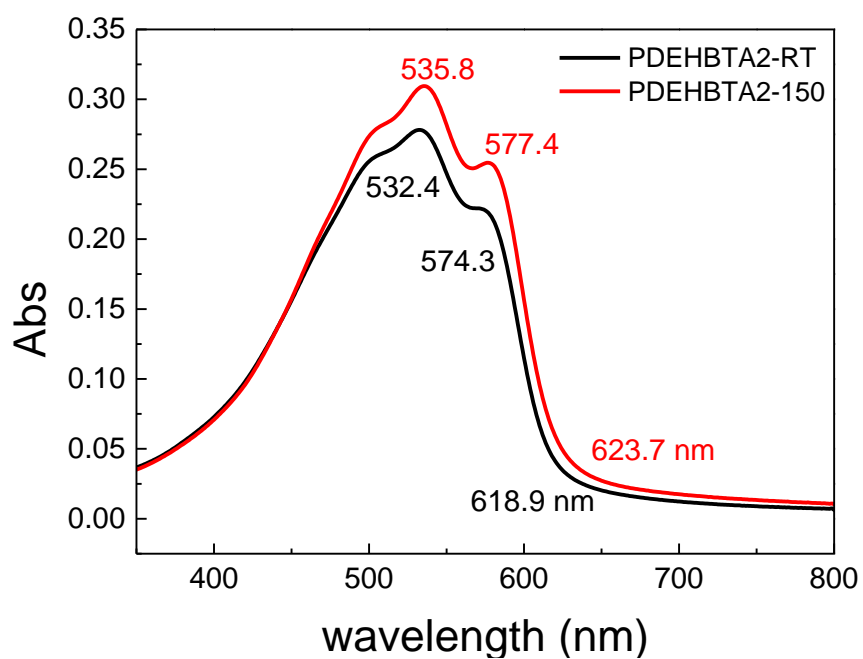
Figure 3.3 UV-vis absorption spectra of PDEHBTA2 films at room temperature and annealing to 150°C.
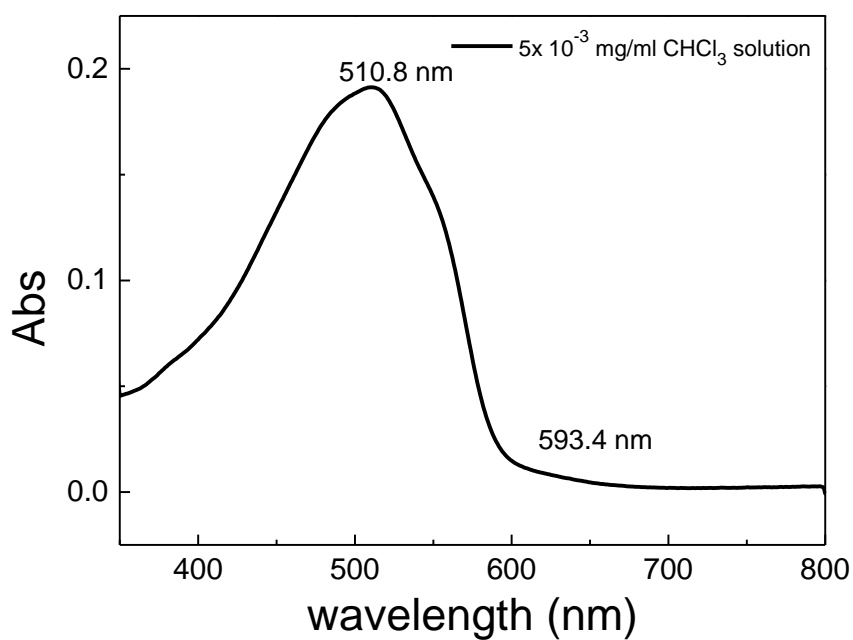
Figure 3.4 UV-vis absorption spectra of PDEHBTA2 in solution in chloroform.

Figure 3.5 shows the TGA curve that the total weight of PDEHBTA2 maintained 99.2% after heated to 290.2°C, which showed a good thermal stability
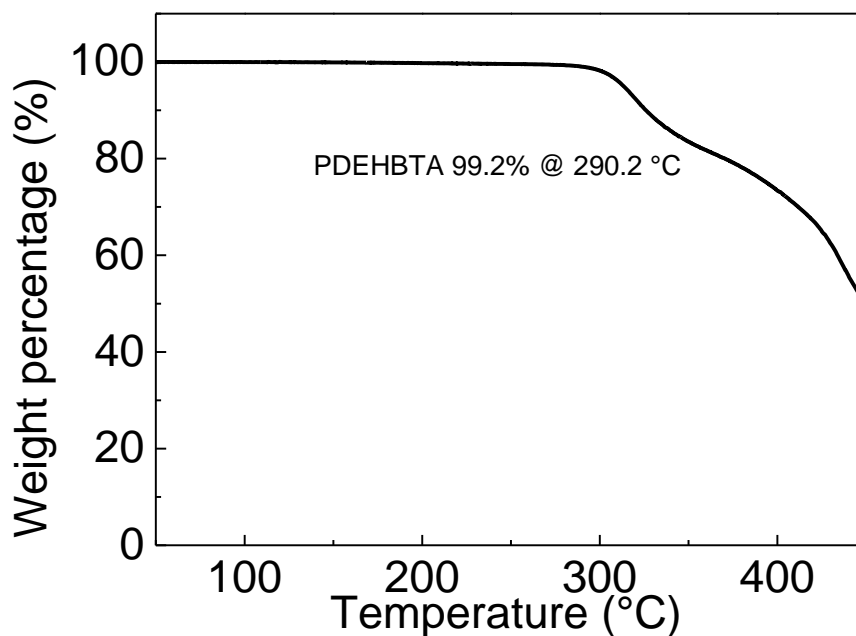
Figure 3.5 The TGA curve of PDEHBTA2 obtained at a heating rate of 10 °C min^{-1} under nitrogen.

DSC results of PDEHBTA2 were summarized in Figure 3.6. During the first heating scan (**Figure 3.6** from -20 °C to 250 °C), two broad peaks at 125.3 °C during heating process and 113.1°C during cooling process were observed, but the temperature need to be increased during the second heating/cooling cycle in order to confirm if the peaks were melting/crystallization points for side chain or backbone. After the heating temperature reached 280 °C (**Figure 3.6** -20 °C to 280 °C), the two broad peaks were hard to see, which indicated that they corresponded to a melting process for side chain during first heating cycle. During the second heating scan, the melting temperatures for the polymer sample appeared at 252.4°C, after cooling, a melting temperature appeared at 207.8 °C, which represented the crystallization of the PDEHBTA2 backbone.
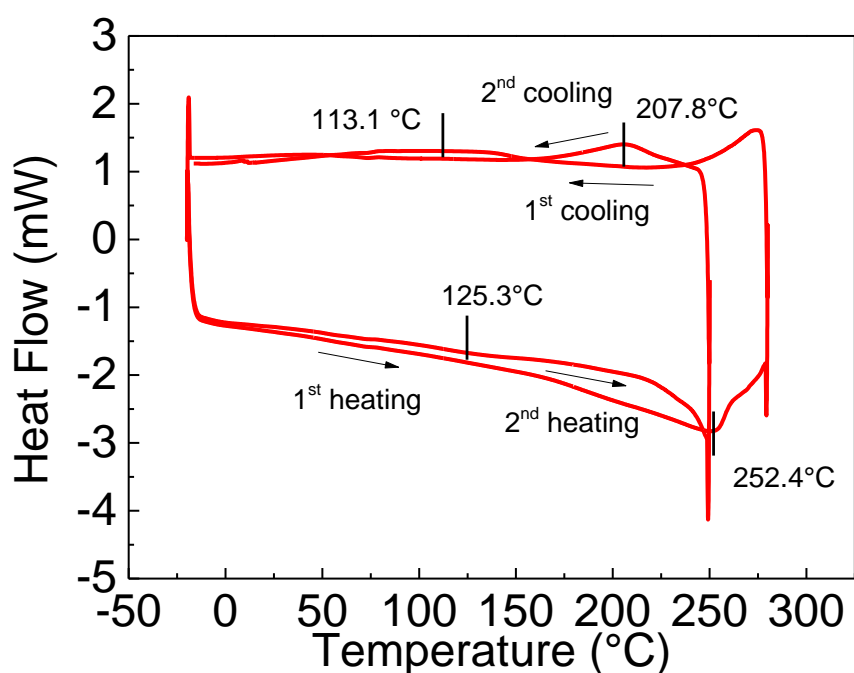
Figure 3.6 DSC diagrams of PDEHBTA2 measured at a heating rate of 5 °C min^{-1} under nitrogen.

3.2.3 OTFTs performance based-on PDEHBTA2

PDEHBTA2 showed a hole mobility of 3.2×10^{-3} cm^2 V^{-1} s^{-1} with a threshold voltage of -32 V (**Table 3.1**) according to the lower HOMO level. After annealing at 100 °C for 20 min, the mobilities increased to 3.4×10^{-3} cm^2 V^{-1} s^{-1} (**Table 3.1 and Figure 3.7**), and there was no performance for as-spun film when annealed at 150 °C, mainly due to the decomposition of this polymer. Compared to the samples processed by different annealing temperatures, the hole mobilities of them only increased a little bit, and as shown in AFM images (**Figure 3.8**), the roughness and crystallinity level of the thin film increased before 50 °C followed by showed a downward trend from 50 °C to 150 °C.

Table 3.1 OTFT device parameters of PDEHBTA2 at different annealing temperatures.

Polymer	Annealing[a] temperature (°C)	Average (maximum) hole mobility[b] ($cm^2\ V^{-1}\ s^{-1}$)	V_{th}[c] (V)	I_{on}/I_{off}
PDEHBTA2	r. t. (22)	$2.6 \times 10^{-4} \pm 4 \times 10^{-5}$ (3.2×10^{-3})	-32	10^3
	50	$2.9 \times 10^{-4} \pm 2 \times 10^{-5}$ (3.1×10^{-3})	-33	10^3
	100	$3.2 \times 10^{-4} \pm 2 \times 10^{-5}$ (3.4×10^{-3})	-29	10^3
	150	No Performance		

[a] Each set of data were obtained from 3-4 OTFT devices.
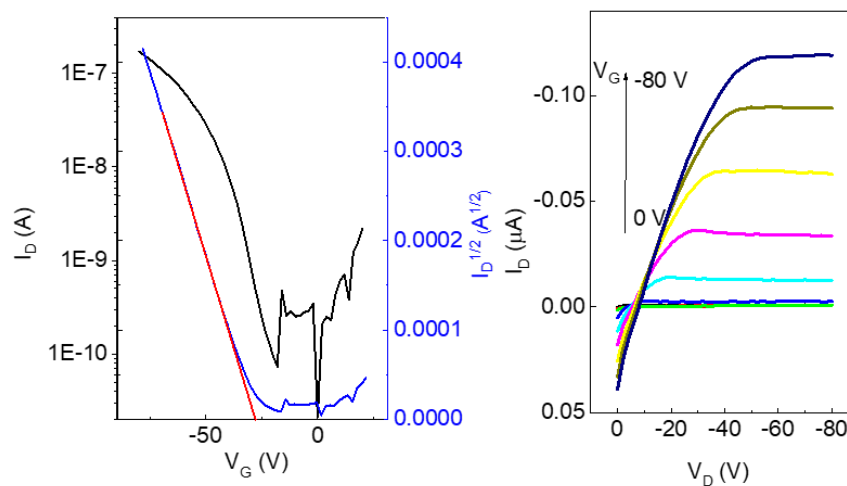
Figure 3.7 The transfer curves and output curves of OTFTs based on PDEHBTA2 annealed at 100°C. Device dimensions: same with PDDBTA devices tested previously.
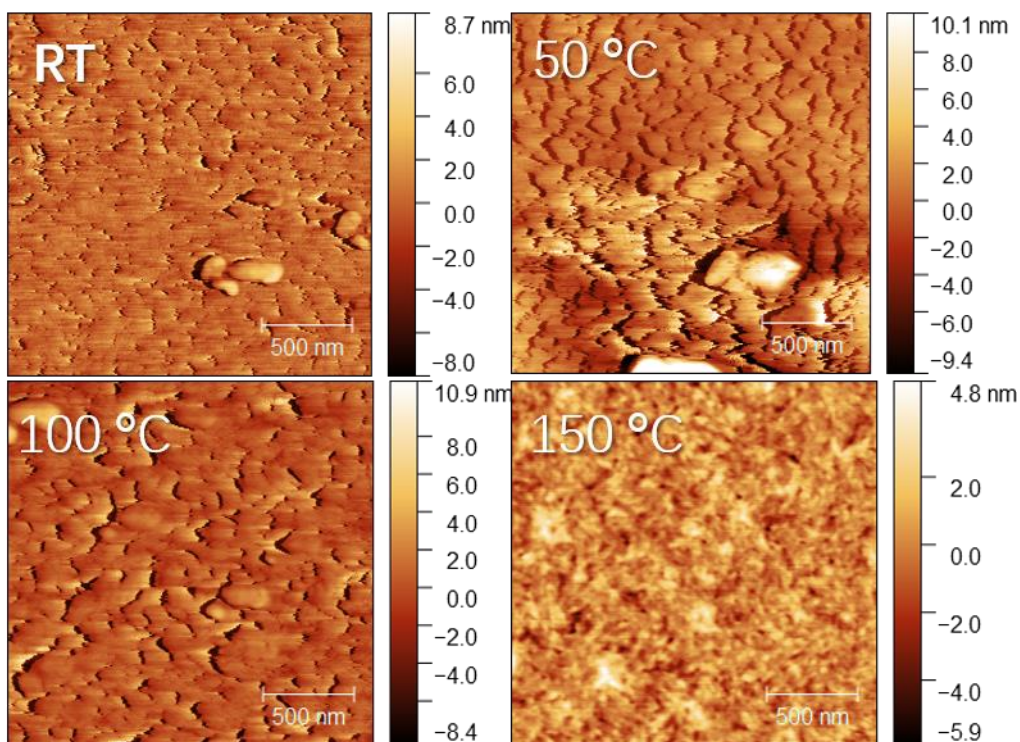
Figure 3.8 AFM height images of neat PDEHBTA2 films on SiO2/Si wafers annealed at different temperatures. RMS=1.55 nm, 3.02 nm, 1.89 nm, 1.08 nm, respectively.

3.2.4 OPVs performance based-on PDEHBTA

Table 3.2 shows the influence of different D:A ratios and solvent on power conversion efficiency, and the highest PCE based-on PDEHBTA: PCBM corresponded to the D:A of 1:1 by using dichlorobenzene as solvent. The current density–voltage (J-V) curves of the devices are shown in **Figure 3.9**. The highest PCE among these devices showed as 1.58 % with a corresponding short circuit current density (J_{SC}) of 3.72 mA cm^{-2}, a V_{OC} of 0.94 V and a FF of 0.45. Obviously, the PDEHBTA: PCBM device has a higher V_{OC} compared with PDDBTA: PCBM one and is approximately equal to the theoretical value by using the method described in **Section 2.5.1**, which indicates little energy loss for PDEHBTA: PCBM OPVs. However, the maximum hole SCLC mobilities of the PDEHBTA :PCBM blend film was low to 1.24×10^{-7} cm^2 V^{-1} s^{-1} even 1 order of magnitude lower than that of PDDBTA blend films. The corresponding electron SCLC mobility was up to 9.43×10^{-7} cm^2 V^{-1} s^{-1} which had a large difference with hole SCLC mobility led to a lower J_{SC} and FF. Furthermore, the lower J_{SC} and FF should be caused

by the low molecular weight. Schilinsky's group demonstrated that P3HT fractions with high molecular weight (13.8 kD in dichloromethane and 19 kD in chloroform) showed 3-4 times of J_{SC} and approximately 2 times of FF compared with those of low molecular weight fractions, respectively (2.2 kD in ethyl acetate and 5.6 kD in hexane). High molecular weight fraction of P3HT as well as high regioregularity supports the formation of a lamellar structure, which is a safe indication of higher mobility due to the expansion of the crystallinity area.[105]
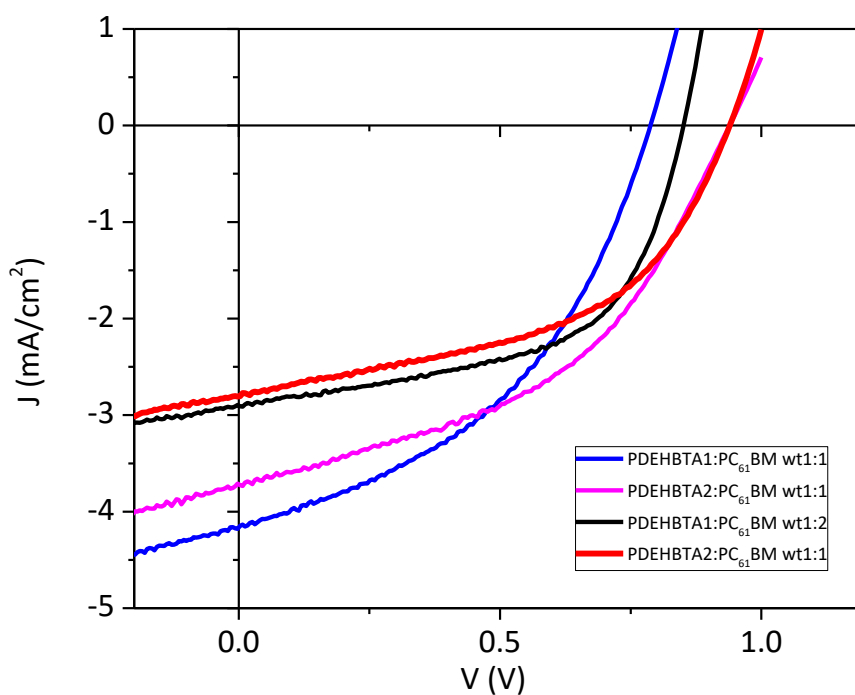
Figure 3.9 J-V curves for OSC devices based-on PDEHBTA1 and PDEHBTA2.

Table 3.2 OPV performances of OSC devices based on the blend of PDEHBTA1: PC$_{61}$BM and PDEHBTA2: PC$_{61}$BM, respectively.

Sample	solvent	Weight ratio	Jsc (mA cm^{-2})	Voc (V)	FF	PCE (%)
PDEHBTA2: PC$_{61}$BM	CB		Poor film, no performance			
PDEHBTA1:PC$_{61}$BM	DCB	1:1	-4.16	0.79	0.44	1.43
PDEHBTA1: PC$_{61}$BM	DCB	1:2	-2.90	0.85	0.56	1.39
PDEHBTA2: PC$_{61}$BM	**DCB**	**1:1**	**-3.72**	**0.94**	**0.45**	**1.58**
PDEHBTA2: PC$_{61}$BM	DCB	1:2	-2.81	0.94	0.49	1.29
PDDBTA: PC$_{61}$BM	**DCB**	**1:2**	**-4.70**	**0.73**	**0.64**	**2.18**

3.3 Synthesis and characterization of poly(1H-hexylpyrrole-azine) (PHPA)

3.3.1 Synthesis of PHPA
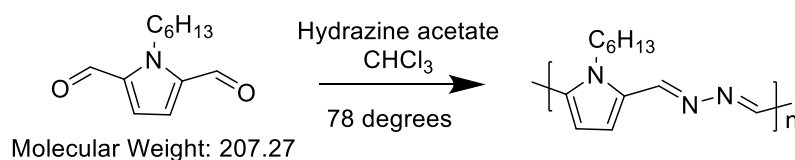
Scheme 3.4 Synthesis of poly(1H-hexylpyrrole-azine) (PHPA)

N-(n-hexyl)-2,5-dialdehydepyrrole (423 mg, 2.04 mmol) was added into a 25 ml 2-neck round bottom flask, then refilled by argon three times. Hydrazine acetate (188 mg,2.04 mmol) was added into flask followed by 4 ml chloroform. The solution was heated to 80 degrees centigrade gradually and stirred for 24h. After cooling to room temperature, the mixture was precipitated in 150 ml methanol and then filtered to give red solid, followed by Soxhlet extraction with acetone, hexane, heptane and chloroform. The chloroform fraction was poured into methanol and then were filtered and dried to afford

a red solid. Yield: 257 mg (61.6%)

M_w = 7.0 kD; M_n = 2.0 kD; **PD** = 3.43 (low temperature GPC)

3.3.2 Characterization of PHPA

The onset of oxidation curve started at a potential of 0.66 V, and a HOMO level of -5.46 eV can be estimated by the CV curve (**Figure 3.10**). There was no reduction peak for this polymer and the LUMO level was estimated from the HOMO level and the optical band gap from UV-vis spectra (**Figure 3.11**) to be -3.37 eV.
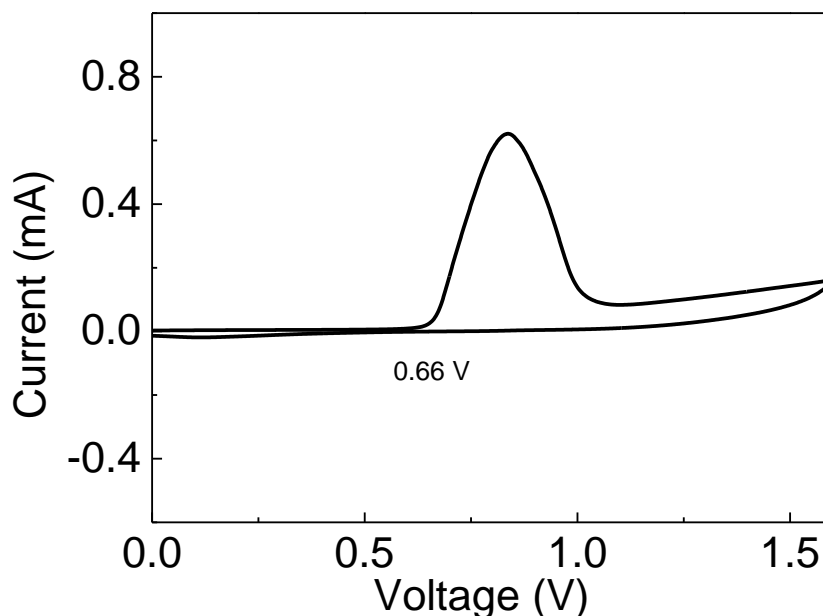
Figure 3.10 Cyclic voltammograms of PHPA film measured in tetrabutylammonium fluoride (0.1 M) solution in acetonitrile using Ag/AgCl as the reference electrode.

The wavelength of maximum absorbance for PDEHBTA2 in a CHCl₃ solution was 509 nm as shown in **Figure 3.12**, while an obvious red-shift with a maximum absorbance at 517.4 nm was observed along with a shoulder peak at 556.1 nm (**Figure 3.11**). After annealed at 150 °C for 20 min, the maximum peak bule-shifted to 509.6 nm. A more significant shoulder peak appeared at 549.7nm compared with the maximum peak, but

the intensities of both two peaks decreased probably due to the partially decomposition of this polymer after being heated.
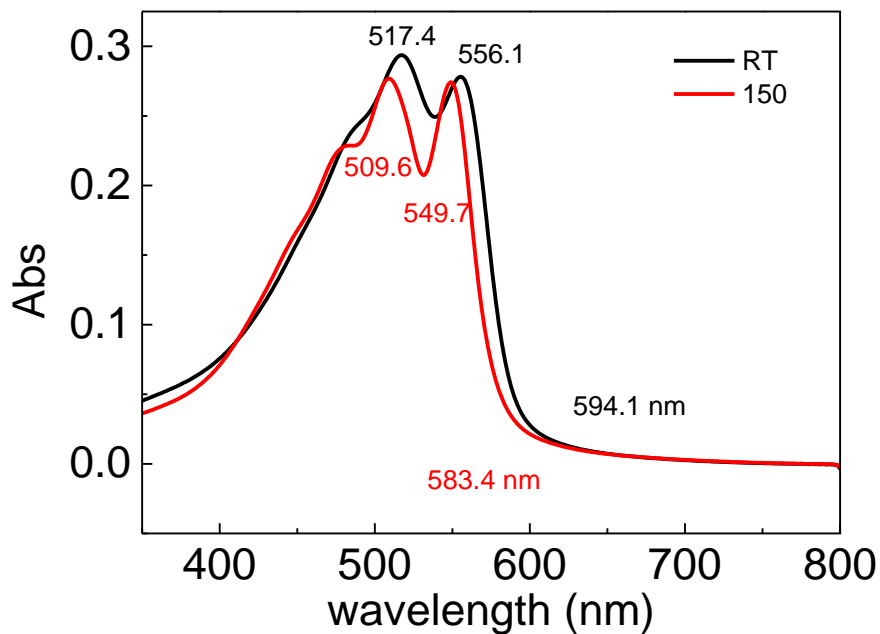
Figure 3.11 UV-vis absorption spectra of PHPA films at room temperature and annealing to 150°C.

The weight of PHPA remains 99.4% at 290°C as shown in TGA **Figure 3.13**.
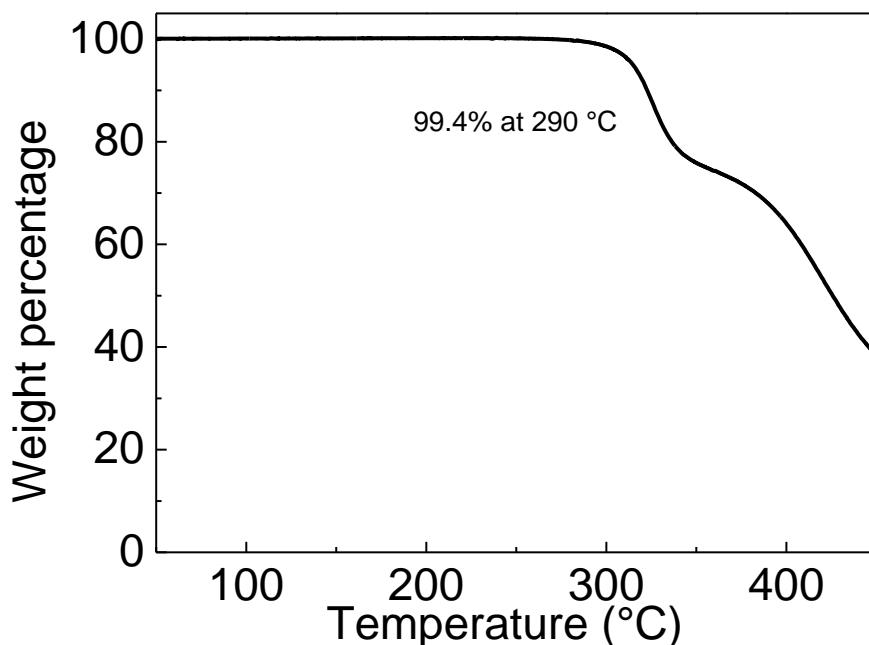
Figure 3.13 The TGA curve of PHPA obtained at a heating rate of 10 °C min^{-1} under nitrogen.

DSC results for PHPA was plot in Figure 3.14. During the first heating scan (**Figure 3.14** from -20 °C to 200 °C), a glass transition temperature T_g was observed at 41.6 °C, followed by a melting point at 109.1°C and a corresponding one at 99.7 °C during the first cooling process. After increasing the heating temperature to 240 °C (**Figure 3.14** - 20 °C to 240 °C), there was another absorption peak at 209.6°C and a releasing peak at 219.8 °C, which indicated the melting point of backbone. Therefore, the peak at 99.7 °C during first and second cycles corresponded to melting point for side chain, which explained in **Section 2.3.6.**
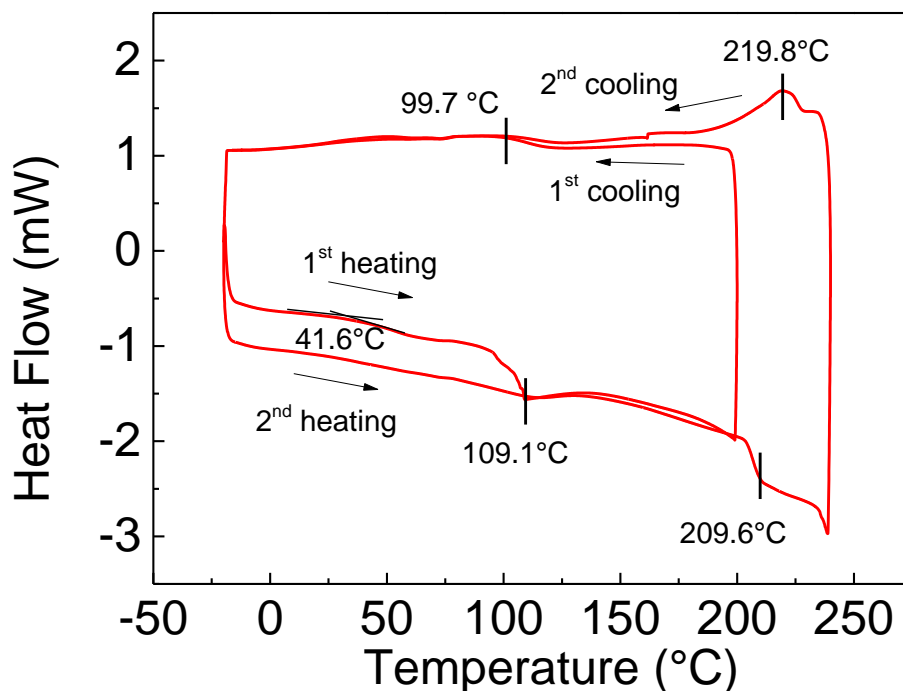
Figure 3.14 DSC diagrams of PHPA measured at a heating rate of 5 °C min^{-1} under nitrogen.

3.3.3 OTFTs performance based-on PHPA

As shown in **Table 3.3** and **Figure 3.15**, the highest hole mobility for PHPA OTFTs was 5.53 ×10^{-3} cm^2 V^{-1} s^{-1} which was tested under argon at room temperature, so the OPVs based-on PHPA should be fabricated without heating. Then the mobilities decreased gradually after annealed at 50 °C, 100 °C and 150 °C. According to the AFM images (**Figure 4.16**) and UV spectra (**Figure 4.11**), the crystallinity and roughness of thin films remain increasing accompanied by a partial decomposition of side chain, which may have an effect on charge transport.

Table 3.3 OTFT device parameters of PHPA at different annealing temperatures.

Polymer	Annealing[a] temperature (°C)	Average (maximum) hole mobility[b] (cm^2 V^{-1} s^{-1})	V_{th}[c] (V)	I_{on}/I_{off}
PHPA	r. t. (22)	$5.3 \times 10^{-3} \pm 3 \times 10^{-4}$ (5.53×10^{-3})	-30	10^4
	50	$1.5 \times 10^{-3} \pm 3 \times 10^{-4}$ (1.67×10^{-3})	-26	10^4
	100	$1.2 \times 10^{-3} \pm 7 \times 10^{-5}$ (1.32×10^{-3})	-29	10^3
	150	$6 \times 10^{-4} \pm 1.6 \times 10^{-4}$ (7.8×10^{-4})	-28	10^3

[a] Each set of data were obtained from 3-4 OTFT devices.
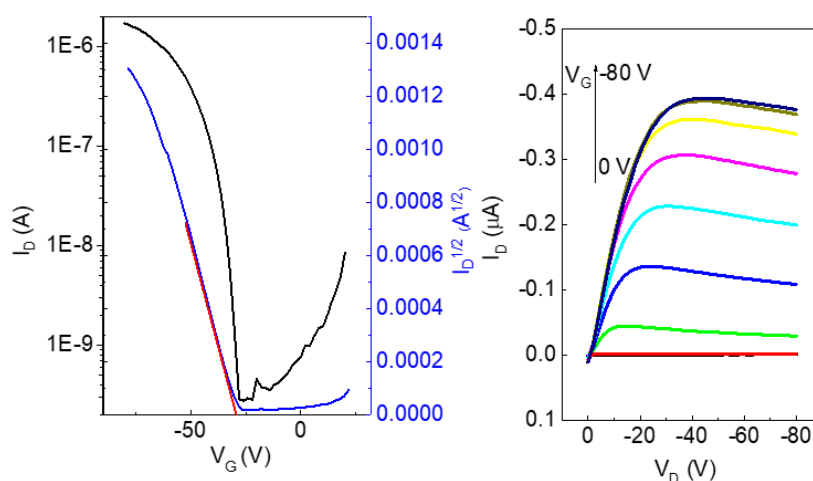
Figure 3.15 The transfer curves and output curves of OTFTs based on PHPA at room temperature. Device dimensions: channel length (L) = 30 µm; channel width (W) = 1000 µm. V_G varied from 0 V to -80 V in a step of -20 V in the output curves.
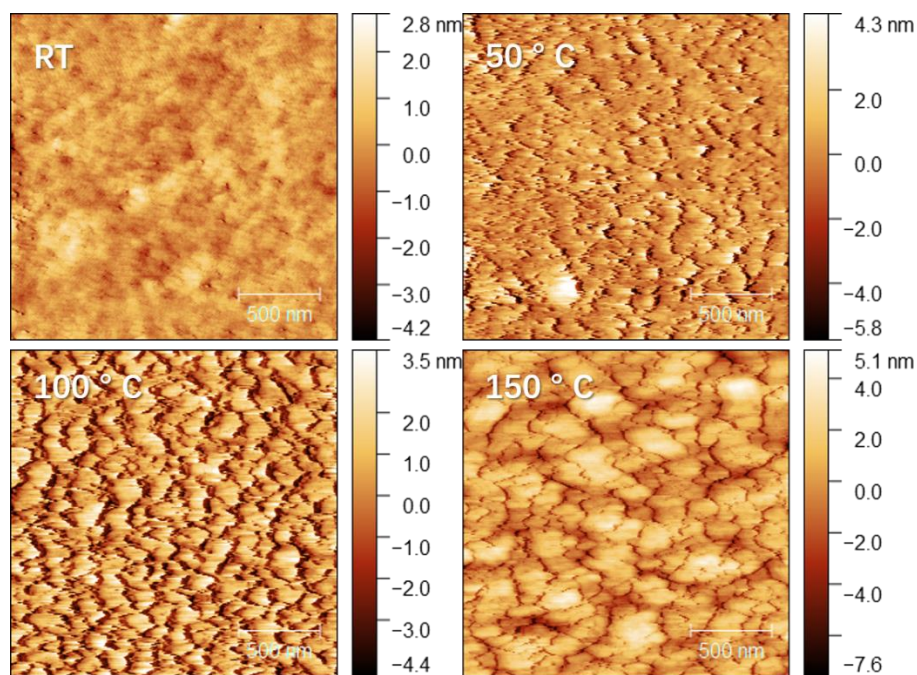
Figure 3.16 AFM height images of neat PHPA films on SiO2/Si wafers annealed at different temperatures. RMS=0.51 nm, 1.431 nm, 1.608 nm, 1.613 nm, respectively.

3.3.4 OPVs performance based-on PHPA

The current density–voltage (J-V) curves of the device with best PCE (**Figure 3.17**) showed as 1.1 % with a corresponding J_{SC} of 4.04 mA cm^{-2}, a V_{OC} of 0.7 V, and a FF of 0.39. The PHPA: PCBM device has a higher HOMO level (-5.46 eV) compared with PDDBTA and PDEHBTA, and the theoretically calculated V_{OC} should be 0.86 V which was higher than the real one, indicating energy loss caused by poor morphology because of the relatively low molecular weight. What's more, the FF of the PHPA: PCBM device is also much lower than that of the PDDBTA: PCBM device, which should be caused by the low molecular weight. In fact, the solubility of PHPA in chloroform or chlorobenzene was acceptable, and what limited the polymerization degree should be the short straight side chain, which means PHPA had already reached the maximum solubility in chloroform by using condensation method reacted with hydrazine acetate. The hole and electron SCLC mobilities of PHPA:PCBM blend film were 1.8×10^{-7} cm^2 V^{-1} s^{-1} and 1.14×10^{-6} cm^2 V^{-1} s^{-1}. Overall, the low FF and J_{SC} still need to be improved

by increasing the molecular weight of this series of donor polymer.

J_{SC}= -4.04 mA cm^{-2}

V_{OC}= 0.7 V

FF= 0.39

PCE= 1.1%

PHPA:PC$_{61}$BM wt1:1
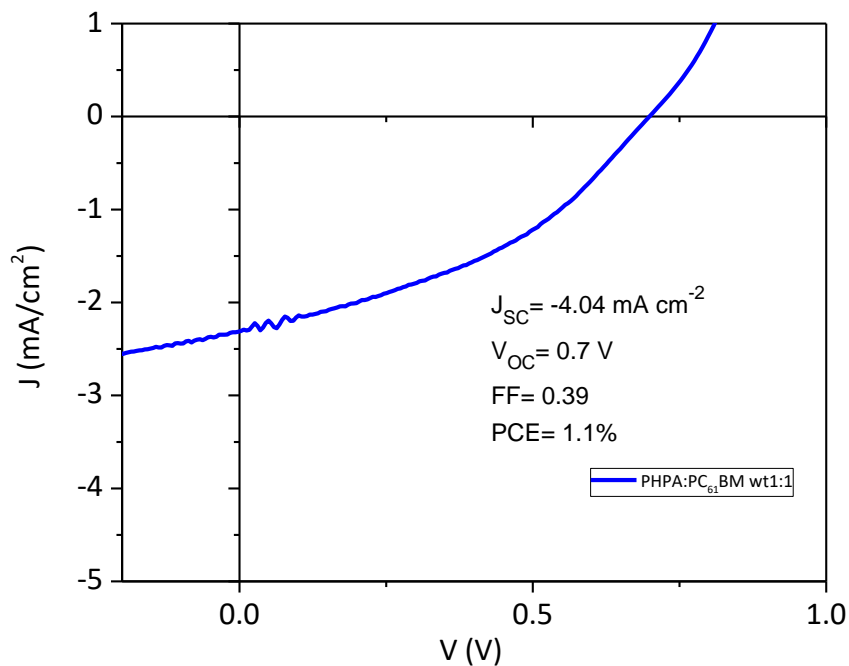
Figure 3.17 J-V curves for OSC devices based-on PHPA.

3.4 Conclusion and future directions

In order to improve poor morphology of PDDBTA: PCBM active layer thin film, two optimized structure modified from PDDBTA were designed and synthesized, which were a branch side chain polymer PDEHBTA and a pyrrole-azine backbone polymer PHPA. PDEHBTA showed a hole mobility up to 3.4 $\times 10^{-3}$ cm^2 V^{-1} s^{-1} and a 1.58% of highest PCE in PDEHBTA: PCBM OSCs, while the hole mobility for PHPA was 5.53 $\times 10^{-3}$ cm^2 V^{-1} s^{-1} at room temperature and the best PCE for OPVs based on PHPA: PCBM was 1.1%.The solubility of PDDBTA and PHPA became better dissolved in CHCl$_3$, but the low J_{SC} and FF of these two polymers were still the main reasons for limiting power conversion efficiencies due to the relative low molecular weight, which led to unsatisfactory active layer film morphology.

For future directions, the challenge should be increasing the molecular weight of PDEHBTA and PHPA. As shown in Scheme **3.5**, to avoid the steric problems of branch side chain during PDEHBTA condensation and increase the predicted molecular weight, another method is oxidative polymerization reacted with the monomer itself which contains an azine group between two thiophene rings. PHPA I synthesized reached the maximum solubility in chloroform which restricted the backbone chain growth, so a branch side chain pyrrole-azine polymer might be a better choice (**Scheme 3.6).**

(1*E*,2*E*)-1,2-bis((3-(2-ethylhexyl)thiophen-2-yl)methylene)hydrazine
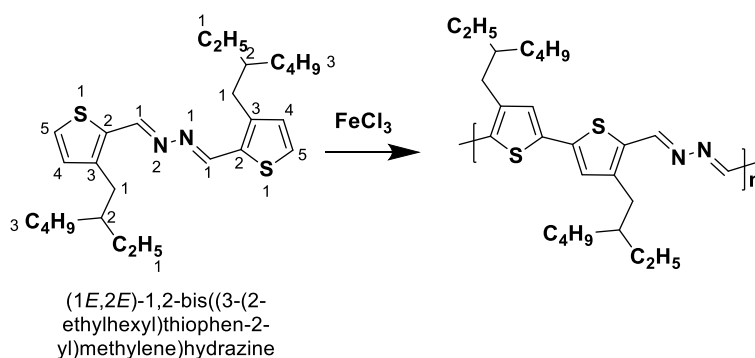
Scheme 3.5 Oxidative polymerization design for PDEHBTA
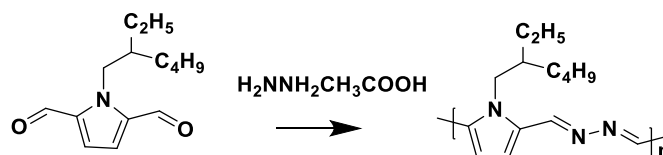
Scheme 3.6 Optimization design for PHPA

3.5 Experimental section

3.5.1 Synthesis and characterization of 3-(2-ethylhexyl)thiophene

Molecular Weight: 163.03

Molecular Weight: 196.35
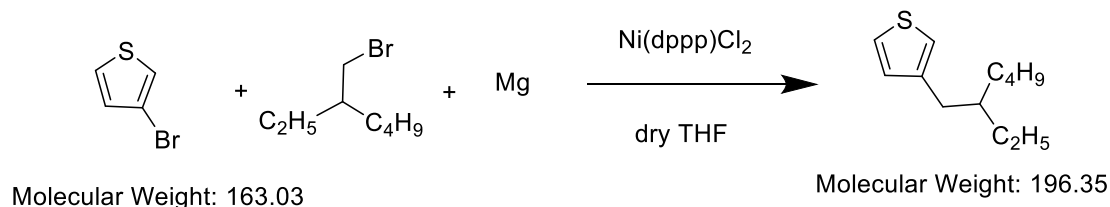
Scheme 3.7 Synthesis of 3-(2-ethylhexyl)thiophene.

A solution of 2-ethylhexyl bromide (5 ml, 28 mmol) in anhydrous THF (15 mL) was added magnesium turnings (2g, 82.2 mmol) with anhydrous THF (5 mL) at a rate sufficient to maintain gentle reflux under N_2. Then the solution was refluxed for 4 h and was cooled to rt followed by transferred dropwise via syringe into a flask containing a solution of 3-bromothiophene (2.4 ml, 25.6 mmol) and dichloro(1,3-bis(diphenylphosphino)propane) nickel (0.139 g, 0.256 mmol) in anhydrous THF (20 mL) under N_2. The mixture was stirred at reflux temperature overnight. After cooling to room temperature, the reaction was quenched with water and extracted with dichloromethane. The combined organic phase was washed with brine and water then dried with anhydrous Na_2SO_4 and concentrated to a yellow oil. The crude product was purified by distillation (under low vacuum at 102 °C) and eluted with hexane through a short column, then a colorless oil was gained (3.2 g, yield 64%), around 1 g mixture left after distillation. (300 MHz, CDCl$_3$, ppm) δ: 7.22-2.19 (dd, 1H), 6.90-6.87 (m, 2H), 2.56-2.54 (d, 2H), 1.54-1.50 (t, 1H), 1.32-1.15 (m, 8H), 0.91-0.8 (m, 6H).

3-(2-ethylhexyl)thiophene before column

72
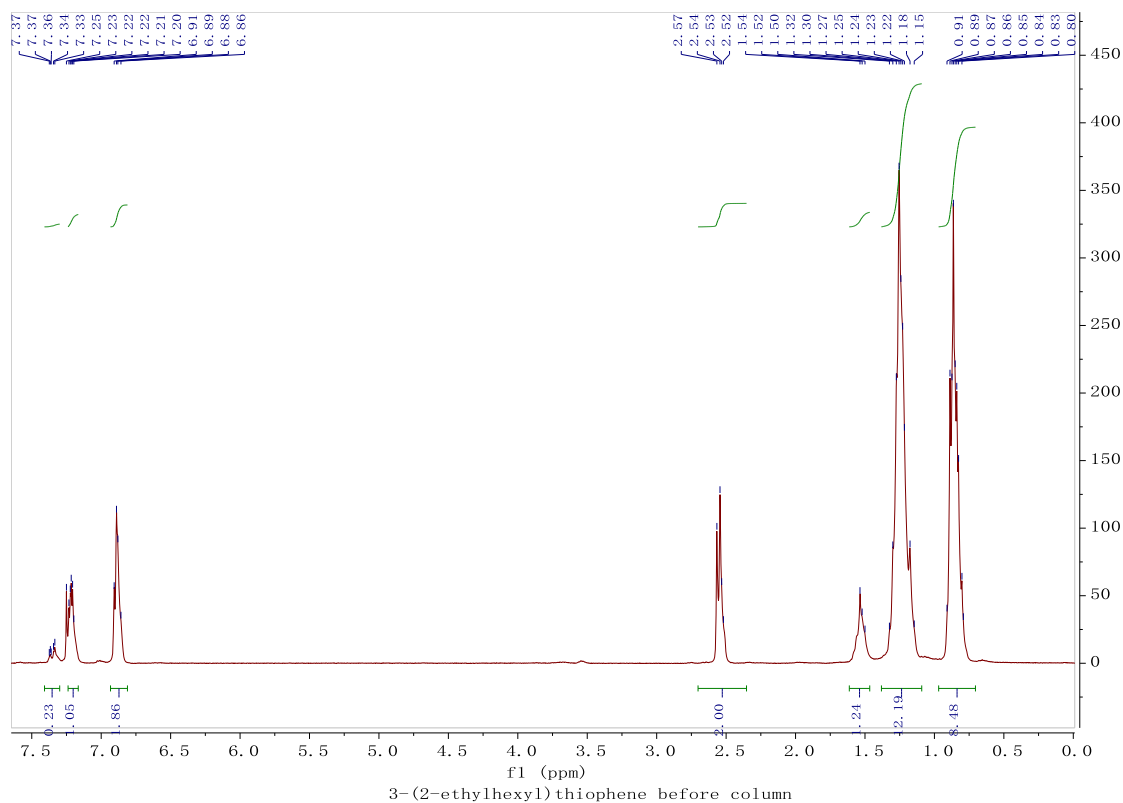
Figure 3.18 300 MHz ^{1}H NMR spectrum for 3-(2-ethylhexyl)-thiophene before eluted by column in Chloroform-*d*.

3-(2-ethylhexyl)thiophene
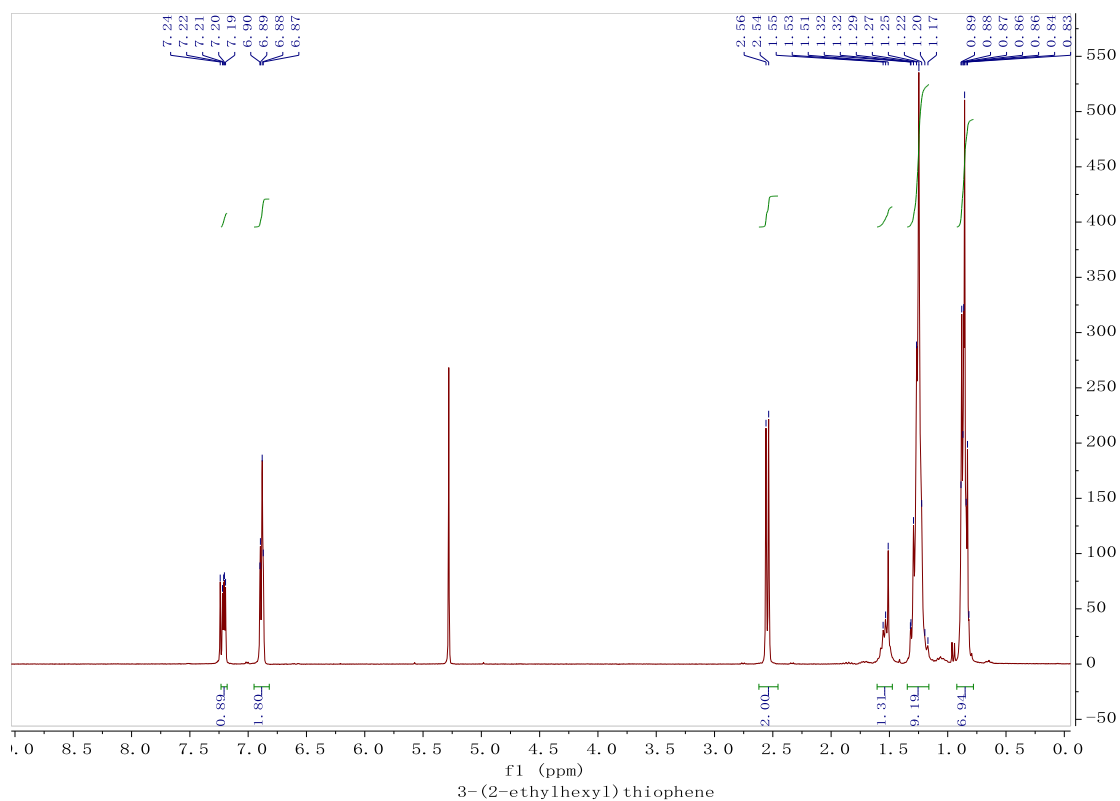
Figure 3.19 300 MHz ^{1}H NMR spectrum for 3-(2-ethylhexyl)thiophene after eluted by column in Chloroform-*d*.

3.5.2 Synthesis of 4,4'-di(2-ethylhexyl)-2,2'-bithiophene

Molecular Weight: 196.35   Molecular Weight: 390.69
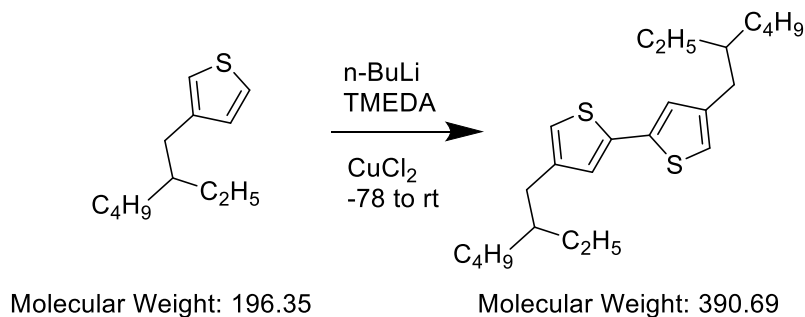
Scheme 3.8 Synthesis of 4,4'-di(2-ethylhexyl)-2,2'-bithiophene.

TMEDA (2.65 ml, 18 mmol) was added into a three-neck flask with 10 ml dry ether after removed air and refilled N_2 three times. Then n-Buli solution (2.5M in hexane) (6.63 ml, 16.5 mmol) was added to the solution dropwise at -78 °C and stirred for half an hour. After warmed to room temperature, the complex solution was transferred into a drop funnel by syringe which was connected with another three-neck round bottom flask followed by refilled N_2 three times and added 3-(2-ethylhexyl)thiophene and 30 ml ether. The complex solution was added into starting material, heated up to 40 °C and refluxed 1.5 h, then cooled down to -78°C. Slowly warmed up to room temperature and stirred overnight. Added 4ml conc. HCL and extracted with ether, washed with NH_4Cl and water, dried by anhydrous Na_2SO_4. Removed organic solvent by rotary evaporator. Purify the crude product by distillation to remove starting material which was not reacted and by column with hexane as eluent. Yield 55% (1.65 g), purity 92%. (300 MHz, CDCl$_3$, ppm) δ: 6.93 (s, 2H), 6.73 (s, 2H), 2.50-2.47 (d, 4H), 1.56-1.52 (t, 2H), 1.32-1.17 (m, 16H), 0.89-0.79 (m, 12H).

4,4'-(2-ethylhexyl)-2,2'-bithiophene

3.5.3 Synthesis of 4,4'-di(2-ethylhexyl)-2,2'-bithiophene-5,5'dicarboxaldehyde

Scheme 3.9 Synthesis of 4,4'-di(2-ethylhexyl)-2,2'-bithiophene-5,5'dicarboxaldehyde.

THF (25 ml) and 4,4'-di(3-ethylhexyl) -2,2'-bithiophene (1.6g, 4.10 mmol) was added into a 2-neck round bottom flask after refilled by N_2 three times (orange). TMEDA (1.53 ml, 10.13 mmol)was added dropwise at -78 °C and stirred for 25 min (green), then n-BuLi (2.5 M in hexane) (4.07 ml, 10.13 mmol) was dropped into the mixture and stirred for 30 min. Warmed up to RT and stirred for 2h then cooled down to -78 °C. Added DMF (1.3 ml, 17.07 mmol)in one portion and slowly warm up to RT and stirred overnight. Added conc. HCL and water, extracted with diethyl ether and washed with NH_4Cl solution and water, dried over anhydrous Na_2SO_4, removed solvent by rotary evaporator. The crude product was purified through silica gel column (hexane: dichloromethane= 1:5(v: v)) and recrystallized with ethyl acetate, and yellow powder was obtained. Yield: 48%, 0.88g. (300 MHz, CDCl$_3$, ppm) δ: 9.99 (s, 2H), 7.14 (s, 2H), 2.85-2.83 (d, 4H), 1.54-1.34 (t, 2H), 1.33-1.24 (m, 16H), 0.91-0.84 (m, 12H).
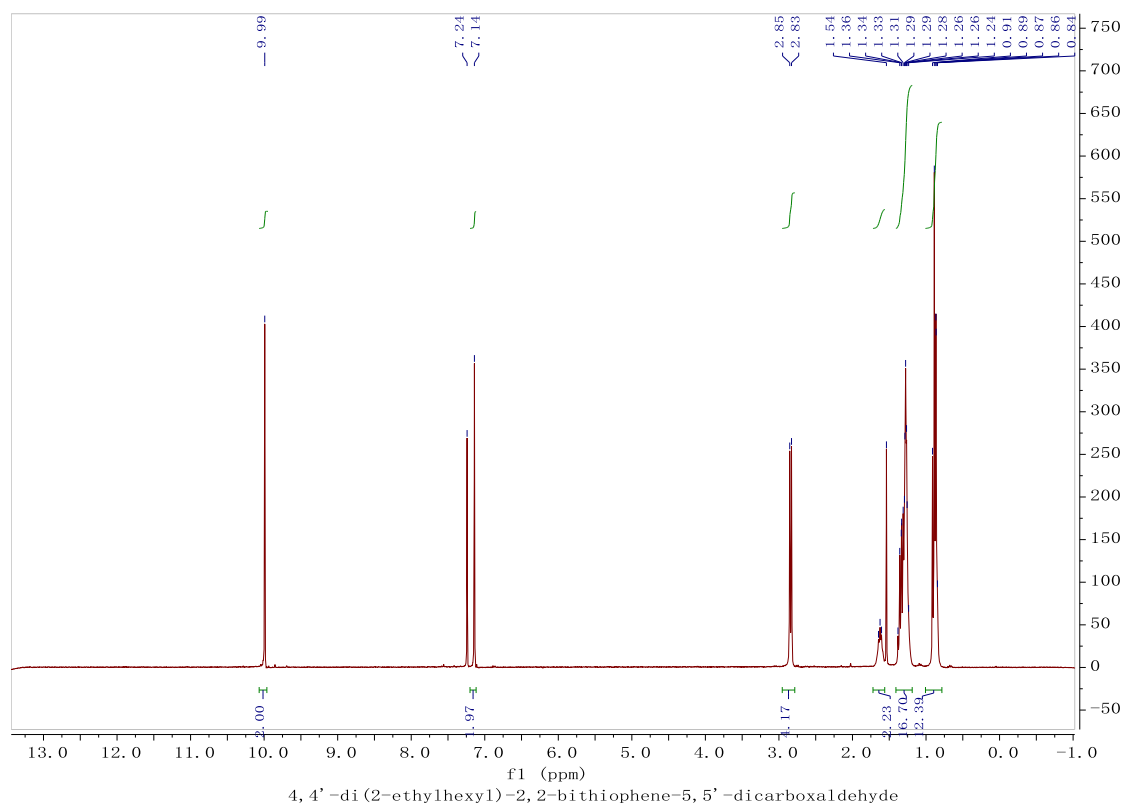
Figure 3.21 300 MHz ^{1}H NMR spectrum for 4,4'-di(2-ethylhexyl)-2,2'-bithiophene-5,5'dicarboxaldehyde in Chloroform-*d*.

3.5.4 Synthesis of 1-Hexyl-1H-pyrrole
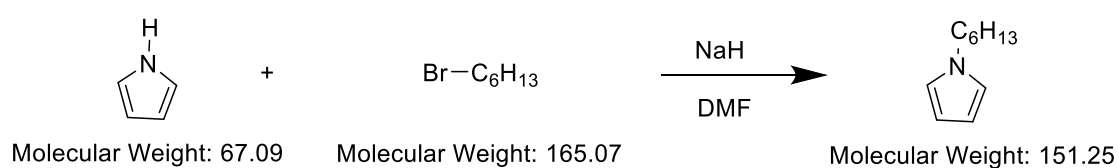
Scheme 3.10 Synthesis of 1-Hexy-1H-pyrrole

Sodium hydride (60% in mineral oil) (3.3g, 82.3 mmol) was stirred in DMF (150 ml) at 0 °C, then pyrrole (3 ml, 43.3 mmol) was added dropwise into flask slowly. After hydrogen evolution had ceased, 1-bromohexane (8.9 ml, 63 mmol) was added in one portion. The solution was warmed up to room temperature and stirred overnight, then quenched by water and extracted with DCM and washed with water and brine. The brown crude product was purified by column with hexane and then Claisen distillation

(56 °C, 0.18 mmHg). 1-Hexy-1H-pyrrole was shown as colorless oil with a yield of 79.6%. (300 MHz, CDCl₃, ppm) δ: 6.63 (t, 2H), 6.12 (t, 2H), 3.85 (t, 2H), 1.75 (quintet, 2H), 1.25-1.29 (m, 8H), 0.88 (t, 3H).
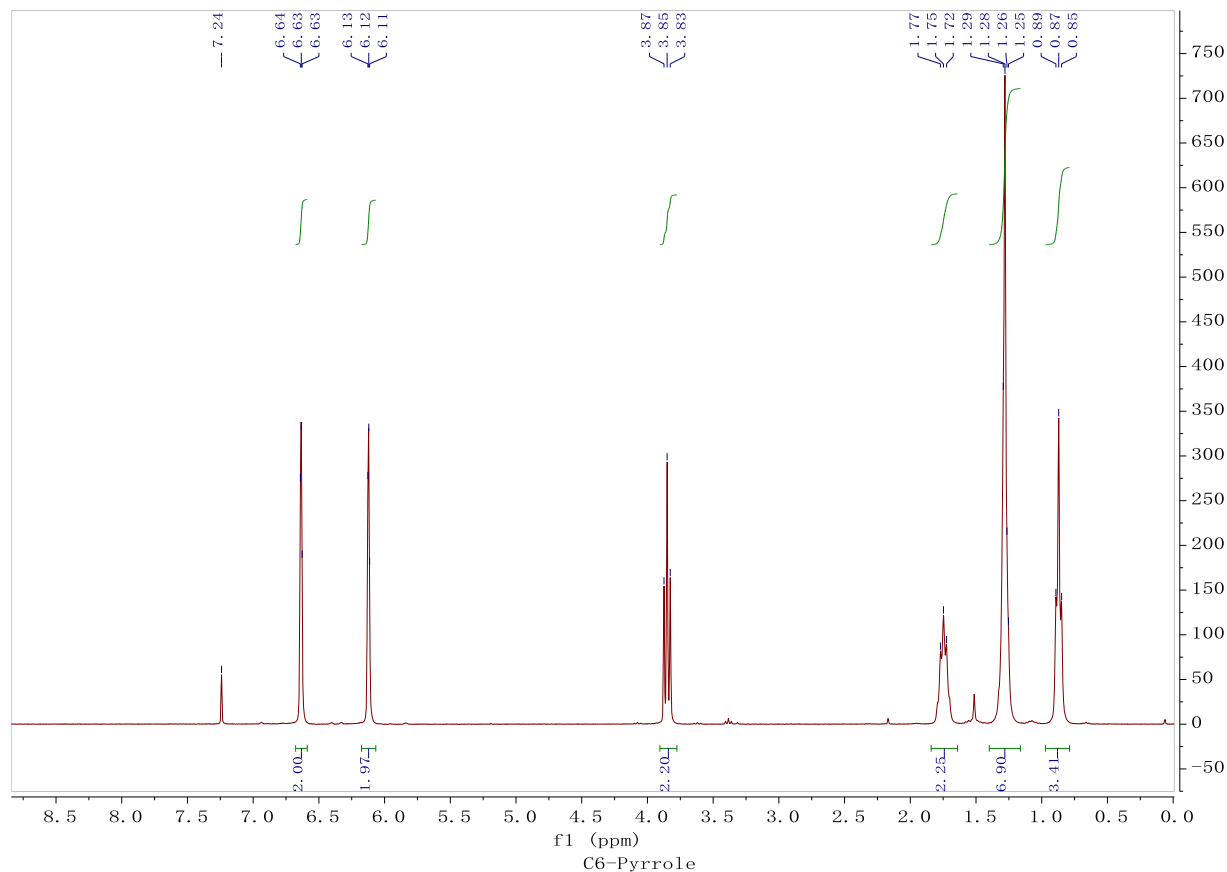
Figure 3.22 300 MHz ^{1}H NMR spectrum for 1-Hexy-1H-pyrrole in Chloroform-*d*.

3.5.5 Synthesis of N-(n-hexyl)-2,5-dibromopyrrole
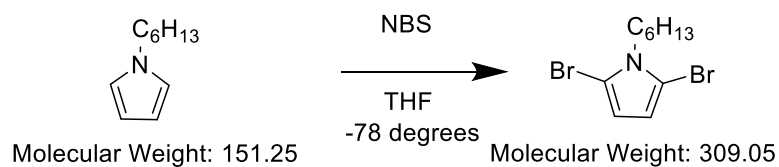
Scheme 3.11 Synthesis of N-(n-hexyl)-2,5-dibromopyrrole

To a 100-mL two-neck round-bottom flask 1-Hexy-1H-pyrrole (3g, 19.8 mmol) and

anhydrous THF (50 ml) were added. Then the flask was cooled to -78° C and NBS powder (8.89g, 50 mmol) was added. The mixture was stirred for 10 minutes, then warmed to RT, and stirred for another 1 h. followed by diluted with 40 mL of water, extracted with 100 mL hexane, and dried by MgSO4 powder. Hexane was removed by vacuum rotary evaporator to afford crude product. The target material was purified by column with hexane to give orange oil. (5.9 g, yield 96%). (300 MHz, CDCl$_3$, ppm) δ: 6.14 (d, 2H), 3.93 (t, 2H), 1.66 (quintet, 2H), 1.24-1.35 (m, 8H), 0.88 (3H).
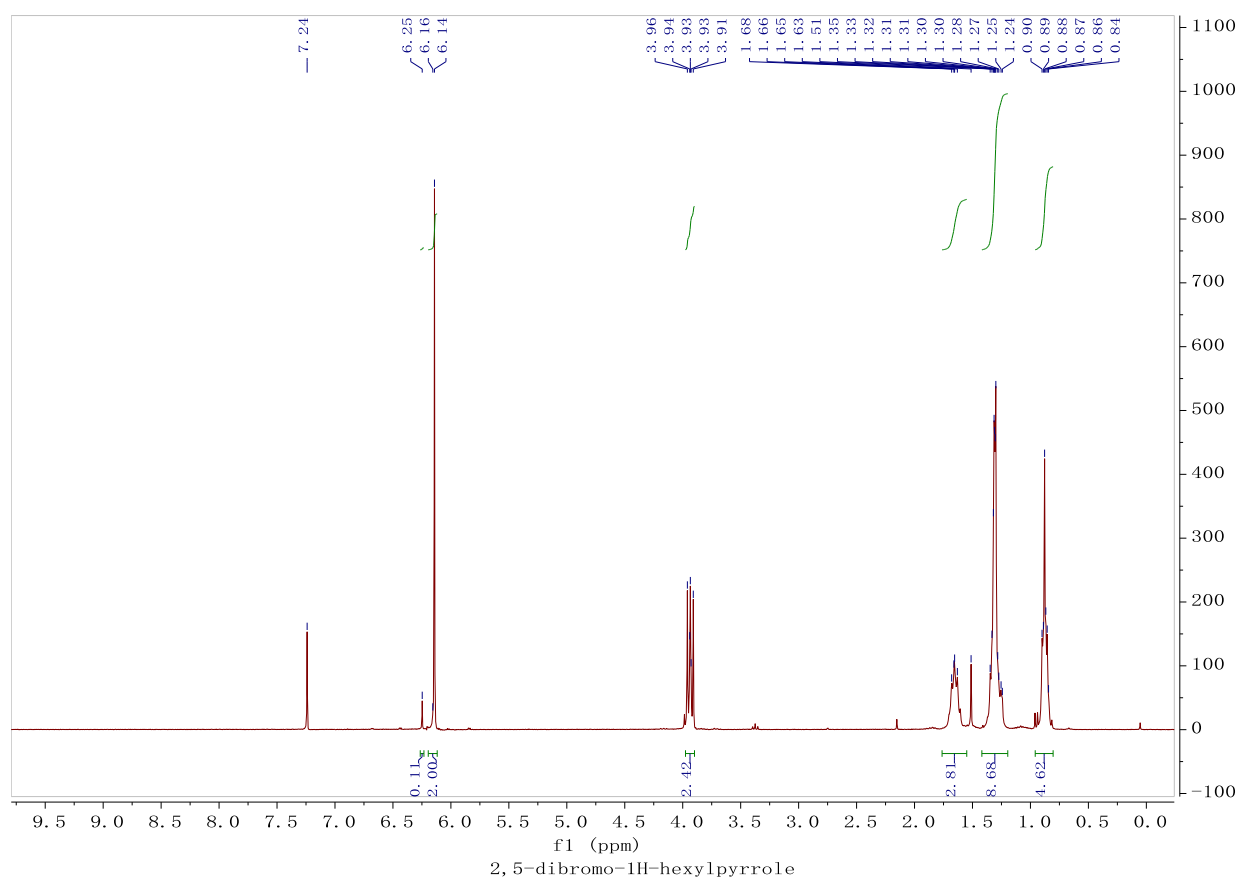
Figure 3.23 300 MHz ^{1}H NMR spectrum for N-(n-hexyl)-2,5-dibromopyrrole in Chloroform-d.

3.5.6 Synthesis of N-(n-hexyl)-2,5-dialdehydepyrrole
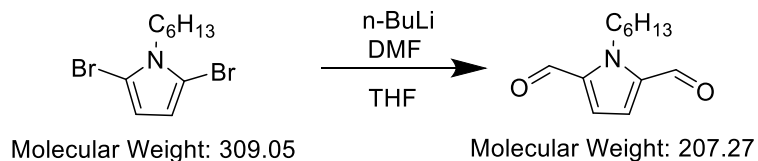
Scheme 3.12 Synthesis of N-(n-hexyl)-2,5-dialdehydepyrrole

To a 50-mL two-neck round-bottom flask 2,5-dibromo-1H-hexylpyrrole (5 g, 16.2 mmol) and anhydrous THF (50 ml) were added. The mixture was cooled to -78°C. N-BuLi (16.2 ml, 16.2 mmol) was added drop-wise into the mixture. 30 minutes later, DMF (3.87 ml, 50 ml) was added. The mixture was stirred for 50 more minutes and poured into the separation funnel containing pure hexane and water for extraction, followed by dried with Na_2SO_4 and filtered. The crude product was purified by column chromatography with silica gel and DCM /hexane (1/1) to give pure liquid product. (0.64 g, Yield 19%) (300 MHz, $CDCl_3$, ppm) δ: 9.81 (s, 2H), 6.93 (s, 2H), 4.72 (t, 2H), 1.69 (quintet, 2H), 1.24-1.33 (m, 8H), 0.85 (t, 3H).
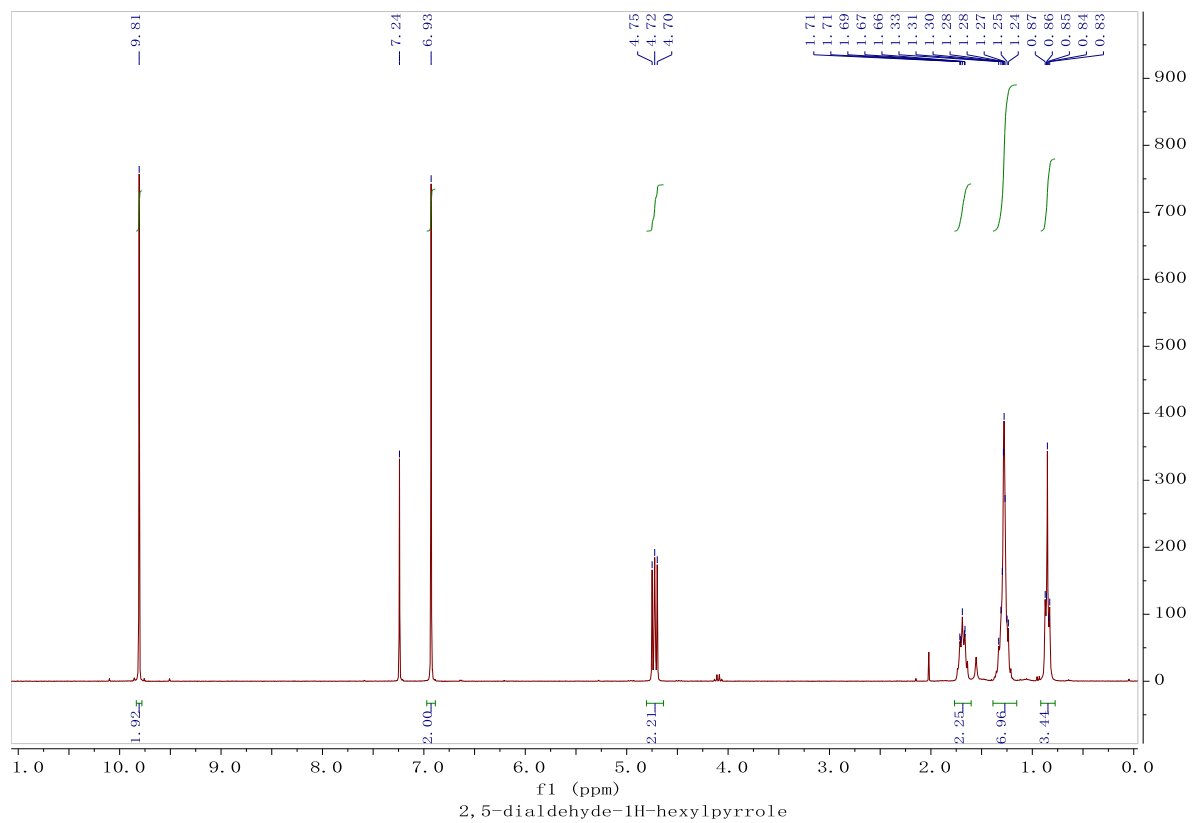
Figure 3.24 300 MHz ^{1}H NMR spectrum for N-(n-hexyl)-2,5-dialdehydepyrrole in Chloroform-*d*.

Chapter 4 Summery and future works

In conclusion, a new azine-based donor polymer PDDBTA was successfully synthesized in only three steps starting from 3-dodecylthiophene. The polymer showed good properties in organic thin film transistors and organic solar cells as a donor material, which reached the same degree compared with those based on P3HT electronic devices. The target of this project was practically achieved that a lower HOMO level of PDDBTA compared with that of rr-P3HT was demonstrated which resulted in a higher V_{OC} of PDDBTA: $PC_{61}BM$ OPVs. Then two kinds of optimization work were also presented in this thesis, though PDEHBTA and PHPA still need further improvement.

In chapter 2, the synthesis procedure of PDDBTA was recorded. Various characterizations for PDDBTA indicated good properties including: a lower HOMO level compared with P3HT which was suitable to match with PCBM as an active layer; a good optical performance and a satisfactory thermal stability. The polymer PDDBTA showed good hole mobility of up to 4.1×10^{-2} cm^2 V^{-1} s^{-1} in OTFTs. Moreover, the V_{OC} of PDDBTA based OPVs obviously increased and the highest PCE based on this polymer as a donor in OPVs achieved up to 2.18%, which was the first case to fabricate OSCs by using an azine-based semiconductor polymer. These results indicated that this series of azine-based polymer may be a class of low-cost polymer semiconductors suitable for large-scale production of organic solar cells and other printed electronic products. However, the solubility of PDDBTA led a poor morphology in PDDBTA: PCBM blend films, which had a bad effect on SCLC mobilities thereby influenced the J_{SC} and FF and then restricted the OPV performance.

In Chapter 3, in order to improve the solubility and morphology drawbacks, a branch

side chain polymer PDEHBTA and a pyrrole-azine backbone polymer PHPA were synthesized based on PDDBTA. PDEHBTA showed hole mobility up to 3.4×10^{-3} cm^2 V^{-1} s^{-1} and a 1.58% of highest PCE when it was used as donor polymer combining with PCBM in OSCs. The best mobility for PHPA was tested as 5.53×10^{-3} cm^2 V^{-1} s^{-1} at room temperature and the best PCE for OPVs was 1.1%.Though the solubility of PDDBTA and PHPA changed better, the low J_{SC} and FF of these two polymers were still the direct reasons for limiting power conversion efficiencies because of the low molecular weight, which was different from that for PDDBTA.

For future works, the primary task is to increase the molecular weight of PDEHBTA and PHPA. For PDEHBTA, a new design scheme was shown as **Scheme 5.1**, and the azine group is added between two thiophene rings as a bithiophene-azine monomer which will be polymerized by oxidative polymerization to prevent the steric hindrance issue, thereby increase the molecular weight. For PHPA, since this polymer had already reached the maximum solubility in chloroform which hindered the growth of polymer chain, a branch side chain pyrrole-azine polymer might be a better choice as shown in **Scheme 5.2**
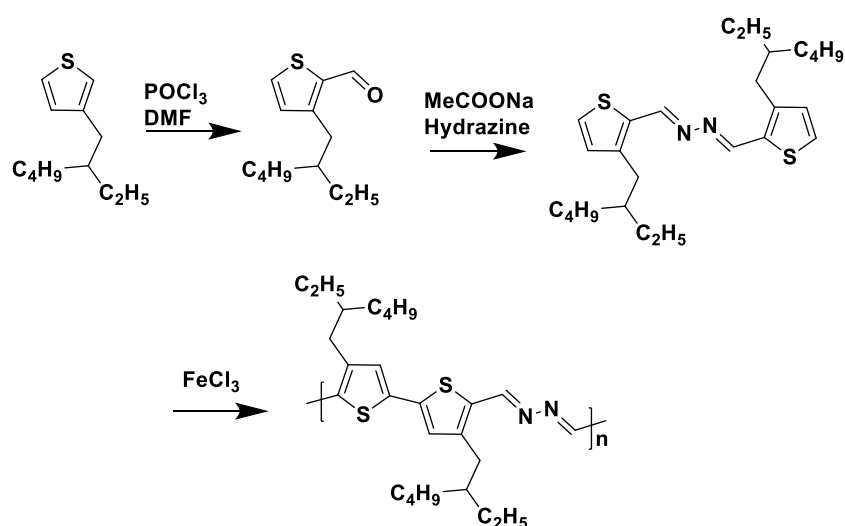
Scheme 4.1 Optimization for PDEHBTA**.**
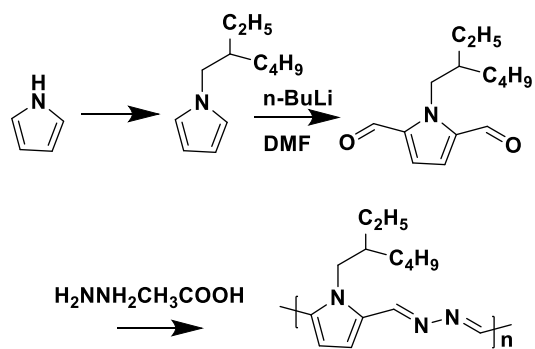
Scheme 4.2 Optimization design for PHPA.

Bibliography

[1]   N. Kannan and D. Vakeesan, "Solar energy for future world: - A review," *Renewable and Sustainable Energy Reviews*, vol. 62, pp. 1092–1105, Sep. 2016, doi: 10.1016/j.rser.2016.05.022.

[2]   Q. Tai and F. Yan, "Emerging Semitransparent Solar Cells: Materials and Device Design," *Advanced Materials*, vol. 29, no. 34, p. 1700192, 2017, doi: 10.1002/adma.201700192.

[3]   R. Memming, "Solar energy conversion by photoelectrochemical processes," *Electrochimica Acta*, vol. 25, no. 1, pp. 77–88, Jan. 1980, doi: 10.1016/0013-4686(80)80054-5.

[4]   "Photoelectrochemistry," *Science*, vol. 207, no. 4427, 1980, doi: 10.1126/science.207.4427.139.

[5]   W. A. Badawy, "Improvement of n-Si/SnO2/ electrolyte photoelectrochemical cells by Ru deposits," *Journal of Electroanalytical Chemistry and Interfacial Electrochemistry*, vol. 281, no. 1, pp. 85–95, Mar. 1990, doi: 10.1016/0022-0728(90)87031-E.

[6]   A. M. Bagher, M. M. A. Vahid, and M. Mohsen, "Types of Solar Cells and Application," *American Journal of Optics and Photonics*, vol. 3, no. 5, Art. no. 5, Aug. 2015, doi: 10.11648/j.ajop.20150305.17.

[7]   W. A. Badawy, "A review on solar cells from Si-single crystals to porous materials and quantum dots," *Journal of Advanced Research*, vol. 6, no. 2, pp. 123–132, Mar. 2015, doi: 10.1016/j.jare.2013.10.001.

[8]   "Total Energy Annual Data - U.S. Energy Information Administration (EIA)." https://www.eia.gov/totalenergy/data/annual/index.php (accessed Nov. 10, 2020).

[9]   J. Yan and B. R. Saunders, "Third-generation solar cells: A review and comparison of polymer:fullerene, hybrid polymer and perovskite solar cells," *RSC Advances*, vol. 4, no. 82, pp. 43286–43314, 2014, doi: 10.1039/c4ra07064j.

[10] H. Hoppe and N. S. Sariciftci, "Organic solar cells: An overview," *Journal of Materials Research*, vol. 19, no. 7, pp. 1924–1945, Jul. 2004, doi: 10.1557/JMR.2004.0252.

[11] Y. Liu *et al.*, "Spin-Coated Small Molecules for High Performance Solar Cells," *Advanced Energy Materials*, vol. 1, no. 5, pp. 771–775, 2011, doi: https://doi.org/10.1002/aenm.201100230.

[12] G. Dennler, M. C. Scharber, and C. J. Brabec, "Polymer-Fullerene Bulk-Heterojunction Solar Cells," *Advanced Materials*, vol. 21, no. 13, pp. 1323–1338, 2009, doi: https://doi.org/10.1002/adma.200801283.

[13] T. Kim *et al.*, "Flexible, highly efficient all-polymer solar cells," *Nature Communications*, vol. 6, no. 1, Art. no. 1, Oct. 2015, doi: 10.1038/ncomms9547.

[14] M. Hiramoto and Y. Shinmura, "Organic Solar Cells," in *Springer Handbook of Electronic and Photonic Materials*, S. Kasap and P. Capper, Eds. Cham: Springer International Publishing, 2017, pp. 1–1.

[15] B. Kippelen and J.-L. Brédas, "Organic photovoltaics," *Energy Environ. Sci.*, vol. 2, no. 3, pp. 251–261, Mar. 2009, doi: 10.1039/B812502N.

[16] A. M. Borchers, J. Duke, and G. Parsons, "Does willingness to pay for green energy differ by source?," *Energy Policy*, vol. 35, no. 6, pp. 3327–3334, 2007.

[17] R. B. Bergmann, "Crystalline Si thin-film solar cells: a review," *Appl Phys A*, vol. 69, no. 2, pp. 187–194, Aug. 1999, doi: 10.1007/s003390050989.

[18] S. E. Habas, H. A. S. Platt, M. F. A. M. van Hest, and D. S. Ginley, "Low-cost inorganic solar cells: from ink to printed device," *Chem Rev*, vol. 110, no. 11, pp. 6571–6594, Nov. 2010, doi: 10.1021/cr100191d.

[19] H. Kallmann and M. Pope, "Photovoltaic Effect in Organic Crystals," p. 3.

[20] C. W. Tang, "Two-layer organic photovoltaic cell," *Appl. Phys. Lett.*, vol. 48, no. 2, pp. 183–185, Jan. 1986, doi: 10.1063/1.96937.

[21] H. Kim *et al.*, "Organic solar cells based on conjugated polymers : History and recent advances," *Korean J. Chem. Eng.*, vol. 31, no. 7, pp. 1095–1104, Jul. 2014, doi: 10.1007/s11814-014-0154-8.

[22] N. S. Sariciftci, L. Smilowitz, A. J. Heeger, and F. Wudl, "Photoinduced Electron Transfer from a Conducting Polymer to Buckminsterfullerene," *Science*, vol. 258, no. 5087, pp. 1474–1476, Nov. 1992, doi: 10.1126/science.258.5087.1474.

[23] J. J. M. Halls *et al.*, "Efficient photodiodes from interpenetrating polymer networks," *Nature*, vol. 376, no. 6540, Art. no. 6540, Aug. 1995, doi: 10.1038/376498a0.

[24] G. Yu and A. J. Heeger, "Charge separation and photovoltaic conversion in polymer composites with internal donor/acceptor heterojunctions," *Journal of Applied Physics*, vol. 78, no. 7, pp. 4510–4515, Oct. 1995, doi: 10.1063/1.359792.

[25] G. Wang *et al.*, "Facile synthesis of a semiconducting bithiophene-azine polymer and its application for organic thin film transistors and organic photovoltaics," *RSC Advances*, vol. 10, no. 22, pp. 12876–12882, 2020, doi: 10.1039/D0RA01211D.

[26] L. Meng *et al.*, "Organic and solution-processed tandem solar cells with 17.3% efficiency," *Science*, vol. 361, no. 6407, pp. 1094–1098, Sep. 2018, doi: 10.1126/science.aat2612.

[27] Q. Liu *et al.*, "18% Efficiency organic solar cells," *Science Bulletin*, vol. 65, no. 4, pp. 272–275, Feb. 2020, doi: 10.1016/j.scib.2020.01.001.

[28] Y. Lin *et al.*, "17% Efficient Organic Solar Cells Based on Liquid Exfoliated WS2 as a Replacement for PEDOT:PSS," *Advanced Materials*, vol. 31, no. 46, p. 1902965, 2019, doi: 10.1002/adma.201902965.

[29] Y. Cui *et al.*, "17% efficiency organic photovoltaic cell with superior processability," *Natl Sci Rev*, doi: 10.1093/nsr/nwz200.

[30] T. Ameri, G. Dennler, C. Lungenschmied, and C. J. Brabec, "Organic tandem solar cells: A review," *Energy Environ. Sci.*, vol. 2, no. 4, pp. 347–363, Mar. 2009, doi: 10.1039/B817952B.

[31] "Organic Photovoltaics (OPV) Tutorial," *Sigma-Aldrich*. https://www.sigmaaldrich.com/materials-science/organic-electronics/opv-tutorial.html (accessed Nov. 14, 2020).

[32] S. R. Cowan, A. Roy, and A. J. Heeger, "Recombination in polymer-fullerene bulk heterojunction solar cells," *Phys. Rev. B*, vol. 82, no. 24, p. 245207, Dec. 2010, doi: 10.1103/PhysRevB.82.245207.

[33] M. C. Scharber *et al.*, "Design Rules for Donors in Bulk-Heterojunction Solar Cells—Towards 10 % Energy-Conversion Efficiency," *Adv. Mater.*, vol. 18, no. 6, pp. 789–794, Mar. 2006, doi: 10.1002/adma.200501717.

[34] N. K. Elumalai and A. Uddin, "Open circuit voltage of organic solar cells: an in-depth review," *Energy Environ. Sci.*, vol. 9, no. 2, pp. 391–410, 2016, doi: 10.1039/C5EE02871J.

[35] H.-Y. Chen *et al.*, "Polymer solar cells with enhanced open-circuit voltage and efficiency," *Nature Photonics*, vol. 3, no. 11, Art. no. 11, Nov. 2009, doi: 10.1038/nphoton.2009.192.

[36] M.-H. Jao, H.-C. Liao, and W.-F. Su, "Achieving a high fill factor for organic solar cells," *J. Mater. Chem. A*, vol. 4, no. 16, pp. 5784–5801, Apr. 2016, doi: 10.1039/C6TA00126B.

[37] R. S. Gurney, W. Li, Y. Yan, D. Liu, A. J. Pearson, and T. Wang, "Morphology and efficiency enhancements of PTB7-Th:ITIC nonfullerene organic solar cells processed via solvent vapor annealing," *Journal of Energy Chemistry*, vol. 37, pp. 148–156, Oct. 2019, doi: 10.1016/j.jechem.2018.12.015.

[38] Q. Wei, W. Liu, M. Leclerc, J. Yuan, H. Chen, and Y. Zou, "A-DA′D-A non-fullerene acceptors for high-performance organic solar cells," *Sci. China Chem.*, vol. 63, no. 10, pp. 1352–1366, Oct. 2020, doi: 10.1007/s11426-020-9799-4.

[39] K. He, P. Kumar, Y. Yuan, and Y. Li, "Wide bandgap polymer donors for high efficiency non-fullerene acceptor based organic solar cells," *Mater. Adv.*, Nov. 2020, doi: 10.1039/D0MA00790K.

[40] A. M. Bagher, "Introduction to Organic Solar Cells," *Sustainable Energy*, vol. 2, no. 3, Art. no. 3, Jan. 2014, doi: 10.12691/rse-2-3-2.

[41] R. Po, G. Bianchi, C. Carbonera, and A. Pellegrino, "'All That Glisters Is Not

Gold': An Analysis of the Synthetic Complexity of Efficient Polymer Donors for Polymer Solar Cells," *Macromolecules*, vol. 48, no. 3, pp. 453–461, Feb. 2015, doi: 10.1021/ma501894w.

[42] T. P. Osedach, T. L. Andrew, and V. Bulović, "Effect of synthetic accessibility on the commercial viability of organic photovoltaics," *Energy Environ. Sci.*, vol. 6, no. 3, pp. 711–718, Feb. 2013, doi: 10.1039/C3EE24138F.

[43] J. Min *et al.*, "Evaluation of Electron Donor Materials for Solution-Processed Organic Solar Cells via a Novel Figure of Merit," *Advanced Energy Materials*, vol. 7, no. 18, p. 1700465, 2017, doi: 10.1002/aenm.201700465.

[44] R. Po and J. Roncali, "Beyond efficiency: scalability of molecular donor materials for organic photovoltaics," *J. Mater. Chem. C*, vol. 4, no. 17, pp. 3677–3685, Apr. 2016, doi: 10.1039/C5TC03740A.

[45] C. Zhang *et al.*, "A top-down strategy identifying molecular phase stabilizers to overcome microstructure instabilities in organic solar cells," *Energy Environ. Sci.*, vol. 12, no. 3, pp. 1078–1087, Mar. 2019, doi: 10.1039/C8EE03780A.

[46] R. D. McCullough, R. D. Lowe, M. Jayaraman, and D. L. Anderson, "Design, synthesis, and control of conducting polymer architectures: structurally homogeneous poly(3-alkylthiophenes)," *J. Org. Chem.*, vol. 58, no. 4, pp. 904–912, Feb. 1993, doi: 10.1021/jo00056a024.

[47] R. S. Loewe, S. M. Khersonsky, and R. D. McCullough, "A Simple Method to Prepare Head-to-Tail Coupled, Regioregular Poly(3-alkylthiophenes) Using Grignard Metathesis," *Advanced Materials*, vol. 11, no. 3, pp. 250–253, 1999, doi: 10.1002/(SICI)1521-4095(199903)11:3<250::AID-ADMA250>3.0.CO;2-J.

[48] T.-A. Chen, X. Wu, and R. D. Rieke, "Regiocontrolled Synthesis of Poly(3-alkylthiophenes) Mediated by Rieke Zinc: Their Characterization and Solid-State Properties," *J. Am. Chem. Soc.*, vol. 117, no. 1, pp. 233–244, Jan. 1995, doi: 10.1021/ja00106a027.

[49] E. A. Zakhidov *et al.*, "Correlation of Degradation of P3HT:PCBM And P3HT:ITIC Organic Solar Cells with Changes of their Optical Spectra," *J Appl Spectrosc*, vol. 87, no. 3, pp. 464–470, Jul. 2020, doi: 10.1007/s10812-020-01024-z.

[50] Y. Qin *et al.*, "Highly Efficient Fullerene-Free Polymer Solar Cells Fabricated with Polythiophene Derivative," *Advanced Materials*, vol. 28, no. 42, pp. 9416–9422, 2016, doi: 10.1002/adma.201601803.

[51] X. Yang and A. Uddin, "Effect of thermal annealing on P3HT:PCBM bulk-heterojunction organic solar cells: A critical review," *Renewable and Sustainable Energy Reviews*, vol. 30, no. C, pp. 324–336, 2014.

[52] F. Padinger, R. S. Rittberger, and N. S. Sariciftci, "Effects of Postproduction Treatment on Plastic Solar Cells," *Advanced Functional Materials*, vol. 13, no. 1, pp. 85–88, 2003, doi: https://doi.org/10.1002/adfm.200390011.

[53] Y. Kim, S. A. Choulis, J. Nelson, D. D. C. Bradley, S. Cook, and J. R. Durrant, "Device annealing effect in organic solar cells with blends of regioregular poly(3-hexylthiophene) and soluble fullerene," *Appl. Phys. Lett.*, vol. 86, no. 6, p. 063502, Jan. 2005, doi: 10.1063/1.1861123.

[54] G. Li *et al.*, "High-efficiency solution processable polymer photovoltaic cells by self-organization of polymer blends," *Nature Materials*, vol. 4, no. 11, Art. no. 11, Nov. 2005, doi: 10.1038/nmat1500.

[55] W. Ma, C. Yang, X. Gong, K. Lee, and A. J. Heeger, "Thermally Stable, Efficient Polymer Solar Cells with Nanoscale Control of the Interpenetrating Network Morphology," *Advanced Functional Materials*, vol. 15, no. 10, pp. 1617–1622, 2005, doi: https://doi.org/10.1002/adfm.200500211.

[56] Z. Li *et al.*, "The Role of the Hydrogen Bond between Piperazine and Fullerene Molecules in Stabilizing Polymer:Fullerene Solar Cell Performance," *ACS Appl. Mater. Interfaces*, vol. 12, no. 13, pp. 15472–15481, Apr. 2020, doi: 10.1021/acsami.9b23366.

[57] D. A. Skoog, S. R. Crouch, and F. J. Holler, *Principles of instrumental analysis.* Belmont, CA: Thomson Brooks/Cole, 2007.

[58] H. Determann, *Gel Chromatography: Gel Filtration · Gel Permeation · Molecular Sieves A Laboratory Handbook*, 2nd ed. Berlin Heidelberg: Springer-Verlag, 1969.

[59] "Cyclic Voltammetry—'Electrochemical Spectroscopy'. New Analytical Methods (25) - Heinze - 1984 - Angewandte Chemie International Edition in English - Wiley Online Library." https://onlinelibrary.wiley.com/doi/abs/10.1002/anie.198408313 (accessed Nov. 18, 2020).

[60] "The use of cyclic voltammetry in the study of the chemistry of metal-carbonyls: An introductory experiment | Journal of Chemical Education." https://pubs.acs.org/doi/abs/10.1021/ed065p1020 (accessed Nov. 18, 2020).

[61] A. W. Bott, "Characterization of Chemical Reactions Coupled to Electron Transfer Reactions Using Cyclic Voltammetry," *Current Separations*, p. 8, 1999.

[62] J.-L. Bredas, "Mind the gap!," *Materials Horizons*, vol. 1, no. 1, pp. 17–19, 2014, doi: 10.1039/C3MH00098B.

[63] Y. He, J. T. E. Quinn, D. Hou, J. H.L. Ngai, and Y. Li, "A small bandgap (3 E ,7 E)-3,7-bis(2-oxoindolin-3-ylidene)benzo[1,2- b :4,5- b ′]difuran-2,6(3 H ,7 H)-dione (IBDF) based polymer semiconductor for near-infrared organic phototransistors," *Journal of Materials Chemistry C*, vol. 5, no. 46, pp. 12163–12171, 2017, doi: 10.1039/C7TC03584E.

[64] D. A. Skoog, F. J. Holler, and S. R. Crouch, *Principles of instrumental analysis.* Belmont, CA : Thomson Brooks/Cole, 2007.

[65] A. W. Coats and J. P. Redfern, "Thermogravimetric analysis. A review," *Analyst*,

vol. 88, no. 1053, pp. 906–924, Jan. 1963, doi: 10.1039/AN9638800906.

[66] T. Zhang, J. Jin, S. Yang, D. Hu, G. Li, and J. Jiang, "Synthesis and Characterization of Fluorinated PBO With High Thermal Stability and Low Dielectric Constant," 2009, doi: 10.1080/00222340903041244.

[67] X. Liu and W. Yu, "Evaluating the thermal stability of high performance fibers by TGA," *Journal of Applied Polymer Science*, vol. 99, no. 3, pp. 937–944, 2006, doi: https://doi.org/10.1002/app.22305.

[68] W. Missal *et al.*, "Miniaturized ceramic differential scanning calorimeter with integrated oven and crucible in LTCC technology," *Procedia Engineering*, vol. 5, pp. 940–943, Jan. 2010, doi: 10.1016/j.proeng.2010.09.263.

[69] "Measuring-and-understanding-force-distance-curves-v2.pdf." Accessed: Nov. 18, 2020. [Online]. Available: https://www.afmworkshop.com/images/news2019/01/Measuring-and-understanding-force-distance-curves-v2.pdf.

[70] P. J. Bryant, R. G. Miller, and R. Yang, "Scanning tunneling and atomic force microscopy combined," *Appl. Phys. Lett.*, vol. 52, no. 26, pp. 2233–2235, Jun. 1988, doi: 10.1063/1.99541.

[71] H.-J. Butt, B. Cappella, and M. Kappl, "Force measurements with the atomic force microscope: Technique, interpretation and applications," *Surface Science Reports*, vol. 59, no. 1, pp. 1–152, Oct. 2005, doi: 10.1016/j.surfrep.2005.08.003.

[72] R. Kohli and K. L. Mittal, Eds., "Chapter 3 - Methods for Assessing Surface Cleanliness," in *Developments in Surface Contamination and Cleaning, Volume 12*, Elsevier, 2019, pp. 23–105.

[73] J. P. Patel and P. H. Parsania, "3 - Characterization, testing, and reinforcing materials of biodegradable composites," in *Biodegradable and Biocompatible Polymer Composites*, N. G. Shimpi, Ed. Woodhead Publishing, 2018, pp. 55–79.

[74] Y. Kim, M. Shin, H. Kim, Y. Ha, and C.-S. Ha, "Influence of electron-donating polymer addition on the performance of polymer solar cells," *J. Phys. D: Appl. Phys.*, vol. 41, no. 22, p. 225101, Oct. 2008, doi: 10.1088/0022-3727/41/22/225101.

[75] Y. Kim *et al.*, "A strong regioregularity effect in self-organizing conjugated polymer films and high-efficiency polythiophene:fullerene solar cells," *Nature Materials*, vol. 5, pp. 197–203, Mar. 2006, doi: 10.1038/nmat1574.

[76] S. Holliday *et al.*, "High-efficiency and air-stable P3HT-based polymer solar cells with a new non-fullerene acceptor," *Nature Communications*, vol. 7, no. 1, Art. no. 1, Jun. 2016, doi: 10.1038/ncomms11585.

[77] C. Wang *et al.*, "A zinc(II) complex of di(naphthylethynyl)azadipyrromethene with low synthetic complexity leads to OPV with high industrial accessibility," *J. Mater. Chem. A*, vol. 7, no. 42, pp. 24614–24625, Oct. 2019, doi:

10.1039/C9TA08654D.

[78] D. M. de Leeuw, M. M. J. Simenon, A. R. Brown, and R. E. F. Einerhand, "Stability of n-type doped conducting polymers and consequences for polymeric microelectronic devices," *Synthetic Metals*, vol. 87, no. 1, pp. 53–59, Feb. 1997, doi: 10.1016/S0379-6779(97)80097-5.

[79] J. Zaumseil and H. Sirringhaus, "Electron and Ambipolar Transport in Organic Field-Effect Transistors," *Chem. Rev.*, vol. 107, no. 4, pp. 1296–1323, Apr. 2007, doi: 10.1021/cr0501543.

[80] H. Yan *et al.*, "A high-mobility electron-transporting polymer for printed transistors," *Nature*, vol. 457, no. 7230, Art. no. 7230, Feb. 2009, doi: 10.1038/nature07727.

[81] I. Osaka *et al.*, "Synthesis, Characterization, and Transistor and Solar Cell Applications of a Naphthobisthiadiazole-Based Semiconducting Polymer," *J. Am. Chem. Soc.*, vol. 134, no. 11, pp. 5425–5425, Mar. 2012, doi: 10.1021/ja3015346.

[82] J. W. Jo, S. Bae, F. Liu, T. P. Russell, and W. H. Jo, "Comparison of Two D−A Type Polymers with Each Being Fluorinated on D and A Unit for High Performance Solar Cells," *Advanced Functional Materials*, vol. 25, no. 1, pp. 120–125, 2015, doi: 10.1002/adfm.201402210.

[83] W. Hong, C. Guo, B. Sun, and Y. Li, "(3Z,3′Z)-3,3′-(Hydrazine-1,2-diylidene)bis(indolin-2-one) as a new electron-acceptor building block for donor–acceptor π-conjugated polymers for organic thin film transistors," *J. Mater. Chem. C*, vol. 3, no. 17, pp. 4464–4470, Apr. 2015, doi: 10.1039/C5TC00447K.

[84] W. Hong, B. Sun, H. Aziz, W.-T. Park, Y.-Y. Noh, and Y. Li, "A conjugated polyazine containing diketopyrrolopyrrole for ambipolar organic thin film transistors," *Chem. Commun.*, vol. 48, no. 67, pp. 8413–8415, Jul. 2012, doi: 10.1039/C2CC33998F.

[85] M. K. Poduval *et al.*, "Stereoisomers of an azine-linked donor–acceptor conjugated polymer: the impact of molecular conformation on electrical performance," *RSC Adv.*, vol. 6, no. 50, pp. 44272–44278, May 2016, doi: 10.1039/C6RA07389A.

[86] R. P. Ortiz, H. Yan, A. Facchetti, and T. Marks, "Azine- and Azole-Functionalized Oligo′ and Polythiophene Semiconductors for Organic Thin-Film Transistors," *Materials*, vol. 3, no. 3, pp. 1533–1558, Mar. 2010, doi: 10.3390/ma3031533.

[87] L. Peng *et al.*, "Development of s-tetrazine-based polymers for efficient polymer solar cells by controlling appropriate molecular aggregation," *Dyes and Pigments*, vol. 171, p. 107717, Dec. 2019, doi: 10.1016/j.dyepig.2019.107717.

[88] M. Lewis and R. Glaser, "The Azine Bridge as a Conjugation Stopper: An NMR

Spectroscopic Study of Electron Delocalization in Acetophenone Azines [†]," *J. Org. Chem.*, vol. 67, no. 5, pp. 1441–1447, Mar. 2002, doi: 10.1021/jo011117o.

[89] V. A. Sauro and M. S. Workentin, "Evaluation of the Extent of Conjugation in Symmetrical and Asymmetrical Aryl-Substituted Acetophenone Azines Using Electrochemical Methods," *J. Org. Chem.*, vol. 66, no. 3, pp. 831–838, Feb. 2001, doi: 10.1021/jo0056287.

[90] D. H. Kim *et al.*, "Liquid-Crystalline Semiconducting Copolymers with Intramolecular Donor−Acceptor Building Blocks for High-Stability Polymer Transistors," *J. Am. Chem. Soc.*, vol. 131, no. 17, pp. 6124–6132, May 2009, doi: 10.1021/ja8095569.

[91] I. McCulloch *et al.*, "Liquid-crystalline semiconducting polymers with high charge-carrier mobility," *Nature Materials*, vol. 5, no. 4, Art. no. 4, Apr. 2006, doi: 10.1038/nmat1612.

[92] T. Mori, H. Komiyama, T. Ichikawa, and T. Yasuda, "A liquid-crystalline semiconducting polymer based on thienylene–vinylene–thienylene: Enhanced hole mobilities by mesomorphic molecular ordering and thermoplastic shape-deformable characteristics," *Polymer Journal*, vol. 52, no. 3, Art. no. 3, Mar. 2020, doi: 10.1038/s41428-019-0282-4.

[93] V. Savikhin *et al.*, "Morphological, Chemical, and Electronic Changes of the Conjugated Polymer PTB7 with Thermal Annealing," *iScience*, vol. 2, pp. 182–192, Apr. 2018, doi: 10.1016/j.isci.2018.03.002.

[94] H. Sirringhaus *et al.*, "Two-dimensional charge transport in self-organized, high-mobility conjugated polymers," *Nature*, vol. 401, no. 6754, pp. 685–688, Oct. 1999, doi: 10.1038/44359.

[95] J.-R. Pouliot, M. Wakioka, F. Ozawa, Y. Li, and M. Leclerc, "Structural Analysis of Poly(3-hexylthiophene) Prepared via Direct Heteroarylation Polymerization," *Macromolecular Chemistry and Physics*, vol. 217, no. 13, pp. 1493–1500, 2016, doi: 10.1002/macp.201600050.

[96] S. Foster *et al.*, "Electron Collection as a Limit to Polymer:PCBM Solar Cell Efficiency: Effect of Blend Microstructure on Carrier Mobility and Device Performance in PTB7:PCBM," *Advanced Energy Materials*, vol. 4, no. 14, p. 1400311, 2014, doi: 10.1002/aenm.201400311.

[97] D. Baran *et al.*, "Reducing the efficiency–stability–cost gap of organic photovoltaics with highly efficient and stable small molecule acceptor ternary solar cells," *Nature Mater*, vol. 16, no. 3, Art. no. 3, Mar. 2017, doi: 10.1038/nmat4797.

[98] L.-Y. He *et al.*, "Synthesis of poly(thiophene-alt-pyrrole) from a difunctionalized thienylpyrrole by Kumada polycondensation," *Tetrahedron*, vol. 71, no. 33, pp. 5399–5406, Aug. 2015, doi: 10.1016/j.tet.2015.05.091.

[99] T. H. Nguyen *et al.*, "N-Benzoyl dithieno[3,2-b:2′,3′-d]pyrrole-based

hyperbranched polymers by direct arylation polymerization," *Chemistry Central Journal*, vol. 11, no. 1, p. 135, Dec. 2017, doi: 10.1186/s13065-017-0367-0.

[100] T. W. Brockmann and J. M. Tour, "Synthesis and Properties of Low-Bandgap Zwitterionic and Planar Conjugated Pyrrole-Derived Polymeric Sensors. Reversible Optical Absorption Maxima from the UV to the Near-IR," *J. Am. Chem. Soc.*, vol. 117, no. 16, pp. 4437–4447, Apr. 1995, doi: 10.1021/ja00121a001.

[101] S. Jadoun, L. Biswal, and U. Riaz, "Tuning the optical properties of poly(o-phenylenediamine-co-pyrrole) via template mediated copolymerization," *Designed Monomers and Polymers*, vol. 21, no. 1, pp. 75–81, Jan. 2018, doi: 10.1080/15685551.2018.1459078.

[102] L. Yan, M. Shao, H. Wang, D. Dudis, A. Urbas, and B. Hu, "High Seebeck Effects from Hybrid Metal/Polymer/Metal Thin-Film Devices," *Advanced Materials*, vol. 23, no. 35, pp. 4120–4124, 2011, doi: https://doi.org/10.1002/adma.201101634.

[103] H. Zarenezhad, T. Balkan, N. Solati, M. Halali, M. Askari, and S. Kaya, "Efficient carrier utilization induced by conductive polypyrrole additives in organic-inorganic halide perovskite solar cells," *Solar Energy*, vol. 207, pp. 1300–1307, Sep. 2020, doi: 10.1016/j.solener.2020.07.059.

[104] K. Keothongkham, S. Pimanpang, W. Maiaugree, S. Saekow, W. Jarernboon, and V. Amornkitbamrung, "Electrochemically Deposited Polypyrrole for Dye-Sensitized Solar Cell Counter Electrodes," *International Journal of Photoenergy*, vol. 2012, pp. 1–7, 2012, doi: 10.1155/2012/671326.

[105] P. Schilinsky, U. Asawapirom, U. Scherf, M. Biele, and C. J. Brabec, "Influence of the Molecular Weight of Poly(3-hexylthiophene) on the Performance of Bulk Heterojunction Solar Cells," *Chem. Mater.*, vol. 17, no. 8, pp. 2175–2180, Apr. 2005, doi: 10.1021/cm047811c.